RF magnetron sputtered perovskite oxide electrodes for Ferroelectric RAM

Thesis submitted to
COCHIN UNIVERSITY OF SCIENCE AND TECHNOLOGY
in partial fulfillment of the requirements
for the award of the degree of
DOCTOR OF PHILOSOPHY

Asha. A. S

Department of Physics
Cochin University of Science and Technology
Cochin – 682 022, Kerala, India

December 2007

RF magnetron sputtered perovskite oxide electrodes for Ferroelectric RAM

Ph.D thesis in the field of material science

Author:

Asha.A.S
Optoelectronics Device Laboratory
Department of Physics
Cochin University of Science and Technology
Cochin – 682 022, Kerala, India
email: ashaas@gmail.com

Supervisor:

Dr. M.K. Jayaraj
Reader
Optoelectronics Device Laboratory
Department of Physics
Cochin University of Science and Technology
Cochin – 682 022, Kerala, India
email: mkj@cusat.ac.in

December 2007

Dr. M.K. Jayaraj

Reader
Department of Physics
Cochin University of Science and Technology
Cochin – 682 022

14th December 2007

Certificate

Certified that the work presented in this thesis entitled "*RF magnetron sputtered perovskite oxide electrodes for Ferroelectric RAM*" is based on the authentic record of research done by Mrs. Asha.A.S under my guidance in the Department of Physics, Cochin University of Science and Technology, Cochin – 682 022 and has not been included in any other thesis submitted for the award of any degree.

Dr. M.K. Jayaraj

(Supervising Guide)

Phone : +91 484 2577404 extn 33   Fax: 91 484 2577595   email: mkj@cusat.ac.in

Declaration

Certified that the work presented in this thesis entitled *"RF magnetron sputtered perovskite oxide electrodes for Ferroelectric RAM"* is based on the original research work done by me under the supervision and guidance of Dr. M.K. Jayaraj, Reader, Department of Physics, Cochin University of Science and Technology, Cochin-682022 and has not been included in any other thesis submitted previously for the award of any degree.

Kochi – 682022

Asha. A. S

Acknowledgements

Contents

Preface

Chapter 1
An overview of ferroelectric capacitor and
applications of perovskite LSCO electrode

Chapter 2
Thin Film Deposition Techniques and
Characterization Tools

Chapter 3
Preparation and Characterization of
$La_{1-x}Sr_xCoO_3$ and $La_{0.5}Sr_{0.5}Co_{1-x}Ni_xO_3$

Chapter 4
Preparation and Characterization of $La_{0.5}Sr_{0.5}CoO_3$ thin films

Chapter 5
Preparation and Characterization of $La_{0.5}Sr_{0.5}Co_{0.5}Ni_{0.5}O_3$ thin Films

Chapter 6
Ferroelectric Capacitors

Chapter 7
Summary and Outlook

Preface

Oxide materials have a wide range of property covering from insulators to high temperature superconductors and from ferroelectric to ferromagnetic materials. They posses an enormous range of electrical optical and magnetic properties and thus have great potential for the application of novel device. Perovskite oxides have been subject to various crystallographic, magnetic and electronic investigations due to their wide variety of physical properties. Lanthanoid cobaltites form an important class of perovskite oxide. Among them $La_{1-x}Sr_xCoO_3$ has been subjected to immense research because of the peculiar way their magnetic and transport properties change with temperature.

$La_{1-x}Sr_xCoO_3$ is obtained from $LaCoO_3$ by substitution of Sr^{2+} for La^{3+}. Strontium substitution brings about remarkable changes in the structural and transport properties of the system. $LaCoO_3$ belong to ABO_3 perovskite with rhombohedral distortion. The rhombohedral distortion decreases with increasing Sr^{2+} content and at about 50 % Sr^{2+} content the system is cubic. For Sr^{2+} content $x > 0.5$ the system is tetragonal. The charge compensation for Sr^{2+} substitution for La^{3+} is accomplished either by the oxidation of Co^{3+} to Co^{4+} or by the creation of oxygen vacancy. As the Sr^{2+} content increases, the Co^{4+} content also increases, increasing the conductivity. When Sr^{2+} content $x = 0.5$, the Co^{4+} content reaches its maximum and with further increase in Sr^{2+} content the structural phase transition occurs with the creation of oxygen vacancy and the conductivity decreases. $LaCoO_3$ show high resistivity and antiferromagnetic exchange interaction. But $La_{1-x}Sr_xCoO_3$ evolves towards a ferromagnetic state with itinerant electrons as Sr^{2+} content increases. The system shows a spin glass type magnetic behavior for low Sr^{2+} doping ($x < 0.25$) due to inhomogeneous magnetic clusters. For higher Sr^{2+} doping the system shows short range ferromagnetic ordering.

i

$La_{0.5}Sr_{0.5}CoO_3$ (LSCO) has been used in the field of catalysis, gas sensors, and oxygen penetration membranes and as electrode in oxide fuel cells and ferroelectric memory due to its relatively high electrical and ionic conductivity. LSCO has similar crystal structure as that of the most widely used perovskite ferroelectrics like $Pb(ZrTi)O_3$, $(Pb,La)(ZrTiO_3)$ and $(Ba,Sr)TiO_3$, and have good chemical stability. Therefore LSCO can serve as electrode as well as growth template layer and protective barrier during device fabrication. The LSCO being a conductive oxide electrode, act as a sink for oxygen vacancies thereby reducing the fatigue. LSCO is also an oxygen ion conductor which makes it useful as a cathode material for fuel cells. LSCO also opens up an interesting option as a candidate for n-MOS gate applications as the work function of LSCO is close to 4.2 eV. The large window of electronic, ionic and catalytic properties of $La_{1-x}Sr_xCoO_3$ makes it a suitable candidate for gas sensing applications. The conductivity of $La_{0.5}Sr_{0.5}CoO_3$ thin films can be improved by the partial substitution of Co by Ni. Doping Ni to replace Co ion at B-site can change the electrostatic potential due to their different electron affinities. Therefore $La_{0.8}Sr_{0.2}Co_{1-x}Ni_xO_{3-\delta}$ can be used for CO detection at relatively low temperatures.

The main objective of this thesis work is to optimize the growth conditions for obtaining crystalline and conducting $La_{0.5}Sr_{0.5}CoO_3$ (LSCO) and $La_{0.5}Sr_{0.5}Co_{0.5}Ni_{0.5}O_3$ (LSCNO) thin films at low processing temperatures. The films are prepared by radio frequency magnetron sputtering under various deposition conditions. The thin films were used as electrodes for the fabrication of ferroelectric capacitors using $Ba_{0.7}Sr_{0.3}TiO_3$ (BST) and $PbZr_{0.52}Ti_{0.48}O_3$ (PZT). The structural and transport properties of the $La_{1-x}Sr_xCoO_3$ and $La_{0.5}Sr_{0.5}Co_{1-x}Ni_xO_3$ are also investigated. The characterization of the bulk and the thin films were performed using different tools. A powder X-ray diffractometer was used to analyze the crystalline nature of the material. The transport properties were investigated by measuring the temperature dependence of resistivity using a four probe technique. The magnetoresistance and thermoelectric power were also

used to investigate the transport properties. Atomic force microscope was used to study the surface morphology and thin film roughness. The ferroelectric properties of the capacitors were investigated using RT66A ferroelectric tester.

An overview of the developments in the field of $La_{1-x}Sr_xCoO_3$ and $La_{0.5}Sr_{0.5}Co_{1-x}Ni_xO_3$ is briefly presented in *Chapter 1*. The chapter presents a detailed literature review on the materials. $La_{0.5}Sr_{0.5}CoO_3$ is used as electrode for ferroelectric capacitors and for many other applications. The advantages of $La_{0.5}Sr_{0.5}CoO_3$ thin films as a potential candidate over other materials are discussed.

Chapter 2 deals with the various deposition methods and characterization tools employed in the present study. The characterization tools include both characterization of the bulk and the thin films.

Chapter 3 presents the preparation and characterization of $La_{1-x}Sr_xCoO_3$ and $La_{0.5}Sr_{0.5}Co_{1-x}Ni_xO_3$ system. $La_{1-x}Sr_xCoO_3$ has been prepared for varying Sr content and $La_{0.5}Sr_{0.5}Co_{1-x}Ni_xO_3$ for varying Ni content, both with x varying from 0.1 to 0.6. The structural evolution of both the compounds with varying Sr and Ni content has been examined. $La_{1-x}Sr_xCoO_3$ prepared for varying Sr^{2+} content were all single phase. The system could be indexed to rhombohedral distorted perovskite structure, space group $R\bar{3}C$ for all except x = 0.6, which had a tetragonal structure. $La_{0.5}Sr_{0.5}Co_{1-x}Ni_xO_3$ had some impurity phase in addition to perovskite $La_{0.5}Sr_{0.5}Co_{1-x}Ni_xO_3$. The transport properties of the system with varying doping concentration of Sr^{2+} and Ni^{3+} have been studied using the temperature dependant measurement of resistivity, magnetoresistance and thermoelectric power. The resistivity data indicated a semiconducting behavior for x = 0.1 of $La_{1-x}Sr_xCoO_3$ and for x > 0.1, the system was metallic. The resistivity was found to decrease with Sr^{2+} content with the x = 0.5 having the lowest resistivity. Whereas for $La_{0.5}Sr_{0.5}Co_{1-x}Ni_xO_3$, the system was metallic for

lightly doped samples ($x \leq 0.3$) and with $x > 0.3$ it was insulating. The MR of the $La_{1-x}Sr_xCoO_3$ indicated a small negative MR for the metallic samples with the peak near the critical temperature. But the semiconducting composition showed a large negative MR at low temperature. In $La_{0.5}Sr_{0.5}Co_{1-x}Ni_xO_3$ only the metallic compositions showed small negative MR and the insulating compositions showed no MR. The thermoelectric power measurements of both the systems indicated large thermoelectric power for the insulating compositions and the metallic compositions had small positive values.

Chapter 4 presents the preparation and characterization of LSCO thin films by rf magnetron sputtering. The rf power, the annealing conditions, sputtering gas pressure, oxygen partial pressure and substrate temperature were optimized to obtain crystalline and conducting LSCO thin film. The rf power was optimized to be 150 W and the post deposition annealing condition was optimized as 600 °C in oxygen for one hour. The sputtering gas pressure was optimized to be 0.003 mbar for preparing conducting thin films at room temperature. But oxygen incorporation in the sputtering gas was found to deteriorate the film properties. The films prepared with the minimum oxygen partial pressure were single phase with minimum resistivity. Deposition at elevated substrate temperature enhanced the crystallinity of the films prepared at high sputtering gas pressure. Crystalline and conducting LSCO thin films were obtained at substrate temperature as low as 500 °C.

Chapter 5 explains the growth and characterizations of LSCNO thin films. The deposition pressure, substrate temperature and $Ar:O_2$ ratio during rf magnetron sputtering has been optimized to get better conducting perovskite thin films. Oxygen incorporation during sputtering was found to improve the crystallinity and conductivity of the thin films. The substrate temperature could be lowered to 300 °C for obtaining crystalline conducting LSCNO thin film. Crystalline thin films were obtained irrespective of the substrate material at the optimized deposition condition. The films deposited on $Pt/TiO_2/SiO_2/Si$ substrates showed

considerable variation in resistivity with deposition conditions and gave the minimum resistivity. The LSCNO thin film deposited on $Pt/TiO_2/SiO_2/Si$ substrate have the advantage of lower resistivity of Pt and improved fatigue behavior associated with LSCNO thin film. The atomic force microscopy images of the thin films revealed a smooth surface for the films prepared with oxygen intercalation. An exceptionally smooth surface for the thin films deposited on Si substrates facilitates its use in high quality integrated devices.

Chapter 6 explains the preparation and characterisation of ferroelectric capacitors using LSCO and LSCNO as electrodes. Capacitors were fabricated using BST and PZT as the ferroelectric (FE) material. The capacitors had the following structure viz; $Pt/TiO_2/SiO_2/Si/LSCO/FE/LSCO$ and $Pt/TiO_2/SiO_2/Si/LSCNO/FE/LSCNO$. The structural, electrical and ferroelectric properties of the capacitors are studied and the properties are compared with capacitors using conventional electrodes.

Chapter 7 presents the summary and outlook.

-

Publications related to the work presented in the thesis

1. Structural and Electrical properties of $La_{0.5}Sr_{0.5}CoO_3$ thin films prepared by rf magnetron sputtering, **A.S.Asha**, M.T.Sebastian, M.K.Jayaraj Journal of alloys and compounds. **449(2008)68**
2. Low temperature deposition of $La_{0.5}Sr_{0.5}Co_{0.5}Ni_{0.5}O_3$ thin films **A.S.Asha**, M.T.Sebastian, M.K.Jayaraj (submitted to Applied Surface Science)
3. Optimization of the deposition pressure and substrate temperature for crystalline conducting LSCO thin films **A.S.Asha**, M.T.Sebastian, M.K.Jayaraj (to be communicated)
4. Structural and transport properties of perovskite oxides $La_{1-x}Sr_xCoO_3$ and $La_{0.5}Sr_{0.5}Co_{1x}Ni_xO_3$ **A.S.Asha**, M.T.Sebastian, M.K.Jayaraj (to be communicated)

Conference Proceedings

1. Pulsed laser deposition of BST thin films for FeRAM applications. R.Reshmi, **A.S.Asha**, M.K.Jayaraj, 9th International Conference on Laser Ablation, 2007
2. Low Temperature Deposition Of $La_{0.5}Sr_{0.5}Co_{0.5}Ni_{0.5}O_3$ Thin Films **A.S.Asha**, M.T.Sebastian, M.K.Jayaraj, National Conference on Smart Electroceramics, 2007
3. Structural and Electrical properties of $La_{0.5}Sr_{0.5}CoO_3$ thin films prepared by rf magnetron sputtering **A.S.Asha**, M.T.Sebastian, M.K.Jayaraj, International Symposium on Functional Materials, 2005
4. Electrical properties of RF sputtered $La_{0.5}Sr_{0.5}Co_{0.5}Ni_{0.5}O_3$ thin films **A.S.Asha**, M.T.Sebastian, R.W.Schwartz M.K.jayaraj Proc. DAE Solid State Physics Symposium, 49(2004)860

Other Publications to which author has contributed

1. Pulsed laser deposition of p-type α-$AgGaO_2$ thin films K.A.Vanaja, R.S.Ajimsha, **A.S.Asha**, K.RajeevKumar, M.K.Jayaraj (article in press Thin Solid Films)
2. p-type electrical conduction in α-AgGaO2 delafossite thin film K. A. Vanaja, R. S. Ajimsha, **A.S.Asha**, M. K. Jayaraj, Applied Physics Letters **88(2006)212103**

3. Electrical and optical properties of $ZnGa_2O_4$ thin films deposited by pulsed laserdeposition, K Mini Krishna, M.Nisha, R Reshmi, R Manoj, **A.S.Asha**, M.K.Jayaraj, Materials Forum **29**(2005)243

4. Growth of $CuInS_2$ thin films by sulphurisation of Cu-In alloys, Aldrin Antony, **A.S.Asha**, Rahana Yoosuf, Manoj R, M.K.Jayaraj, Solar Energy Materials and Solar Cells **81**(2004)407

5. $CuInS_2$/CdS Solar cell with the absorber layer prepared by sulphurisation technique, **A.S.Asha,** Sukesh G, Rahana Yoosuf, M.K.Jayaraj, International conference on electrochemical power systems 2004

6. Transprent p-AgCoO2/n-ZnO pn junction K.A.Vanaja, M.Nisha, **A.S.Asha**, M.K.Jayaraj, Photonics 2004

7. Improved adhesion of copper Indium sulphide by gallium Incorporation, **A.S.Asha**, Rahana Yoosuf, Sukesh. G, M.K.Jayaraj, Proc. DAE Solid State Physics Symposium, **49**(2004)768

8. Electrical and optical properties of α-AgGaO2 synthesised by hydrothermal reaction, K.A.Vanaja., M.Nisha., **A.S.Asha**, M.K.Jayaraj Proc. DAE Solid State Physics Symposium, **49**(2004)770

9. Thermal diffusivity of flash evaporated $CuInSe_2$ thin films by photothermal beam deflection Mohamed M.A.Fadhali, A.S.Asha, Aldrin Antony, Jyotsna Ravi, K. P. R. Nair, T. M. A. Rasheed and M. K. Jayaraj, Proc. DAE Solid State Physics Symposium, **46**(2003)667

10. Preparation and characterisation of single phase $CuInS_2$ films by two stage process, Aldrin Antony, M.Gafoor, **A.S.Asha**, Rahna Yousf and M.K.Jayaraj, Proc. DAE Solid State Physics Symposium, Chandigarh, India, **45**(2002)475

CHAPTER 1

An overview of ferroelectric capacitor and applications of perovskite LSCO electrode

This chapter gives an overview of ferroelectric capacitors. The various degradation mechanisms of ferroelectric capacitors and the need for choosing conducting perovskite oxide electrode LSCO are discussed. A brief description on the other applications of LSCO is given and the properties of the compound are discussed.

-

3

1.1 Introduction

Ferroelectric random access memories (FeRAM) have attracted considerable attention due to its superior performance over the conventional planar devices [1, 2]. Their intrinsic nonvolatility, low operating voltage, low operating power, fast read/write speed and excellent endurance make them superior over semiconductor memory technologies such as flash memory and magnetic random access memory (MRAM) [1-5]. The popularity of modern electronic portable devices such as mobile phones and notebook computers has increased the demand for non volatile memories [6, 7]. FeRAM is one of the most promising candidates for non volatile memory, and currently there is active research and development in this field [2, 3, 5]. FeRAMs are currently used in low density (up to 1-2 Mbytes) memories in "smart cards" and other radio frequency integrated devices (RFID) [8]. Production of FeRAMs with several hundred megabits in future can replace all existing memories such as dynamic RAM (DRAM), electrically erasable programmable read only memory (E^2PROM), and flash memory [6-10].

In this chapter an overview of the FeRAM is presented with emphasis on capacitor type memory. The various degradation factors encountered in a ferroelectric capacitor and the possibility of circumventing them are discussed. The use of perovskite oxides especially $La_{0.5}Sr_{0.5}CoO_3$ (LSCO) as electrode for ferroelectric capacitor is discussed. The other applications of LSCO is also explored along with the structural and transport properties of the compound.

1.2 Basic Operation of FeRAM

Crystals can be classified into seven crystal systems depending on their geometry. These systems are again subdivided into point groups or crystal classes according to their symmetry with respect to a point. There are such 32 crystal classes and among them 11 possess centre of symmetry and have no

polar properties [11, 12]. Among the remaining 21 non-centric crystal classes, all except one exhibit electrical polarity when subject to stress. The effect is called piezoelectric effect and is linear, with reversal of the stimulus resulting in a reversal of the response. Of the piezoelectric crystal classes 10 are characterized by unique polar axis and are called polar as they posses spontaneous polarization. The spontaneous polarization is temperature dependent and the effect is called pyroelectric effect. The effect can be detected by observing the flow of charge to and from the surfaces on change of temperature [12].

A crystal is said to be ferroelectric when it has two or more orientational states in the absence of an electric field and can be shifted from one to another of these states by an electric field. These two orientaional states are identical in crystal structure and differ only in electric polarization vector at null electric field. The highest symmetry phase compatible with the ferroelectric structure is called the prototype phase. The protype phase is non polar in character and exists as the highest temperature phase of the crystal. Structural distortion to the prototype phase destroys the symmetry of the phase and the ferroelectric then posses a spontaneous polarization. The spontaneous polarization decreases with increasing temperature T and disappear at a Curie point T_c. Thus a ferroelectric phase change represents a special class of structural phase transition denoted by the appearance of a spontaneous polarization. The phase which transforms to the ferroelectric form at T_c is called the paraelectric phase. Below T_c in the absence of applied field, there are at least two directions along which the spontaneous polarization can develop. The different regions of the crystal polarize in each of these directions to minimize the depolarizing field. Each volume of uniform polarization is called domain [12].

Ferroelectric material is characterized by spontaneous polarization and the polarization has a hysteric dependence on applied electric field. It is this property of the ferroelectric material which is used in the memory device. The

non centerosymmetric arrangement of the atoms in the unit cell gives a net dipole moment to the material in the ferroelectric phase. The property is commonly observed in ABO_3 perovskites where the up and down displacement of the B cation with respect to the other ions gives the net dipole moment (figure 1.1 a) [3, 13]. In a typical ferroelectric material there will be ferroelectric domains where the polarization is either in the up or down direction. By the application of a large electric field to the specimen all the domains can be aligned in one direction and at a particular applied voltage the material reaches its saturation polarization P_s. The polarization of the entire crystal can be switched from up to down by reversing the applied field. Figure 1.1 b shows the hysteresis loop of a ferroelectric material. Coercive field E_c is the threshold voltage above which the polarization changes its sign. The two zero field values $\pm P_r$ are equally stable and may be encoded as the logic state 1 and 0 of the memory device. Since no voltage is required to maintain the memory the device is "nonvolatile" [1, 3, 12, 13].

(a)   **(b)**
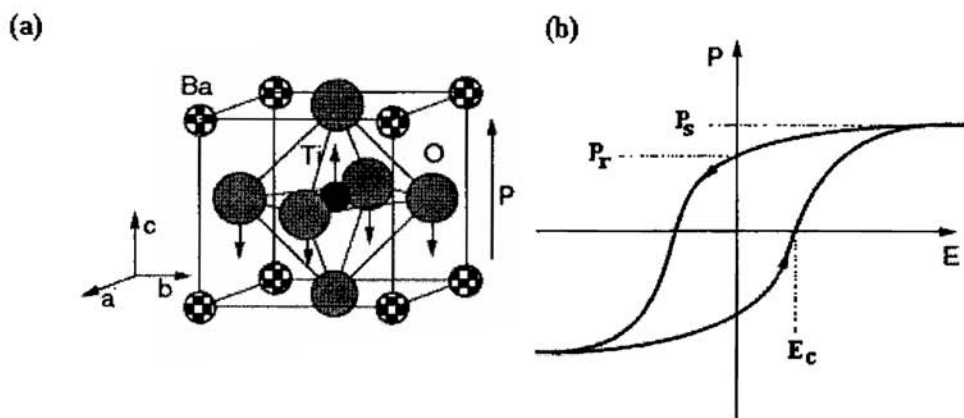
Figure 1.1. (a) Intrinsic spontaneous polarization in tetragonal $BaTiO_3$ (b) Schematic of a hysteresis loop for a ferroelectric material induced by an external electric field E, where P_s, P_r and E_c are saturation polarization, remanent polarization and coercive field respectively

7

FeRAM may be classified into two types of memory cell structures [2, 14-17]. One is the destructive read out memory which is the one transistor one capacitor type or 1T-1C type. In this case a ferroelectric capacitor is combined with a metal oxide semiconductor field effect transistor (MOSFET) for cell selection. Figure 1.2 a shows the circuit diagram of a 1T-1C memory cell activated through word line (WL), and written or read through bit line (BL) and plate line (PL). In writing a binary digit zero to the cell, a positive voltage V_{DD}, is applied to the bit line while the plate line is grounded and the word line is asserted. The voltage waveform that appears across the capacitor is a positive square pulse with amplitude V_{DD}-V_T, where V_T is the threshold voltage of the access transistor. In writing a binary digit 1, a positive voltage V_{DD} is applied to the plate line while the bit line is grounded and the word line is asserted. The voltage waveform across the capacitor in this case is a negative pulse with amplitude V_{DD}. A cell can be read by floating the bit line and applying positive voltage V_{DD} to the plate line while asserting the word line. If the initial polarization state of the capacitor is negative, reading the cell develops a relatively large signal on the bit line. If the polarization state of the capacitor is positive the cell develops a small signal on the bit line. Since this operation is destructive data must be written back into the cell after each read [2, 14, 15].

The second structure is a nondestructive read out memory in which the ferroelectric capacitor in the previous structure is replaced with a ferroelectric-gate field effect transistor ie a metal ferroelectric semiconductor field effect transistor (MFSFET) as given in figure 1.2 b. It is composed of two field effect transistors (FET); one is the ferroelectric gate FET for data storage and the other is a MOSFET for cell selection. The ferroelectric gate FET is the key device in this cell, whose gate insulator is composed of a ferroelectric material. The "0" and "1" data are written in the ferroelectric film as the direction of polarization. The data can be readout as a difference of drain current of the FET. All commercially available FeRAMs are based on the capacitor type structure as its fabrication is easier than the FET type. The largest capacity of the FeRAM

commercially available at present is 4 Mbits produced by Sam Sung electronics [14-17].
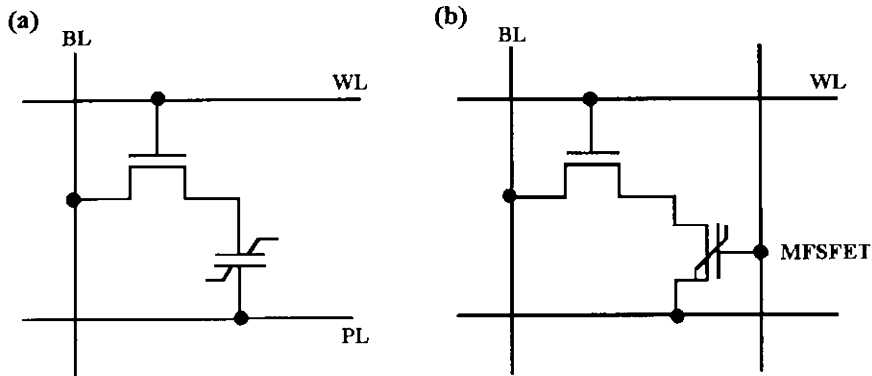
Figure 1.2. Circuit diagram of ferroelectric random access memories (a) Destructive read out type and (b) Non destructive read out type. BL, WL and PL are the bit line, word line and plate line respectively

1.3 Ferroelectric Materials

Perovskites having the formula ABO_3 is one family of well established ferroelectric materials that have been investigated so far for the fabrication of ferroelectric memories [1, 3, 14]. One of the first materials to be used in the design of ferroelectric memory was potassium nitrate (KNO_3) by General Motors laboratory. It is an excellent ferroelectric with extremely sharp and well defined coercive field, E_c. But the hygroscopic nature of KNO_3 makes it poorly suited for device processing [1, 18]. The advent of the new thin film deposition techniques such as sputtering made the thin films of lead-based ferroelectrics popular [19, 20]. The high polarization and low coercive field of these perovskites make them an important candidate for ferroelectric memory. $Pb(Zr_xTi_{1-x})O_3$ (PZT) is a widely used material in this family [2]. It is reported that doping lanthanum, calcium, and strontium improved PZT's low voltage performance, hydrogen-degradation resistance, retention and imprint

9

performance [2, 3, 14]. The recent growth of PLZT thin films by hydrothermal technique at a very low reaction temperature (< 200 °C) opens up the possibility of preparing ferroelectric capacitors at low temperatures [21]. Many of the commercially available ferroelectric memories are manufactured using PZT thin films prepared either by sputtering or sol-gel deposition [14, 15, 19, 20]. The low crystallization temperature of PZT makes it an attractive candidate for integration into complementary metal oxide semiconductor circuitry [1, 3]. The degradation factor imprint in the PZT capacitor can be reduced by doping Nb into PZT forming $Pb(NbZrTi)O_3$ [22]. This is also reported to reduce the crystallization temperature of PZT layer [23]. $Ba_{1-x}Sr_xTiO_3$ (BST) is a new candidate among the perovskites for memory applications. The large dielectric constant and fatigue free nature of BST makes it an interesting candidate [24, 25]. The good dielectric tunability of the material makes it suitable for various microwave devices such as voltage tunable phase shifter, decoupling capacitor and tunable filters [26].

Layered perovskites is another more recently developed family of ferroelectric materials. In these materials the oxide layers interleave the perovskite layers in the lattice structure. $SrBi_2Ta_2O_9$ (SBT) is a well studied member in this family [14, 27]. The direction of spontaneous polarization is along the a-axis of the crystal, while the preferred orientation in an SBT film is c-axis. Therefore a randomly oriented polycrystalline SBT films are usually used in FeRAM applications. Compared to PZT, SBT promises better endurance characteristics such as fatigue, imprint and low voltage operation below 1 V. The memory devices using SBT is found to have fatigue endurance up to 10^{10} cycles. But the high crystallization temperature and lower remanent polarization makes the integration of SBT capacitors difficult [3, 28].

1.4 Degradation Factors

The ferroelectric thin film should have the following characteristics in order to fabricate a capacitor type FeRAM;

(i) Remanent Polarization should be large enough so that a large polarization reversal current can be derived from a small area of the capacitor.

(ii) Low dielectric constant is preferable, because a high dielectric constant material produces a large displacement current and it disturbs the detection of the polarization reversal current.

(iii) Low coercive field is preferable for the low voltage operation of FeRAM [3, 14, 23].

There are many process technologies to be solved before making FeRAM a universal memory. A fundamental problem was the lack of reproducible deposition methodology to generate ferroelectric thin films. The lack of production worthy deposition process adversely impacted the long term reliability performance of any films that were produced. As the thin film technology materialized, all the fundamental problems were solved and focus shifted to improving the performance of the nonvolatile memories by circumventing the degradation factors [14, 15, 19, 20]. The major degradation factors that can limit the use of ferroelectric random access memories are fatigue, logic state retention loss and imprint [3, 14, 29].

1.4.1 Fatigue

A ferroelectric capacitor should undergo large number of read write cycles to store and retrieve data. The switching polarization is the charge available (Q_{sw}) for the ferroelectric as the polarity is changed. Repeated cycling of the ferroelectric capacitor will decrease the value of Q_{sw} and eventually the value will be so low to be detected, resulting in the loss of information. This loss of the switchable polarization due to repeated cycling of the hysteresis loop is

known as fatigue [3, 14, 28-30]. For example a reduction of the remanent polaraization to 50% of its initial value was observed for PZT capacitor using Pt as the electrode [3, 30, 31]]. Figure 1.3 shows the fatigue characteristic of PZT capacitor using conventional electrode Pt in comparison with perovskite oxide electrode LaNiO$_3$ [3, 28, 32].
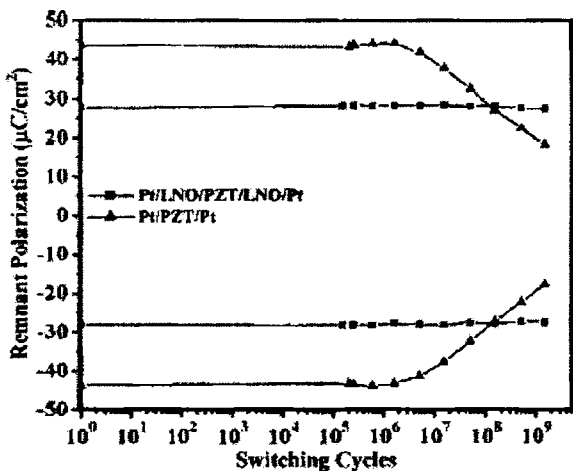
Figure 1.3. Fatigue characteristics of Pt/LNO/PZT/LNO/Pt capacitor and Pt/PZT/Pt capacitor (from [32])

Several mechanisms have been proposed to explain the fatigue phenomena in ferroelectric thin films. Most widely accepted proposal for the fatigue phenomena is the defect entrapment at the ferroelectric-electrode interface and/or at the grain and domain boundaries [30-35]. For example in the case of PZT capacitors oxygen vacancies are the prominent ionic defects. These oxygen vacancies could release two electrons upon ionization. These electrons could get trapped at the Ti^{4+} sites reducing it to Ti^{3+}. This can result in development of a space charge in the neighborhood of the film electrode interface or at the grain or the domain boundary. As the fatigue proceeds domain splitting occurs and domain boundaries are created. Therefore a reduction in the switchable charge is

observed due to increased pinning at the domain boundaries. Therefore the switchable polarization decreases with increasing polarization reversal [34, 35]. The electrical breakdown in the fatigue process is due to the hopping conduction between the small domains. There is also an increase in the carrier trap density with switching of cycles. These traps which are complex defects further contribute to fatigue [36].

Several phenomena which are observed in the fatigue mechanism of the ferroelectric thin films can be summarized as follows. The use of conductive perovskite oxide as the bottom electrode improves the ferroelectric-electrode interface and provides fatigue endurance up to 10^{10} cycles. It reduces the high angle grain boundaries of the ferroelectric layer and gave a better crystallographic orientation to the ferroelectric layer [31-33]. A better fatigue endurance up to 10^{12} cycles was observed for those capacitors using the conductive oxide layer as both top and bottom electrode [32, 33, 37]. The use of a template layer beneath the perovskite bottom electrode could increase of switchable polarization and fatigue resistance due to the preferred c-axis growth of the ferroelectric layer [37, 38]. Also the use of a buffer layer between the PZT and Pt bottom electrode could improve the fatigue performance of the PZT capacitor [39, 40]. For example by using $PbZrO_3$ as the buffer layer the Pb vacancies during the sintering process of the PZT film is compensated. This suppresses the formation of associated oxygen vacancies which are the only mobile ionic defects in the perovskite structure causing the fatigue phenomena [39]. The Zr/Ti ratio of PZT thin film is also found to affect the fatigue behavior. A gradual decay in the fatigue profile after 10^6 cycles was observed in the capacitor using PZT film with relatively small Zr/Ti ratios such as 10/90. The optimal composition for the PZT capacitor to be almost fatigue free is found to be for a Zr/Ti ratio of 40/60 [41]. Therefore in the present study we have made use of Zr/Ti ratio 52/48 which is close to the optimal ratio.

13

1.4.2 Imprint

The preference of a certain polarization state over the other in ferroelectric bistable states is known as imprint. The imprint phenomena exhibit itself as an asymmetry in the hysteresis loop of the ferroelectric capacitor [42-44]. This asymmetry leads to the reduction in the value of one of the remnant polarization states. If the shift is large enough, the two polarization states become indistinguishable which eventually leads to failure [43, 44]. There are various reasons for the occurrence of imprint. Dipolar defect complexes in the thin film, asymmetric distribution of charged defects, and/or charge trapping are suggested as possible causes for the asymmetric behavior of ferroelectric capacitor. The main defects in the ferroelectric thin films are oxygen vacancies. Therefore the oxygen vacancies in ferroelectric-electrode interface determine both the imprint and fatigue in ferroelectric thin films [44- 47].
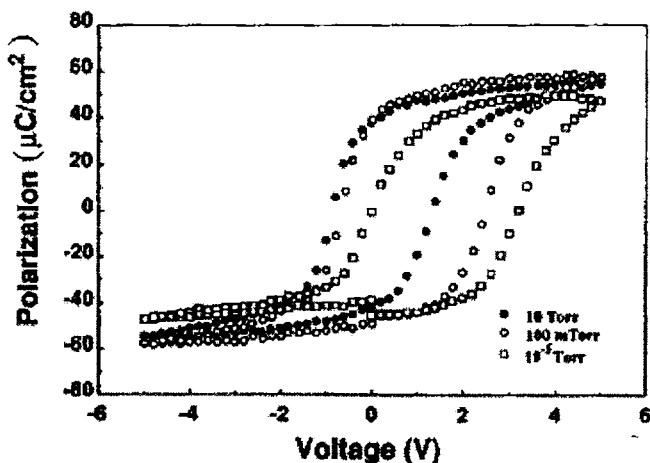
Figure 1.4. Polarization vs Electric field (PE) hysteresis loop of LSCO/PLZT/LSCO capacitor cooled in different oxygen ambient. The loop is more positively biased as the cooling atmosphere becomes more reducing (from [44])

The oxygen vacancies and the related defects are responsible for the measured voltage offset and imprint in the ferroelectric capacitor [42-44]. The imprint of

the LSCO/PLZT/LSCO capacitor was found to be enhanced (figure 1.4) by cooling the films in reducing atmosphere. The use of a dc bias or a unidirectional pulse under isothermal condition can reduce the voltage offset. But the hysteresis loop will move towards the original voltage offset condition if the capacitor is maintained in the original polarization state. The rate of this process depends on the temperature and degree of oxygen deficiency on the top LSCO electrode as opposed to the bottom electrode. But capacitors cooled in fully oxidizing atmospheres shows symmetric hysteresis loop and little imprint [35, 42, 44]. The asymmetric configuration of the top and bottom electrodes leads to asymmetric band bending due to the different work function of the top and bottom electrodes causing imprint [44]. But a slight variation in the composition of the top and bottom electrode will not affect the ferroelectric properties [30]. The imprint phenomena in the ferroelectric capacitor can be tackled by the use of identical top and bottom electrodes which facilitates symmetric switching on both sides of the ferroelectric [30, 44].

1.4.3 Retention

Memory devices should have good retention characteristics. When a capacitor maintains a polarization state and clearly discriminate it from the opposite state for almost indefinite time, it is said to possess good logic state retention. A capacitor can be tested for logic state retention by writing the capacitor with a pulse of one polarity and subsequently reading it with two pulses of opposite polarity, thereby simulating a logic "0" state and logic "1" state read. The delay between the read and the write pulse is the retention time [14, 29, 30]. The capacitor with symmetrical composition for the electrode was found to have better retention properties [30]. For the capacitor with asymmetric electrodes better retention was obtained for negative pulse compared to positive pulse.

The empirical relation

$$Y = 1 - e^{-Kt^m}$$ (1.1)

explains the phenomena. K and m are empirical constants, t is the retention time, Y normalized polarization loss and 1-Y is the normalized retained polarization. The retention loss can be explained considering a random walk process. The constants K and m define the rate of decay of the retained polarization or retention loss. They are related to degradation factors such as depolarizing fields and strains in the capacitor and can be used as a measure of back switching of domains. With smaller values of m and K the capacitor would retain more polarization and m = 0 is the ideal case with no polarization. The retention failure of the capacitor using asymmetric electrodes with positive polarity read is due to the fact that the positive pulses make the capacitor more symmetric by lowering its polarization [29, 30].

Most of the degradation factors of the ferroelectric memory devices can be circumvented by the appropriate choice of the electrode materials. The electrode material has direct influence on the nucleation, microstructure and electrical properties of the ferroelectric material [28, 41, 48, 49]. The electrode must have low resistance, better adhesion to the ferroelectric and layers under the electrode and should provide chemically stable environment for the growth of ferroelectric material and operation of the device [41, 48]. The electrode materials can be classified into two major categories;

    (i) Conventional electrodes which includes

        (a) Noble metal electrodes such as Pt, Au, Ir, Ru, Al etc

        (b) Rutile type oxides such as IrO_2, RuO_2

        (c) Conductive oxides such as ITO and

    (ii) Conductive perovskite oxides including LNO, LSCO, SRO [34, 50-58].

1.5 Conventional Electrodes

The most commonly used electrode for ferroelectric memory devices is Pt due to its high electrical conductivity [1, 28, 44, 59]. Ferroelectric memory devices are fabricated using high permittivity metal oxides which require high temperature for crystallization. Pt being a noble metal does not oxidize readily when subjected to high temperatures. Thus the formation of a low dielectric constant layer which can in turn reduce the field across the high permittivity metal oxide is avoided by the use of Pt electrode. Pt also acts as a good diffusion barrier [53]. But one of the major drawbacks of the ferroelectric devices using Pt electrode is fatigue [3, 30, 31]. Also the morphological inhomogeneties developed in the Pt layer during its growth lead to low breakdown voltage of the ferroelectric layer. Therefore Pt layer should be generally patterned either by photolithography or by plasma etching [60].

The fatigue phenomena in the ferroelectric capacitors with Pt electrode have been investigated in detail. The oxygen vacancies near the electrode ferroelectric interface are the primary mechanism for the fatigue in ferroelectric memory devices [30-35, 42]. Pt also forms Schottky contact to the ferroelectric layer limiting the leakage current. It is the charge trapping at the defect centers that leads to the reduction in the leakage current [34]. It was found that the oxygen depletion layer near the Pt electrode moves into the ferroelectric thin film after fatigue. This is due to the formation of platinum oxide at the electrode surface by the recombination between the Pt and the oxygen ion released during the reduction process [46]. A recent investigation on the fatigue behavior over a wide range of temperature revealed that the temperature and electric voltage are the key factors determining the oxygen vacancy migration in the PZT capacitors with Pt electrodes. Even though the fatigue endurance was significantly improved at low temperature, an increase in fatigue was observed with the increase in the magnitude of the electric pulses [50].

17

The crystallinity and surface morphology of the Pt bottom electrode was found to influence the ferroelectric properties of the BST and PZT layer grown over it. The optimized Pt layer formed with (111) preferred orientation and smooth surface morphology produced better ferroelectric properties in both Pt/BST/Pt and Pt/PZT/Pt capacitors [60]. The fatigue endurance of the ferroelectric capacitor using Pt bottom electrode has been increased by the use of a perovskite oxide layer between the bottom Pt layer and the ferroelectric layer. Fatigue characteristics of the PZT capacitors with various metallic oxides layer such as MgO, CeO_2, Mn_2O_3, and LSCO between PZT and the Pt bottom electrode revealed that the fatigue resistance of the PZT thin film capacitors was found to increase as the degree of nonstoichiometry of the metallic oxide layer increases. The nonstoichiometry of the oxides was found to alleviate the oxygen vacancies at the interface thereby reducing the fatigue [40].

Ir which belongs to the same group as Pt and has similar properties as Pt, is also another conventional electrode used in ferroelectric memory [52]. It is more commonly used as a stacked electrode along with its conductive oxide IrO_2 in the form Ir/IrO_2 when the interconnection of the capacitor to the periphery circuit is considered [52, 61]. IrO_2 being a conductive oxide prevents the connection failure due to the oxidization of the interconnect material such as Al, Cu, Ti or TiN during fabrication [62]. IrO_2 is even more advantageous due to the fact that it has good heat resistance and can act as a diffusion barrier. A well crystallized smooth morphology was obtained for Pt layer when IrO_2 was used as a barrier between the Pt and the substrate. This in turn resulted in a smooth morphology for the PZT layer on top of it and gave fatigue endurance up to 10^{12} cycles [52]. The oxygen partial pressure during the growth of IrO_2 was found to influence the ferroelectric properties due to the reaction between IrO_2 and PZT due to oxygen ion bombardments [61]. Even though the device exhibited good ferroelectric properties with fatigue endurance up to 10^{11} cycles the interfacial phases between the PZT and the electrode layer resulted in a high leakage current density.

18

Ru is another conventional electrode material used in the fabrication of ferroelectric memory. The ferroelectric properties and fatigue resistance of the capacitors using Ru and RuO_2 as the electrode material were found to be slightly better (10^7 cycles) than that using Pt electrodes [63]. Even though there are reports on the low temperature growth of the PLZT over Ru electrode, the remnant polarization was found to decrease to half its initial value after 10^5 cycles [53]. Al is another metal electrode that can be used for PZT capacitors. But PZT crystallizes in a cubic non ferroelectric phase when deposited over Al leading to poor ferroelectric properties [54].

Fatigue resistance for the ferroelectric capacitor can be achieved by the use of conductive oxides as the electrode material. The oxide electrodes do not form blocking contacts to the oxygen vacancies in the ferroelectric thin film thereby avoiding space-charge build up and fatigue [34, 42-44]. ITO is a conventional conductive oxide electrode used for ferroelectric capacitors. ITO being a transparent conductor can be used for the fabrication of light sensitive devices using PZT. Photo stimulation effects of the charge carriers in the PZT thin films can be measured using ITO as the electrode material. ITO being permeable to oxygen vacancies reduces the charge build up at the PZT-ITO interface and gave fatigue endurance up to 10^8 cycles. But the significant inter diffusion between the ITO and the ferroelectric thin films results in high leakage current and poor ferroelectric properties [55, 64, 65].

Cuprate superconductors are another electrode material that can be used for ferroelectric memory devices as ferroelectric thin films could be grown epitaxially on them [66-68]. The crystallographic orientation of the ferroelectric layer is found to influence the fatigue characteristics. Better fatigue properties have been observed for epitaxial thin film heterostructure of ferroelectric material and cuprate superconductor YBCO ($YBa_2Cu_3O_{7-x}$) electrodes grown by pulsed laser deposition [69]. But the properties of the YBCO thin film depend largely on the accurate control of the deposition and the post deposition

processing parameters. Also the deposition temperature of the YBCO thin film is larger (800 °C) when compared to the PZT thin film (600 °C), which make the device integration difficult. The rough surface morphology of the YBCO thin film due to the generation of "boulders" and other smaller sized particles during PLD process resulted in a rough surface for the PZT film grown on top of it. Also the YBCO thin films need to be grown with c-axis orientation to facilitate its use as conductive electrode material [66-69].

1.6 Conductive perovskite oxide electrodes

The use of conductive perovskite oxides as electrode for ferroelectric memory devices is appropriate solution for the various degradation mechanisms in the memory device [3, 14, 28-31]. Perovskite electrodes have pseudocubic structure similar to that of the ferroelectric material. The lattice match between the two facilitates high quality epitaxial ferroelectric heterostructure [31, 70-73]. Perovskite oxides are chemically stable at both oxidizing and inert atmospheres [74, 75]. This is favorable for device integration as ferroelectric materials are usually grown at high deposition temperature (~ 600 °C) [70, 71, 76]. The similar crystal structure of the electrode layer provides appropriate nucleation sites for the growth of perovskite ferroelectric layer [29-31, 77, 78]. These electrodes being conductive oxides will act as oxygen vacancy sink thereby limiting the accumulation of oxygen vacancies at the ferroelectric-electrode interface [33-35, 42-44]. Therefore the major degradation factors such as fatigue and imprint are considerably alleviated. These conductive oxide layers also acts as protective barriers during device fabrication [53, 63]. Another feature is the isotropic low resistivity of these materials. The typical room temperature resistivity of these materials are between 90-100 $\mu\Omega$cm. Also the temperature dependence of resistivity of these materials shows a metallic nature which is an important prerequisite for electrode applications [31, 79-81]. The various conductive perovskite oxide electrodes which are commonly investigated are $SrRuO_3$, $LaNiO_3$ and $La_{0.5}Sr_{0.5}CoO_3$.

1.6.1 SrRuO₃

SrRuO$_3$ is an isotropic metallic oxide with pseudocubic perovskite structure. The small lattice mismatch (~ 2.7%) between SrRuO$_3$ (a = 3.93 A°) and PZT (a and c values are 4.036 A° and 4.146 A° respectively) allows the growth of high quality ferroelectric heterostructure. SrRuO$_3$ has high chemical stability up to 1200 K in both oxidizing and reducing atmospheres [31, 82]. It has got a very low resistivity at room temperature (340 μΩcm) and the temperature dependence of resistivity shows a metallic behavior. Doping Ca yields Sr$_{1-x}$Ca$_x$RuO$_3$ ($0 \leq x \leq 1$), which is also a pseudocubic perovskite. The lattice parameter of this compound can be tuned by varying the Sr/Ca ratio which enables the growth of epitaxial multilayer with many oxide materials with excellent lattice match [80]. SrRuO$_3$ can also be used as a buffer layer for memory devices using PZT. The SrRuO$_3$ layer reduces the interfacial defect density and enhances the ferroelectric properties with high remanent polarization and superior imprint characteristics [83].

PZT capacitor fabricated using SrRuO$_3$ electrode showed better ferroelectric property with increased remanent polarization and fatigue endurance (10^{10} cycles) due to the better interface properties [31]. The electrical and microstructural properties of the BST capacitor using SrRuO$_3$ as the bottom electrode revealed a "local epitaxial film" which gave a low leakage current (10^{-7} A/cm^2) for the capacitor [84]. A comparative study on the epitaxial growth of the PZT on SrRuO$_3$ and LSCO bottom electrode was carried out by Cho et al. [85]. The PZT film grown on LSCO showed a (001) oriented heteroepitaxial growth. But the growth of PZT on SrRuO$_3$ was found to depend on the substrate temperature used for the deposition of SrRuO$_3$ and it influenced the ferroelectric properties also. The PZT film showed a tetragonal mixture of (001) and (h00) heteroepitaxial growth on SrRuO$_3$ and does not show a good saturation polarization at low maximum driving voltage.

1.6.2 LaNiO₃

LaNiO$_3$ is an isotropic n-type metallic conductor with room temperature resistivity as low as 150-210 μΩcm. It has a pseudocubic perovskite structure with lattice parameter 3.84 A$^\circ$ [86, 87]. LaNiO$_3$ can be grown epitaxially on lattice matched substrates at low substrate temperature [32, 88-90]. Compared to other perovskite oxides LaNiO$_3$ can be fully oxidized at lower oxygen partial pressures [88, 89]. The electrical and structural properties make LaNiO$_3$ a potentially good candidate for electrodes and buffer layers in ferroelectric memory and MEMS devices. (100) and (001) oriented PZT films with good ferroelectric properties could be grown on LaNiO$_3$ bottom electrode prepared at a substrate temperature in the range 200-500 $^\circ$C on SiO$_2$/Si substrates [86]. The growth on SiO$_2$/Si substrates is particularly important considering device integration using Si semiconductor technology. An investigation on the ferroelectric properties of PZT capacitor using different electrode combinations revealed that a better fatigue endurance was shown by the capacitor using LaNiO$_3$ as electrode on the both sides [33].

The post deposition annealing condition was found to affect the ferroelectric properties of PZT capacitor using LaNiO$_3$ as the electrode [90]. Samples annealed in air and oxygen yielded complete perovskite phase and that annealed in nitrogen had random orientation with pyrochlore phase. The pyrochlore phase in the samples annealed in nitrogen resulted in poor ferroelectric behavior with slim hysteresis loop. LaNiO$_3$/PZT/ LaNiO$_3$ capacitor prepared by conventional spin coating combined with rapid thermal annealing (RTA) gave better spontaneous polarization and remanent polarization for the capacitor [32]. The fast temperature ramping rates and short annealing time in RTA suppresses the intermediate layer formation and resulted in good ferroelectric properties. SrTiO$_3$/TiN can be used as the buffer layer for the PZT capacitor using LaNiO$_3$ as the electrode material. The device had a smooth and crack free epitaxial heterostructure with good ferroelectric property and fatigue endurance up to

10^8 cycles [91]. Recently Che et al. [81] investigated of the ferroelectric properties of the PZT capacitor prepared on Ti foils using $LaNiO_3$ buffer layers at varying thickness. An optimum $LaNiO_3$ thickness of 150 nm mitigates the lattice mismatch and Ti diffusion between the PZT thin film and Ti substrate resulting in significant decrease in the leakage current density. The excellent electric and dielectric properties of PZT thin films deposited on $LaNiO_3$ buffered Ti foils makes it a promising candidate for microelectronic device applications.

1.6.3 $La_{0.5}Sr_{0.5}CoO_3$

$La_{0.5}Sr_{0.5}CoO_3$ (LSCO) is a p-type conductive oxide with a cubic perovskite structure [30, 41, 92, 93]. The structural compatibility of LSCO (a = 3.83 A°) with lead based ferroelectric materials (a = 3.93 - 4.3 A°), makes it an ideal growth surface for the ferroelectric layer. Epitaxial growth of the ferroelectric layer is facilitated over LSCO due to the same crystal structure and the lattice match between the two [37, 70-72]. LSCO is also an isotropic conductor with room temperature resistivity as low as 90 $\mu\Omega$cm, which makes it an ideal electrode material [81, 84]. The good thermal and chemical stability makes it a suitable candidate for device integration [75, 78, 94]. LSCO is having large oxide ion diffusivity due to the large oxygen non stoichiometry in the compound. Therefore it effectively reduces the polarization fatigue as it acts as a sink for oxygen vacancies, which are the major ionic defects causing fatigue [33, 42, 93, 95]. This property of LSCO also reduces effectively the imprint behavior of ferroelectric capacitor [30, 35, 42]. LSCO can be grown at the similar growth conditions of the ferroelectric layer, ie at lower substrate temperature compared to other perovskite electrodes [48, 37]. This is particularly interesting considering the device integration. LSCO can promote perovskite phase formation not only of Pb-based ferroelectrics, but also of other ferroelectric materials such as $Ba_{1-x}Sr_xTiO_3$ [48, 96].

23

One of the earlier studies on the use of LSCO as an electrode material for ferroelectric capacitors was carried out by Ramesh et al.[37]. The capacitor structure LSCO/PLZT/LSCO was grown by PLD on to Si [001] substrate with yttria stabilized zirconia buffer layer. The large lattice mismatch between the yttria stabilized zirconia (a = 5.16 A^o) and LSCO resulted in poor ferroelectric properties with the capacitor showing a leaky dielectric behavior. But the use of a very thin non conducting template layer, $Bi_4Ti_3O_{12}$ between the yttria-stabilized zirconia buffer layer and the LSCO bottom electrode resulted in better ferroelectric properties as it provided suitable surface for the growth of LSCO and PZT layer. The device showed excellent retention and fatigue endurance up to 10^{12} cycles. The effect of scaling on the ferroelectric property of the PZT capacitor by Ramesh et al. [97] revealed that the ferroelectric properties of the small capacitor were commensurate with the discrete capacitor. This was one of the earliest studies on the effect of scaling on the ferroelectric properties and was very relevant with respect to the ultimate application of the capacitors in high density non volatile memories.

There have been substantial studies on the growth of PZT/LSCO heterostructure on various conditions to check the possibility of using them for ferroelectric memory devices [23, 37, 41, 42, 44, 57, 70, 85, 91, 98-100]. The PZT/LSCO heterostructure fabricated on MgO substrate facilitated an epitaxial growth of LSCO which produced a polycrystalline PZT layer over it. The LSCO on SiO_2/Si substrate was polycrystalline in nature, and it prevented PZT from forming as perovskite crystallites [70]. The imprint behavior of the PZT capacitor with LSCO was improved by doping Niobium with PZT forming PNZT [57]. The PNZT/LSCO heterostructure with good ferroelectric properties could be at prepared at low process temperature [57, 23]. Wang et al. [100] demonstrated a simple method of preparing ferroelectric capacitors directly on to Si substrate by chemical solution route. The LSCO and the PZT layers were found to be polycrystalline with no pyrochlore phase and were able to get better fatigue endurance up to 10^9 cycles. Better ferroelectric properties could be

obtained when a double electrode structure of the form oxide electrode/Pt was used rather than using oxide electrode alone as the bottom electrode [101].

The oxygen deficiency of the LSCO electrode was found to affect hysteresis relaxation of the PLZT capacitor [30, 35, 42, 73, 93]. The capacitors developed an internal field when the oxygen content in the film was reduced. But fully oxygenated samples showed no imprint. Also the hysteresis loop of the LSCO/PLZT/LSCO capacitor cooled in reducing atmosphere developed a voltage offset with the internal field directed from the bottom to the top electrode. An oxygen vacancy gradient is created in the LSCO/PLZT/LSCO stack with more vacancy concentration at the top electrode [30, 42, 93]. When one of the electrodes was replaced with $LaCoO_3$ (LCO), the capacitor developed asymmetric switching behavior and imprint failure [102]. But a slight variation in the composition of the LSCO electrode did not affect the ferroelectric properties of the PNZT capacitor [30]. Even though some asymmetry was found on the hysteresis loop, it had the same imprint and retention properties compared to the capacitor with symmetric LSCO electrode.

Ferroelectric thin films require high temperature for crystallization. The oxygen contained in the film and or in the annealing ambient can penetrate through the bottom electrode during the high temperature processing leading to degradation of contact resistance. The reaction between each layer can also lead to high leakage current for the ferroelectric film. The large thermal and chemical stability makes LSCO a better diffusion barrier. LSCO was used as a buffer layer for the fabrication of PZT capacitors using Ir and Ru as the bottom electrode on poly-Si/SiO$_2$/Si substrate [103]. The PZT layer deposited over Ir/poly-Si/SiO$_2$/Si and Ru/poly-Si/SiO$_2$/Si was found to develop perovskite structure without any pyrochlore phase. PZT on LSCO/Ir/poly-Si/SiO$_2$/Si had a (100) preferred orientation which resulted in higher remnant polarization and more saturated hysteresis loop. A comparison of the properties of the heterostructures Pt/PZT/LaAlO$_3$/Si and Pt/PZT/La$_{0.85}$Sr$_{0.15}$CoO$_3$/LaAlO$_3$/Si for

25

ferroelectric gate FET memory revealed that the PZT layer grow with (111) orientation over the LSCO layer and provided more polarization charge under the same applied voltage to give a large memory window for the device [104]. The use of LSCO template layer was found to facilitate perovskite grain growth Perovskite $Pb(Nb_{2/3}Mg_{1/3})O_3$ - $PbTiO_3$ could be grown at a at low temperature of 600 °C using LSCO template layer, which otherwise required a post deposition annealing at temperature ranging from 750-800 °C [76].

Certain barrier layers, both conducting and nonconducting has been used in between the substrate and the LSCO bottom electrode layer. The purpose of this layer is to seed the perovskite phase formation on both LSCO and the ferroelectric layer on top. They enhance the fatigue endurance of the capacitor and can also make the memory device durable against repeated polarization switching. Capacitors using amorphous Ti-Al as barrier layers exhibited excellent ferroelectric properties with fatigue resistance up to 10^{11} cycles [105]. Conducting $La_{1-x}Sr_xTiO_3$ used beneath the LSCO layer seeded the (001) oriented epitaxial growth of perovskite PZT and the device exhibited better ferroelectric properties [106]. In a recent study Liu et al. [107] investigated the properties of the PZT thin film sandwiched between conducting and non conducting oxides. Ferroelectric capacitors of $Bi_{3.25}La_{0.75}Ti_3O_{12}/PbZr_{0.4}Ti_{0.6}O_3/ Bi_{3.25}La_{0.75}Ti_3O_{12}$ and $La_{0.5}Sr_{0.5}CoO_3/ PbZr_{0.4}Ti_{0.6}O_3/ La_{0.5}Sr_{0.5}CoO_3$ were fabricated on Si substrates. The good interface and the conductivity of LSCO resulted in better crystallinity and higher polarization for PZT capacitor with LSCO electrodes compared to that of $Bi_{3.25}La_{0.75}Ti_3O_{12}$ electrodes. As the non conducting $Bi_{3.25}La_{0.75}Ti_3O_{12}$ layer can act as a diffusion barrier, the leakage current density of the capacitor using $Bi_{3.25}La_{0.75}Ti_3O_{12}$ layer was one order less than that using LSCO. The use of $SrTiO_3$ as a template layer for the LSCO bottom electrode for the PZT capacitor strengthened the adhesion of the PZT layer to the substrate. $SrTiO_3$ layer was found to be detrimental in texturing the PZT layer and the capacitor gave fatigue endurance up to 10^{10} cycles [41]. The fabrication of LSCO/Pb-Nb-Zr-Ti-O/LSCO capacitor on platinized conducting barrier layer of TiN/poly-

Si/Si substrate for integration into high density non volatile memory devices has been investigated by Dhote et al. [98]. The use of the Pt layer reduces the sheet resistance of the bottom electrode and it realized three dimensionally stacked capacitor-transistor geometry with direct contact to the memory capacitor.

1.7 Other Applications of LSCO

Perovskite oxides are potential candidates for a number of high temperature electrochemical processes such as solid oxide fuel cells (SOFC), electrolysis, oxygen reduction, oxygen sensors, and oxygen separation membrane [108-125]. The properties required for these applications are either possessed by perovskite oxides or can be tailored by substitution of a wide range of cations onto the lattice [13, 108]. The major requirements for electrochemical applications are

> (i) thermodynamic stability over the applicable temperature and oxygen activity range
>
> (ii) sufficient electrical conductivity
>
> (iii) chemical stability
>
> (iv) mechanical stability ie having sufficient strength and thermal expansion match and mixed electronic and ionic conductivity, particularly important for SOFC cathode, catalysis, oxygen separation membranes.

The major electrochemical applications of LSCO are as cathode for SOFC, in oxygen separation membranes and in gas sensors.

1.7.1 Cathode for SOFC

Solid oxide fuel cells of micro meter size can revolutionize the means by which portable electronic devices are powered [112, 113]. They offer power densities much greater than conventional lithium batteries and can be instantaneously recharged with readily available hydrocarbon fuels. The thin solid electrolyte films, coupled with Si MEMS technology offer the possibility of highly

27

integrated system-on-a-chip [112]. The most significant limitation encountered in SOFC is the corrosion of cathode at cathode leads by oxygen at working temperature. The operating temperature of these devices are about 1000 °C in air or oxygen and the cathode material has to meet the following requirements such as high electronic conductivity, thermal and chemical stability, compatibility with the solid electrolyte, sufficient porosity, and good adherence at the surface of the electrolyte [113]. Noble metals or conducting metal oxides are usually used as electrode material. The mixed ionic and electronic conductivity and good catalytic behavior makes $La_{1-x}Sr_xCoO_3$ a strong candidate for cathode of SOFC [108, 109, 113]. The presence of oxide ionic conductivity in the background of high electronic conductivity for $La_{1-x}Sr_xCoO_3$ leads to a substantial improvement in the electrochemical property of the electrode, due to the expansion of the electrochemical reaction zone. $La_{1-x}Sr_xCoO_3$ is having high thermal expansion coefficient and reacts readily with the yttria stabilized zirconia (YSZ) electrolyte in SOFC [109, 112, 113].

Among the $Ln_{1-x}Sr_xCoO_3$ (Ln = La, Pr, Nd) solid solution, $La_{1-x}Sr_xCoO_3$ was found to have the maximum oxygen permeability [109]. Bieberle-Hutter et al. [112] carried out a detailed investigation on the electrical conductivity and electrochemical properties of the $La_{1-x}Sr_xCoO_3$ as the electrode for SOFC. Electrical conduction in $La_{1-x}Sr_xCoO_3$ was found to strongly depend on the deposition condition; particularly the oxygen partial pressure. Quartz was found to be the most suitable substrate for the growth of $La_{1-x}Sr_xCoO_3$ for SOFC application. The microstructure of the electrode material is an important criterion determining the properties of the SOFC. The oxygen adsorption/desorption rate was to be faster on the $La_{1-x}Sr_xCoO_{3-\delta}$ electrode with smaller grain size [114]. The oxygen diffusivity measurement by Routbort et al. [115] on various composition of $La_{1-x}Sr_xCoO_3$ revealed that $La_{0.8}Sr_{0.2}CoO_3$ has the largest oxygen diffusivity to be useful as a dense electrode in a low temperature SOFC. $La_{0.7}Sr_{0.3}MnO_3$ (LSMO) is found to be the most adaptable electrode for SOFC due to its electrical conductivity, good catalytic activity for

oxygen reduction and good chemical stability with YSZ electrolyte [113]. The recent investigation on LSMO suggested the use of a composite electrode LSMO-YSZ as the most suitable electrode for SOFC using YSZ as the electrolyte. Recently an improvement in the performance of the composite electrode LSMO-YSZ was found by the addition of $La_{0.8}Sr_{0.2}CoO_3$ layer on the top of the existing LSMO electrode layer [116].

1.7.2 Ceramic membrane

Ceramic membranes are designed to separate oxygen from air. There are stringent requirements on the material to be used as oxygen separation membrane. The material is expected to have an optimum range of mixed conductivity, high degree of oxygen non stoichiometry, structural stability and thermal expansion compatibility through out a wide range of oxygen activity [110]. Perovskite oxides with their mixed conductivity are a promising candidate for oxygen separation membranes [117-119]. High oxygen fluxes have been measured through oxides with perovskite structure [110, 117-119]. $La_{1-x}Sr_xCoO_3$ being a high temperature mixed conductor can be used for oxygen separation and catalytic oxidation. The electrochemical separation involves the reduction of oxygen on one side of a dense $La_{1-x}Sr_xCoO_3$ membrane and subsequent reoxidation of O^{2-} at the other side of the membrane. The pressure gradient of oxygen across the membrane provides the driving force for the migration of O^{2-} ions in the lattice of $La_{1-x}Sr_xCoO_3$. The electronic conductivity provides a return path for electrons so as to balance the current of oxygen ions in the absence of an external electrical field. These thin films are to be supported on porous substrates for sufficient mechanical stability and to allow the membrane accessible by the reacting species [120].

In one of the earlier studies on the use of perovskite oxides as dense ceramic membranes, Bouwmeester et al. [110] has provided a theoretical approach on the influence on the surface exchange kinetics as rate determining step in mixed

conducting oxides. The oxygen flux through the perovskite was found to be proportional to the oxygen ion conductivity of the material. Reducing the thickness of the membrane increases the oxygen flux and reduces the operating temperature of the device. High surface exchange rates are prerequisite to sustain high oxygen fluxes through the membrane. The possibility of using a symmetric porous support for the ceramic membrane was investigated by Hong et al. [120]. The normally used asymmetric support can give rise to inevitable cracking in the support membrane upon sintering due to large shrinkage mismatch between the membrane and underlying support. A symmetric support for the $La_{0.2}Sr_{0.8}CoO_{3-\delta}$ (LSCO-80) membrane can be realized by depositing Co metal on to the packed LSCO-80 powder layer [120]. The Co metal can penetrate into the powder packed layer through the inter-particulate space, resulting in a Co/LSCO-80 composite which gives a CoO/LSCO-80 composite membrane after sintering. The oxidation of Co during sintering causes a structure expansion, which exerts a compressive stress on LSCO-80 phase. Therefore the tensile stress applied by the support is effectively buffered. Introducing Pd/Ag alloy into the LSCO-80 membrane could also reduce the mechanical cracks in the membrane caused by thermal mismatch between the membrane and the asymmetric support [121]. Hong et al. [122] prepared crack free porous LSCO-80 thin film on MgO substrate by the use of Ag coating on top of LSCO-80 powder casting layer prior to sintering.

1.7.3 Gas Sensors

Environmental pollution and security in the work and domestic ambient atmosphere represent acute problem with high social impact. Therefore intensive research is being carried out for the development of solid-state chemical sensors especially gas sensors [123, 124]. Gas sensors based on semiconductors can be used since they can detect various toxic gases by changing its conductivity due to the absorption and/or desorption on the metal oxide surface. Recently there has been investigation on the use of perovskite oxides as gas sensors [123-126].

The sensing property in these compounds is due to the high catalytic activity to oxygen reduction and oxidation due to the presence of oxygen vacancies [124]. There are commercially available gas sensors based on perovskite oxide $LnFeO_3$ (where Ln = La, Nd, Sm, Gd, Dy) to detect ammonia, $Cr_{2-x}Ti_xO_3$, NO_x [125, 126].

The use of $La_{0.8}Sr_{0.2}Co_{1-x}Ni_xO_3$ thin film for CO detection was carried out by Chiu et al. [111]. Doping Ni to replace Co ion at the B-site can change the electrostatic potential due to their different electron affinities. The sensitivity was found to depend on the film morphology with more porous film being more sensitive. Anh et al. [124] prepared LSCO thin films by PLD and the possibility of using the thin films for H_2O_2 decomposition was investigated. The catalytic H_2O_2 decomposition was found to increase with increase in oxygen vacancies in LSCO. The sensitivity and selectivity of CO gas sensing was improved by using a simple SnO_2/LSCNO heterojunction [127]. The active region is the interface between the two materials which behaves like a pn junction. The XPS analysis of the heterojunction revealed that the gases adsorbed on either side of the heterocontact were oxidized at varying rates. The heterojunction showed higher sensitivity compared to single layer sensors. The sensitivity was found to depend on the doping concentration of Ni and the maximum sensitivity was obtained for a doping of 50 mol% Ni [128].

1.8 ABO₃ perovskites

The wide range of applications in the field of ferroelectricity, piezoelectricity, ferromagnetism, magnetoresistance, superconductivity and ionic conductivity make perovskites an important class of compounds [12, 13, 29, 129]. The broad spectrum of properties exhibited by perovskite transition- and rare-earth metal oxides are due to the following characteristics: (1) innumerable combinations of metal cations can be accommodated within perovskite-related structural systems,

(2) nonstoichiometry ie controlled amounts of ordered oxygen vacancies can be introduced into the structure by reduction/oxidation processes and (3) the design of composite structural systems containing perovskite building units allows fine-tuning electronic and magnetic properties [13]. In this section the various properties of perovskite oxide $La_{1-x}Sr_xCoO_3$ will be discussed. The evolution of the structural, electrical and magneto transport properties of the system with increasing Sr^{2+} content will be considered.

1.8.1 Structural Properties

The perfect perovskite is a simple one with general formula ABO_3, where A is a monovalent or divalent metal ion and B is tetra-or pentavalent one. The ABO_3 structure can be considered in either of the two ways ie; (i) with A atoms at the cube corners, B atoms at the body centers, and the oxygen at the face centers or (ii) as a set of BO_6 octahedra arranged in a simple cubic pattern and linked together by shared oxygen atoms, with the A atoms occupying the spaces between (figure 1.5). The perovskite family is created by doping other types of cations into the stoichiometry and/or introducing anion deficiency. The A cation is usually coordinated by 12 atoms and the B cation is coordinated by 6 atoms. The valence variation at the A cation position can cause distortion or displacement of the oxygen anion array. This result in distortion in the B-cation-centered octahedron and the B cation must have the flexibility to tolerate this effect. The transition metal elements due to their multivalences and their special 3d and 4d electronic configuration are the best candidates for B-cation position and therefore most of the transition metal oxides have perovskite structure. It is the structural evolution of the perovskites and the corresponding cation valence and the coordination for the cations which governs the transport properties of the system [13, 130-132].
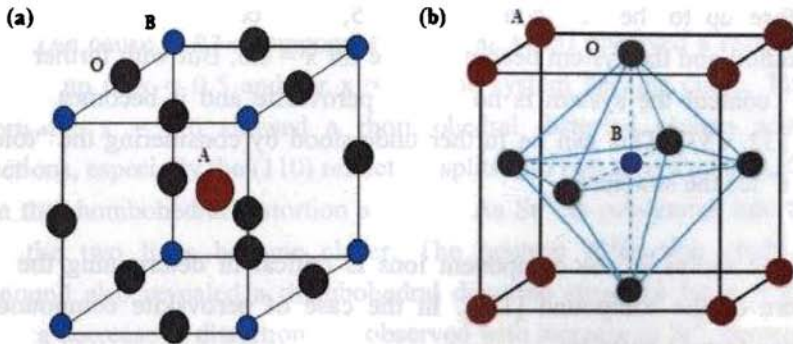
Figure 1.5 ABO$_3$ perovskite structure (a) with the A cation at the centre, B at the corners and oxygen at the edge centers (b) A cation at the corners of the Bravais cell showing the BO$_6$ octahedron located in the A-cation cube

La$_{1-x}$Sr$_x$CoO$_3$ is obtained from the compound LaCoO$_3$ by the partial substitution of La^{3+} by Sr^{2+}. LaCoO$_3$ has a rhombohedral distorted perovskite structure with lattice parameters a = 3.82 Å and α = 90° 42'. When La^{3+} is substituted with Sr^{2+} the rhombohedral distortion of the LaCoO$_3$ system decreases and for Sr^{2+} content x = 0.5 the system is cubic. But with further increase in Sr^{2+} content (x > 0.5) the system becomes tetragonal. The structural evolution of the system with Sr^{2+} substitution can be explained by considering the charge compensation on Sr^{2+} substitution which can occur either by the oxidation of Co^{3+} to Co^{4+} or by the creation of oxygen vacancy, V$_o$. The mechanism can be expressed as [132, 133]

$$La_{1-x}^{3+} Sr_x^{2+} Co_{1-x}^{3+} Co_x^{4+} O_3 \qquad (1.2.a)$$
$$La_{1-x}^{3+} Sr_x^{2+} Co^{3+} O_{3-x/2} V_{ox/2}. \qquad (1.2.b)$$

The former mechanism predominates for Sr^{2+}, x $\leq$ 0.5 and for higher Sr^{2+} content, x > 0.5 the latter mechanism takes over. Jonker et al. [130] conducted a systematic study to determine the oxygen content in the system with varying Sr^{2+} content. A maximum Co^{4+} content of 45% in the system was obtained for

60% Sr^{2+} and with further increase in Sr^{2+} content the Co^{4+} content decreased. Therefore up to the Sr^{2+} content x = 0.5, Co^{4+} content increases with Sr^{2+} substitution and the system becomes cubic for x = 0.5. But with further increase in Sr^{2+} content the system is no longer perovskite and it becomes tetragonal [130, 132, 133]. This can be further understood by considering the "tolerance factor t" for the structure.

The ionic radius of the component ions is critical in determining the crystal structure of the compound [132]. In the case of perovskite compounds, the tolerance factor t given by

$$t = \frac{\sqrt{2}r_A + r_B}{2r_B + r_O} \, ,$$
(1.3)

where r_A, r_B and r_O are the ionic radii of the A, B and O ions respectively determine the crystal structure [13, 132, 134]. The lower limit of tolerance factor for the perovskite structure is around 0.8. A detailed investigation of the structural evaluation of the lanthonoid cobalt oxides with Sr^{2+} doping was done by Ohbayashi et al. [132]. The tolerance factor increases with increase of Sr^{2+} doping and the upper limit of the Sr^{2+} content for perovskite structure is between 0.7 and 0.9 depending on the lanthanoid ion. But in the case of $La_{1-x}Sr_xCoO_3$, for Sr^{2+} content greater than 0.5, the charge compensation results in the creation of oxygen vacancy. The system is no more perovskite due to the disrupted oxygen octahedra around the Co ion and hence the tolerance factor loses it s meaning.

Even though the above theory predicts a cubic structure for the compound with Sr^{2+} content x = 0.5, there are large number of reports stating a rhombohedral distorted structure even for x = 0.5. Raccah et al. [135] investigated the structural properties of $La_{1-x}Sr_xCoO_3$ in the composition range $0 \le x \le 0.5$. The most probable space group for the compound in this composition range was

34

found to be $R\bar{3}C$ at room temperature. But oxygen ion displacements in the system can cause a $R\bar{3}m$ component. Liu et al. [133] observed a rhombohedral structure up to x = 0.5 and for x = 0.6 the system became cubic. The XRD pattern for x = 0.6 showed a rhombohedral distorted system with more reflections, especially the (110) reflection splits into two inequivalent reflections when the rhombohedral distortion appears. As Sr^{2+} is substituted into the La^{3+} sites, the two lines become closer. The neutron diffraction study of the compound also revealed a rhombohedral distorted structure for x = 0.5 even though a decrease in distortion was observed with increase in Sr^{2+} content [136]. Sr^{2+} substitution causes an effective expansion of the unit cell there by reducing the rhombohedral distortion, as the Sr^{2+} ion has larger ionic radius than the La^{3+} ion. The Reitveld analysis of the $Ln_{1-x}Sr_xCoO_3$ by Vanitha et al. [137] also revealed a rhombohedral distorted structure in these compounds up to Ln = Nd.

The structural evolution of the compound is closely related to the observed magnetotransport properties of the system. The observed magnetic susceptibility in the temperature range 400 < T < 650 K for the parent compound $LaCoO_3$ can be correlated with a transition from space group $R\bar{3}C$ below 400 K to $R\bar{3}$ above 650 K [134, 138]. Bhide et al. [138] observed that the discontinuity in the hexagonal c axis C_H as well as the rhombohedral angle α_R of the compound at x = 0.125 were consistent with the change at x = 0.125 from isolated magnetic islands in paramagnetic host to paramagnetic islands in ferromagnetic host. Racch et al. [135] interpreted the discontinuity observed in the α_R and C_H in the composition range 0.1 < x < 0.15 as a chemical inhomogenity separating the strontium-free regions of localized 3d from strontium rich regions of collective 3d electrons. This was justified by the discontinuity in the ferromagnetic Curie Temperature T_c in the same compositional range. These two different regions occur within the same rhomhohedral perovskite crystal. Thus the system represents two different electronic phases within the same crystallographic phase.

1.8.2 Electrical properties

The advent of transition metal oxides has made the electronic structure of first row of transition metal oxides an important subject for both theoretical and experimental research [12, 13, 140]. The various competing energies which affect the electronic behavior of these compounds are generally of similar order which gives them complex and diverse behavior. The ABO_3 perovskites of this group is a typical example where there is immense variation in electrical properties across the series. For example in the series of Lanthanum oxides of the form $LaMO_3$ the compounds varies from being semiconductor/metallic (M = Ti), through antiferromagnetic insulator (M = Cr, Mn, Fe) to a Pauli paramagnetic metal (M = Ni) [138, 139, 141-143].

The family of $La_{1-x}Sr_xCoO_3$ has been extensively studied for their interesting properties related to semiconductor-metal transition as a function of both temperature (for x = 0) and doping concentration. The parent compound in the series $LaCoO_3$ is a non magnetic p-type semiconductor at room temperature [132, 144]. The energy difference between the high spin and low spin state of the trivalent Co in $LaCoO_3$ is only 0.03 eV. Therefore a spin state transition takes place in the compound around 100 K with the lowering of resistivity [94, 138, 145]. The ratio of the high spin to low spin Co reaches 50:50 around $100 \leq T \leq 350$ K and above 600 K, the compound shows metallic behavior [130, 131, 133, 138, 146]. The conductivity of the $LaCoO_3$ is found to change remarkably with Sr^{2+} doping. The conductivity of the compound increases with increase of Sr^{2+} content and the conductivity reaches a maximum at Sr^{2+} content x = 0.5. With further increase in Sr^{2+} content the conductivity decreases [35, 93; 130, 132, 146]. The mechanism can be explained using the Kroger-Vink notation as follows. When $LaCoO_3$ is doped with Sr, the replacement of La^{3+} by Sr^{2+} leads to a charge state transition of Co^{3+} to Co^{4+} through the following reaction,

$$SrO + \frac{1}{4}O_2 + \left(La_{La^{3+}}^{3+}\right)^x + (Co_{Co^{3+}}^{3+})^x = \left(Sr_{La^{3+}}^{2+}\right)' + \left(Co_{Co^{3+}}^{4+}\right)^{\bullet} + \frac{1}{2}La_2O_3 \quad (1.4)$$
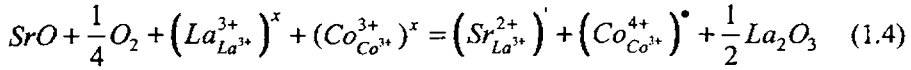
where $(Co_{Co^{3+}}^{4+})$ represents a hole responsible for the electrical conductivity in $La_{1-x}Sr_xCoO_3$. It carries a positive charge so that $La_{1-x}Sr_xCoO_3$ is a p-type conductor. The number of $(Co_{Co^{3+}}^{4+})$ increases with increase of Sr doping and reaches the maximum at La/Sr = 1. With the increase of Sr^{2+} beyond x = 0.5, the charge compensation is achieved through the creation of oxygen vacancy. The corresponding reaction can be written as

$$2(Co_{Co^{3+}}^{4+}) + (O_{O^{2-}}^{2-})^x = \frac{1}{2}O_2 + 2(Co_{Co^{3+}}^{3+})^x + (V_{O^{2-}}) \qquad (1.5)$$
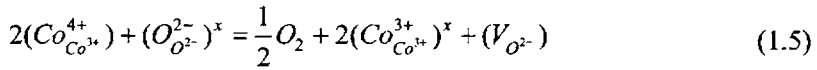
with $(V_{O^{2-}})$ representing one oxygen vacancy. Thus one oxygen vacancy balances two holes. Therefore formation of one oxygen vacancy consumes two holes and then drastically reduces the electrical conductivity [35, 93, 130, 133]. This explains the reduction in conductivity for the samples with Sr^{2+} content x > 0.5. A detailed explanation on the resistivity of the compound using the spin state of the Co ions will be considered while discussing the magnetoresistance (MR) of cobaltites.

1.8. 3. Magnetoresistance

Magnetoresistance is defined as the relative change in the electrical resistivity of a material upon the application of a magnetic field and is generally given by

$$\%MR = 100 \times \left\{ \frac{(\rho(H) - \rho(0))}{\rho(0)} \right\}, \qquad (1.6)$$

where $\rho^{(H)}$ and $\rho^{(0)}$ are the resistivities at a given temperature in the presence and in the absence of a magnetic field, respectively. MR is positive for most non magnetic metals, and its magnitude is limited to a few percent, whereas MR can be negative in magnetic materials because the magnetic field tends to reduce the spin disorder. MR property of the material can be used in magnetic storage of information, which explains the technological interest of the phenomena. IBM is using the Permalloy (composition: 80% Ni and 20% Fe) MR of about 3% in a small magnetic field at room temperature for magnetic storage of information. Thin films of magnetic superlattice have recently shown large magnetoresistance known as giant MR (GMR). In this case the application of small magnetic field align the magnetizations ferromagnetically and induce a resistivity decrease [147-149].

Among the perovskite oxides the MR phenomena was first observed in manganese perovskites of the form $A_{1-x}A'_{x}MnO_3$ where A is a rare earth and A' is a divalent cation [150]. These compounds have been subjected to extensive investigations due to their technological applications and due to the basic interest in solid state physics [151-153]. Unlike manganates the MR property of the cobalt based perovskites (cobaltites) are not extensively investigated. Eventhough the substitution for the rare earth ion A renders ferromagnetism and metallicity in the two systems, there are some basic differences between the two systems [139, 154-156]. In the following section the MR behavior of the manganates will be first discussed followed by the discussion on MR of cobaltites.

(a) MR in perovskite manganates

The discovery of ferromagnetism in mixed crystals $LaMnO_3$-$CaMnO_3$, $LaMnO_3$-$SrMnO_3$, and $LaMnO_3$-$BaMnO_3$ by Jonker and Van Santen triggered the research towards manganites [157]. The general formula for perovskite manganese oxide is $T_{1-x}D_xMnO_3$ where T is a trivalent rare earth ion or Bi^{3+}

38

cation and D a divalent alkaline earth metal or Pb^{2+} cation. The oxygen in the compound is usually in O^{2-} state and the relative fraction of Mn^{4+} and Mn^{3+} is regulated by "x"[153]. One of the earliest theories to explain the behavior of manganites is the Double exchange theory [158, 159]. This theory could explain most of the observed phenomena manganites and hence the study in this field was almost stagnant for a certain period. But the discovery of large MR effects in $Nd_{0.5}Pb_{0.5}MnO_3$ and $La_{2/3}Ba_{1/3}MnO_x$ in 1990s renewed the interest in manganites [150,160]. The thin films could yield MR as high as 60% which opens potential application in magnetic recording. The discovery of colossal magnetoresistance (CMR) produced an explosion of interest in the field of manganites. In $La_{0.67}Ca_{0.33}MnO_x$ thin films a MR three orders of magnitude larger than the typical giant MR of superlattice films was observed. The effect was called colossal to distinguish it from the previously found giant MR effect [161, 162]. In this section the MR behavior of perovskite manganites will be considered. The phase diagram of $La_{1-x}Sr_xMnO_3$ (LSMO) will be discussed and the general theories which are used to describe the behavior in the manganite system will be discussed.

The study of LSMO has been given considerable emphasis as it is a representative of the "large" bandwidth subset of manganese oxides [153]. The different phases of the compound with varying hole doping can be explained using the phase diagram of the compound shown in figure 1.6 [163-166]. At Sr^{2+} concentration $x = 0.4$, the system is metallic even above ferromagnetic (FM) transition temperature or Curie temperature, T_c. At Sr^{2+} densities above $x = 0.5$, an antiferromagnetic metallic (AFM) state is stabilized with ferromagnetism in planes and antiferromagnetism between those planes. For Sr^{2+} concentration slightly below $x = 0.3$, the state above T_c becomes an insulator, which transforms into metal upon reducing the temperature. At $x \leq 0.17$, an insulating phase is found even at low temperature. For $x \sim 0.12$ the region is a ferromagnetic insulator [164-166]. The MR behavior in LSMO can be explained as follows. Large negative MR was observed for all composition near the critical

39

temperature T_C for the ferromagnetic phase transition. Maximum MR is obtained for density region separating the insulating state from metallic states at low temperature, viz. $x = 0.175$ [165, 166]. This can be interpreted as a field induced nonmetal-metal transition as the temperature dependence of resistivity also shows a change of sign close to T_C. The large T_c (~250K) makes this region attractive for potential applications. The MR behavior could be correlated with the changes in the magnetization of the compound and was found to closely related to its composition and conductivity [165]. The various theories explaining the behavior of manganites can be explained as follows.

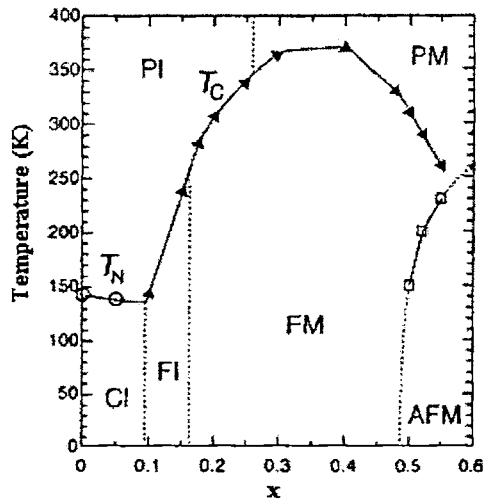**Figure 1.6.** Phase diagram of $La_{1-x}Sr_xMnO_3$. The antiferromagnetic phase (AFM) at large x denotes anti ferromagnetic metal with uniform orbital order. PM, PI, FM, FI and CI denote paramagnetic metal, paramagnetic insulator, ferromagnetic metal, ferromagnetic insulator and spin-canted insulator states respectively. T_c is the Curie temperature and T_N is the Neel temperature (from [163])

(i) Double exchange

Double exchange theory (DE) is one of the early theoretical works on the manganites which focused on the qualitative aspects of the experimentally discovered relation between transport and magnetic properties. According to the theory proposed by Zener, the states of the manganites are assumed to be uniform and charges move in manganites by the generation of a spin polarized state [158]. The DE process has been historically explained in two different ways. Zener considered the explicit movement of electrons schematically written as

$$Mn_{1\uparrow}^{3+}O_{2\uparrow,3\downarrow}Mn^{4+} \rightarrow Mn^{4+}O_{1\uparrow,3\downarrow}Mn_{2\uparrow}^{3+} \tag{1.7}$$
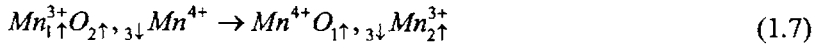
where 1, 2, and 3 label electrons that belong either to the oxygen between the manganese, or to the e_g -level of the Mn-ions. Here there are two simultaneous motions involving electron 2 moving from the oxygen to the right Mn-ion, and electron 1 from the left Mn-ion to the oxygen. The second theory was proposed by Anderson and Hasegawa which involves a second order process in which the two states described above go from one to the other using an intermediate state $Mn_{1\uparrow}^{3+}O_{3\downarrow}Mn_{2\uparrow}^{3+}$ [159]. In this case the effective hopping for the electron to move from one Mn-site to the next is proportional to the square of the hopping involving the p-oxygen and d-manganese orbitals. In addition if the localized spins are considered classical and with an angle θ between the nearest neighbor ones, the effective hopping becomes proportional to $\cos(\theta/2)$. The $\theta = 0$ the hopping is largest, while if $\theta = \pi$, corresponding to an antiferromagnetic background, then the hopping cancels.

(ii) Ferromagnetism due to large Hund coupling

The large Hunds coupling in the compound can also stabilize the ferromagnetic phase in manganates [167]. In this case, when the e_g electrons directly jump from Mn to Mn, their kinetic energy is minimized if all spins are aligned. This procedure to obtain ferromagnetism is also called double-exchange even though there is little resemblance in the physical process with the original DE ideas where two electrons are involved in actual hopping. The recently generated computer simulations and a variety of mean-field approximations suggest that the main reason for ferromagnetism is indeed a large Hunds coupling.

(iii) Charge ordered state at x = 0.5

According to the charge ordering model proposed by J.B.Goodenough [168] an electronic phase separation occurs in half doped $Ln_{0.5}A_{0.5}MnO_3$ manganites. In this case the e_g carriers; $e_g^0 - e_g^1$ are delocalized in the paramagnetic state but localized in alternating Mn^{4+} and Mn^{3+} planes below the characteristic charge-ordering temperature, T_{CO} [169]. This phenomenon is driven by long-range coulombic repulsion which tends to separate the Mn^{3+} and Mn^{4+} species. The Jahn-Teller distortion of the Mn^{3+} plays a crucial role in the charge ordering process because the d_{z^2} orbital of Mn^{3+} are arranged in $90°$ zigzag chains in the charge ordered phase. The radius of the A cation $\langle r_A \rangle$ is a crucial parameter governing T_{CO} and T_{CO} increases as $\langle r_A \rangle$ decreases. Therefore as the Mn-O-Mn angle decreases, the charge ordering is favored at the expense of the ferromagnetic metallic state. The spin order of all the charge ordered $Ln_{0.5}Ca_{0.5}MnO_3$ is antiferromagnetic state below the Neel temperature T_N and the value of T_N is always such that $T_N \leq T_{CO}$. Therefore the charge ordering process in $Ln_{0.5}Ca_{0.5}MnO_3$ half-doped manganites induces a structural transition and an antiferromagnetic arrangement of spins [149, 170].

(iv) Recent theories

The above mentioned theories could not explain all the properties of perovskite manganites, especially the colossal magnetoresistance. The MR phenomena in manganites were believed to be the magnetic field induced insulator metal transition as the ferromagnetic transition and the metal insulator transition is simultaneous [165]. The experimental results on manganites made it clear that the double exchange interaction, which is the basic interaction correlating resistivity and magnetism is not sufficient to explain the MR phenomena [171]. The MR phenomena can be related to the formation of small lattice polarons in the paramagnetic state. The large MR resulting from the transition is called the colossal magnetoresistance (CMR) [161]. Another explanation towards the understanding of CMR can be given by electron-phonon coupling. The electron-phonon coupling is originated from the large Jahn-Teller effect which occurs for d^4 ions in an octahedral ligand environment [172-174]. The most recent theory which is capable of explaining almost all the observed phenomena in manganites is the theory of phase separation. The phase separation can be both structural and electronic [153, 175, 176]. According to this model the ferromagnetic grains are embedded in antiferromagnetic matrix. The ferromagnetic phase is metallic with low resistivity where as the antiferromagnetic phase is insulating with high resistivity. With the application of magnetic field aniferromagnetic phase can be converted into ferromagnetic phase causing large magnetoresistance. This phenomenon is more evident near the percolation limit where the application of the magnetic field leads to colossal magnetoresistance as the ferromagnetic clusters form a percolative path [176].

(b) MR in perovskite cobaltite
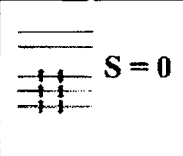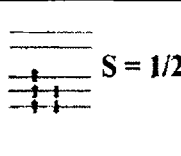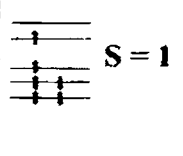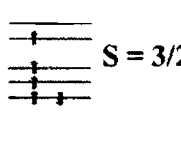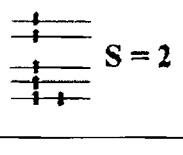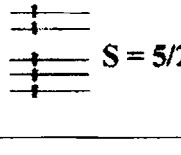
Perovskite cobaltites have received relatively little attention compared to manganites even though both of them were discovered during the same period of time. The Sr^{2+} substitution for La^{3+} brings the same changes in the transport

properties of both the systems. However, there are certain differences between the two [139, 154-156]. For example the parent compound in cobaltites $LaCoO_3$ is a diamagnetic semiconductor at T = 0, unlike $LaMnO_3$ which exhibit antiferromagnetic ordering with $T_N \approx 150$ K. Also cobalt perovskites does not exhibit CMR unlike manganites despite having high metallic conductivity [164, 177]. This difference is due to the fundamental difference in the strength of the spin to charge and lattice coupling in the two systems [175].

The unique properties of the cobaltites which differentiate them from the Mn systems are the existence of spin state transitions and the presence of magnetic ground state [145, 178-182]. The thermally activated spin state transition of the cobaltite system can be understood by considering the spin states of trivalent and tetravalent Co ions in the compound. The comparable crystal field splitting energy and the Hund's rule exchange energy contributes to the spin state transitions in the t_{2g} and e_g states of the Co ion in the $La_{1-x}Sr_xCoO_3$ system [138, 149, 183]. In $LaCoO_3$, the Co ion is in the low-spin-state (LS) Co^{III} (t_{2g}^6, S = 0) at low temperature. The energy difference between the LS and high spin (HS); Co^{3+} ($t_{2g}^4 e_g^2$, S = 2) is only 0.03 eV [94, 138, 145, 184]. The large crystal field stabilizes the low spin state at low temperature. Thermal excitation can provide a spin transition from the LS to the intermediate spin; (IS: $t_{2g}^5 e_g^1$) at a temperature of 100 K [145, 184]. Metal-Insulator transition is observed in the $LaCoO_3$ system with the spin state transition to high spin state above 500 K. Sr^{2+} substitution creates tetravalent Co ions which can take either of LS: Co^{IV} (t_{2g}^5, S = ½), IS Co^{+4} ($t_{2g}^4 e_g^1$, S = 3/2) and HS states Co^{+4} ($t_{2g}^3 e_g^2$, S = 5/2). The HS Co^{4+} is 1 eV lower in energy than LS Co^{IV}. Thus $La_{1-x}Sr_xCoO_3$ system contains a mixture of LS Co^{III} (t_{2g}^6), LS Co^{IV} (t_{2g}^5), IS Co^{3+} ($t_{2g}^5 e_g^1$), IS Co^{+4} ($t_{2g}^4 e_g^1$) and some HS Co^{3+} ($t_{2g}^4 e_g^2$) and HS Co^{4+}($t_{2g}^3 e_g^2$) depending on the temperature and the Sr^{2+} content . The possible spin states of the Co^{3+} and Co^{4+} ions in the compound is given in table 1.1. But in manganite systems the Hunds rule

exchange energy is larger than the crystal field splitting energy and the HS state is stable in the Mn based systems [144, 175]. The strong Hunds rule coupling prevents thermal variation of the spin state.

Table 1.1 The possible spin states of Co^{3+} and Co^{4+} in $La_{1-x}Sr_xCoO_3$. The lower energy levels corresponds to t_{2g} electrons while the highest one corresponds to e_g states (from [156])

Spin-state	Co^{3+}	Co^{4+}
LS (low spin)	$S = 0$	$S = 1/2$
IS (intermediate spin)	$S = 1$	$S = 3/2$
HS (high spin)	$S = 2$	$S = 5/2$

One of the earliest evidence for the spin state transition of the compound was given by Chainani et al. [142] from the electron spectroscopy studies. The ground state of the tetravalent Co ions was found to be the HS state located below the LS and IS state. Further evidence was given by the NMR measurements and neutron diffraction study [145, 187].The spin state of the trivalent Co ion in the LS state for low doping was converted to trivalent HS or tetravalent HS with increasing Sr^{2+} content. Recent theoretical works on the $LaCoO_3$ system favor IS state for the Co^{3+} ion in the compound [186, 187]. But

45

there are conflicting reports on the spin state of the Co ions in $La_{1-x}Sr_xCoO_3$. The trivalent Co ion can be considered to be in IS state. But even with very small Sr^{2+} doping, the LS state of the tetravalent cobalt ion is suppressed. Therefore the spin state of tetravalent Co ion is an open issue. Magnetometry measurements and neutron scattering measurements suggests an IS state for the tetravalent Co ion in the composition range $0.2 < x < 0.7$ [145, 156,186]. But the recent investigations suggests that since the energy difference between the HS and the IS state is far larger than that between the IS and LS state, no spin state transition is observed for the compound in the temperature interval $5 < T < 800$ K, for compositions in the range $0.2 < x < 0.7$. Therefore the trivalent and tetravalent Co ion in the compound can be considered to in IS state and a thermal excitation to the HS state is less probable [156].

The existence of a spin glass state with short range ferromagnetic ordering for low Sr^{2+} doping can be considered as the magnetic ground state for low doping in cobaltites. The Sr^{2+} doping introduces holes in the system which stabilizes IS state for the neighboring trivalent Co ion. There is an inhomogeneous distribution of the Sr^{2+} ions in the system and the material segregates into hole rich metallic FM region and hole poor semiconducting matrix [156]. Neutron diffraction, high resolution electron microscopy and magnetic sucesptability measurements have shown long range FM order in the compound even for $x = 0.1$ and a transition to spin glass (SG) is observed for $x = 0.1$ [143, 145]. The NMR measurements also revealed the existence of SG state for low Sr^{2+} doping and cluster glass (CG) phase for high Sr^{2+} content [180]. The boundary between the two to occur at the critical composition, $x_c = 0.18$. But the recent investigation shows that the boundary between the spin glass phase and the ferromagnetic metallic phase is not sharp [156]. The higher doping level samples shows the signature of glassy behavior such as frequency-dependent ac susceptibility peaks and time dependent phenomena Brillouin-like temperature dependence of magnetization and apparent Curie temperature. Similarly the low doping samples exhibit characteristic of both spin glass behavior and strong

ferromagnetic correlations. Therefore there exists a coexistence of ferromagnetic ordering and glassy behavior in the system.
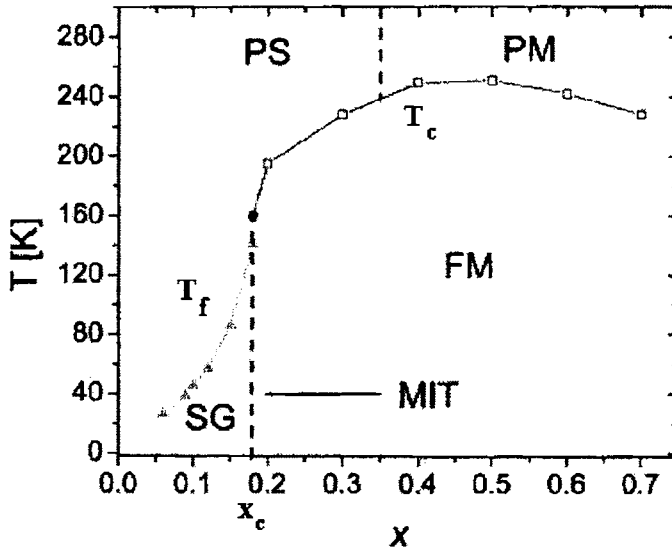
Figure 1.7 Magnetic phase diagram of $La_{1-x}Sr_xCoO_3$ $0 \leq x \leq 0.5$.SG, PS, PM and FM represent spin glass, paramagnetic semiconductor and ferromagnetic phase respectively. MIT is the metal insulator transition and T_c and T_f are the ferromagnetic transition temperature and spin-glass transition temperature respectively (from [156])

The spin state transition and the magnetic ground state explain the observed phase diagram of the compound (figure 1.7). The phase diagram also explains the MR and the zero field resistivity behavior of the $La_{1-x}Sr_xCoO_3$. The phase diagram is dominated by two distinct regions characterized by the critical doping concentration x_c ($0.15 \leq x_c \leq 0.18$). The regime $x > x_c$ is characterized by short range ferromagnetic ordering and for $x < x_c$, the magnetism is dominated by spin glass type behavior. In the regime $x > x_c$, the onset of ferromagnetic transition is denoted by the transition temperature T_c, below which the material is ferromagnetic and above T_c the material is paramagnetic. The T_c is found to

47

monotonically decrease with decreasing x from x = 0.5 down to x = 0.18. Below x = 0.18, the phase diagram is dominated by spin glass transition temperature T_f, which decreases with decreasing x. The critical point x_c marks the point where ferromagnetic clusters coalesce and a finite T_c of each sample is an evidence for percolating ferromagnetic clusters. For low values of x, the system is originally dominated by AF interactions and the material behaves as a semiconductor. As x is increased, the fraction of the Co^{4+} ions increases and the system phase separates into ferromagnetically interacting hole-rich clusters in antiferromagnetically correlated matrix. Thus for Sr^{2+} content more than the critical composition, the compound is a metallic ferromagnet in the temperature range below the transition temperature and above which it is paramagnetic. The resistivity of the compound decreases with increasing Sr^{2+} content and the minimum resistivity is observed for the composition x = 0.5, where the fraction of the Co^{4+} ions reaches the maximum. With further Sr^{2+} doping there is slight decrease in resistivity due to the reduction in the Co^{4+} content [35, 93, 130, 133]. The temperature of spin-glass freezing ie the temperature, at which F and AF clusters compete, increases with increasing x. Hence the $T_f(x)$ increases monotonically with x and eventually join with the $T_c(x)$ line at the point (x_c) at which the cluster coalesce. The SG phase is achieved due to the frustration between AF super exchange and ferromagnetic double exchange. The magnetic behavior for the system for very low doping concentration (x < 0.01) suggests magnetic polaron formation which could be the precursors of ferromagnetically correlated clusters that dominate the behavior at larger x. Therefore the $La_{1-x}Sr_xCoO_3$ exhibits a SG dominated phase for x < 0.18 and a F dominated phase for x > 0.18, even though the ground state in both cases are not entirely pure [156].

The MR in the $La_{1-x}Sr_xCoO_3$ compound shows different behavior for the semiconducting and metallic compositions. The metallic composition of the compound shows small negative MR like a typical ferromagnetic metal and the semiconducting compositions shows large negative MR close to 0 K. In metallic

compositions the maximum in MR is found close to the T_c of the samples but in semiconducting compositions the peak in MR close to T_c disappears. There is qualitative difference in the MR behavior shown by both systems.

(i) Metallic Compositions

The value of MR for the metallic compositions is found to increase with increase of Sr^{2+} content. The maximum MR is usually obtained for the most metallic composition (x = 0.5) and with further increase in Sr^{2+} content, there is a slight decrease in MR. The observed MR behavior in the metallic composition can be explained using the Double exchange theory. In the Double exchange theory, the electron or the hole transfer between the neighboring sites depends on the relative angle $\Delta\theta_{ij}$ of the local t_{2g} spins, i.e.

$$t_{ij} = t_0 \cos\left(\Delta\theta_{ij}\Big/2\right)$$

(1.8)

In the ferromagnetic state the spins are aligned parallel and spin transfer integral t_{ij} reaches its maximum value [177]. Therefore the carrier mobility increases and the resistivity is reduced. The peak in the negative MR is observed around the T_c of the samples. The external magnetic field aligns the local spin moments of the sample. Maximum magnetization due to the alignment of the spin moments is obtained at the critical temperature of the ferromagnetic material [156, 177]. Therefore there is reduced carrier scattering round the T_c with magnetic field which causes maximum negative MR around T_c. The AC magnetic susceptibility studies of the system give evidence of long range FM ordering for Sr^{2+} content x > 0.3 [155]. Senaris Rodriguez et al. [146] observed that the interpenetrating hole poor matrix persists in the compound even up to x = 0.5 although the composition in the range $0.3 \leq x \leq 0.5$ shows metallic FM behavior. But Mahendiran et al. [154] observed a decrease in negative MR as the sample become metallic and the most metallic composition showed a positive

contribution at a temperature $T > T_c$ due to some orbital effects in the metal. The MR of the compound was found to enhance with oxygen deficiency as the applied magnetic field suppresses the quantum interference effects created with oxygen deficiency [188].

(ii) Semiconducting compositions

In $La_{1-x}Sr_xCoO_3$ as the Sr^{2+} doping is lowered, the compound exhibits semiconducting behavior. In this case as the doping x is reduced below the critical concentration $x_c = 0.18$, the peak in the MR close to T_c disappears and the MR becomes much pronounced at low temperature. The low temperature MR value in these compositions can give large value of MR up to 35 % [156]. This effect is more prominent for the most resistive samples with no ferromagnetic order. The MR in these compositions also shows hysteric effect. The onset of metallicity and ferromagnetism is simultaneous in $La_{1-x}Sr_xCoO_3$ [189]. The double exchange theory cannot be used to explain the large negative MR behavior in the semiconducting samples at low temperature. Because according to this theory the MR can be observed only during a transition to the FM state [190, 191].

The applied magnetic field facilitates ferromagnetic cluster formation at low temperature as the temperature is low compared to the energy involved in FM exchange interaction causing large negative MR close to the critical composition, x_c [154]. The MR in this case shows peak corresponding to the spin glass-like transition temperature T_g. Wu et al. [156] also observed a similar low temperature large negative MR for the compound in the semiconducting composition. The observed high value of n-MR observed at low temperature was found to decrease rapidly at the MIT (meta-insulator transition). Because beyond MIT, isolated FM clusters cease to exist as they coalesce into a percolative network. The observed features in the MR behavior of the semiconducting composition can be explained using the theory of phase separation [153, 163,

50

192]. $La_{1-x}Sr_xCoO_3$ can be considered to be spontaneously phase separated into metallic clusters embedded in a semiconducting matrix of hole-poor non FM material. The ferromagnetic phase is metallic with low resistivity where as the antiferromagnetic phase is insulating with high resistivity. With the application of magnetic field aniferromagnetic phase can be converted into ferromagnetic phase causing large magnetoresistance. This phenomenon is more evident near the percolation limit where the application of the magnetic field leads to colossal magnetoresistance as the ferromagnetic clusters form a percolative path [143].

References

1. J.F.Scott, C.A.Paz De Araujo, Science. **246**(1989)1400
2. A.Sheikholeslami, P.G.Gulak, Proc.IEEE. **88**(2000)667
3. D.Hadnagy, The Industrial Physicist. **5**(1999)26
4. R. Bruchhaus, B-K. Moon, A. Hilliger, N. Nagel, Y. Yamada, H. Itokawa, K. Yamakawa, I. Kunishima, G. Beitel, Integrated Ferroelectrics. **64**(2004)115
5. N.Setter, D.Damjanovic, L.Eng, G.Fox, S.Gevorgian, S.Hong, A.Kingon, H.Kohlstedt, N.Y.Park, G.B.Stephenson, I.Stolichnov, A.K.Taganstev, D.V.taylor, T.Yamada, S.Streiffer, J.Appl.Phys. **100**(2006)051606
6. R. E. Jones Jr., Proc. IEEE Custom Integrated Circuits Conf., (1998) pp. 431
7. T. Miwa, J. Yamada, Y. Okamoto, H. Koike, H. Toyoshima, H. Hada, Y. Hayashi, H. Okizaki, Y. Miyasaka, T. Kunio, H. Miyamoto, H.Gomi, and H. Kitajima, Proc. IEEE Custom Integrated Circuits Conf., (1998) pp. 439
8. S.Baik, N.Setter, O.Auciello, J.Appl.Phys. **100**(2006)051501
9. D.J. Wouters, G.J. Norga, F. Beckers, L. Bogaerts, H.E. Maes, 9th Int. Symp. on Integr. Ferroelectrics., (1997) pp. 19
10. H.Koike, T.Otsuki, T.Kimura, M.Fukuma,Y.Hayashi, Y.Maejima, K.Amanuma, N.Tanabe, T.Matsuki, S.Saito,T.Takeuchi, S.Kobayashi, T.Kunio, T.Hase, Y.Miyasaka, N.Shohata,M.Takada, Proc. of IEEE Int. Solid-State Circuits Conf., (1996) pp. 368
11. A.J.Dekker, *Introduction to Solid State Physics*, Macmillan India Limited, New Delhi. 1981, pp.184
12. M. E. Lines and A. M. Glass, *Principles and Applications of Ferroelectrics and Related Materials*, Oxford University Press, New York. 1977, pp.8
13. Z.L.Wang, *Smart Perovskites*, in *Encyclopedia of SMART Materials*,

Volume 1 and Volume 2, edited by M.Schwartz, John Wiely and Sons Inc., New York. 2002, pp. 994

14. H.Ishiwara, FED Jrnl. **11**(2000)27

15. H . Takasu , Microelectronic Engineering **59**(2001)237

16. T. Nakamura, Y. Nakao, A. Kamisawa, H. Takasu, IEEE Int. Solid-State Circuit Conf., (1995) pp. 68

17. Y. Fujimori, N. Izumi, T. Nakamura, A. Kamisawa, Integrated Ferroelectrics. **21**(1998)73

18. N.W.Schubring, R.A.Dork, J.P.Nolte, J.Appl.Phys. **38**(1967)1671

19. B.Wyncke, F.Brehat, Physica Status Solidi (a). **104**(1987)873

20. S.S.Eaton, D.B.Butler, M.Parris, D.Wilson, H.McNeillie, Proc. IEEE Int. Solid-State Circuit Conf., (1988) pp. 130

21. X.Chen, H.Fan, and S.Ke, Appl.Phys.Lett. **88**(2006)012901

22. W.L.Warren, D.Dimos, G.E.Pike, B.A.Tuttle, M.V.Raymond, R.Ramesh, J.T.Evans.Jr, Appl.Phys,Lett. **67**(1995)866

23. H.N.Al-Shareef, B.A.Tuttle, W.L.Warren, D.Dimos, M.V.Raymond, M.A.Rodriguez, Appl.Phys.Lett. **68**(1996)272

24. C-J.Peng, S.B.Krupanidhi, J.Mater.Res. **10**(1995)708

25. F.M.Pontes, E.Longo, E.R.Leite, J.A.Varela, Thin Solid Films. **386**(2001)91

26. W.J.Kim, W.Chang, S.B.Qadri, J.M.Pond, S.W.Kirchofer, D.B.Chrisey, J.S.Horwitz, Appl.Phys.Lett. **76**(2000)1185

27. Y.I.Kim, D.S.Shin, Appl.Phys.Lett. **71**(1997)2507

28. M.Sayer, Z,Wu, C.V.R.Vasant Kumar, D.T.Amm, E.M.Griswold, Can.J.Phys. **70**(1992)1159

29. M.Dawber, K.W.Rabe, J.F.Scott, Rev.Mod.Phys. **77**(2005)1083

30. S.Aggarwal, T.K.Song, A.M.Dhote, A.S.Prakash, R.Ramesh, N.Velasquez, L.Boyer, J.T.Evans.Jr, J.Appl.Phys. **83**(1998)1617

31. C.B.Eom, R.B.Van Dover, J.M.Philips, D.J.Werder, J.H.Marshall, C.H.Chen, R.J.Cava, R.M.Fleming, D.K.Fork, Appl.Phys.Lett. **63**(1993)2570

32. H.Han, J.Zhong, S.Kotru, P.Padmini, X.Y.Song, R.K.Pandey, Appl.Phys.Lett. **88**(2006)092902

33. M-S.Chen, T-B.Wu, J-M.Wu, Appl.Phys.Lett. **68**(1996)1430

34. B.Nagaraj, S.Aggarwal, R.Ramesh, J.Appl.Phys. **90**(2001)375

35. S.Madhukar, S.Aggarwal, A.M.Dhote, R.Ramesh, A.Krishnan, D.Keeble, E.Poindexter, J.Appl.Phys. **81**(1997)3543

36. Z.Wu, M.Sayer, Proc. of the Eigth IEEE International Symposium on Applications of Ferroelectrics. (1992) pp. 244

37. R.Ramesh, H.Gilchrist, T.Sands,, V.G.Keramidas, R.Haakenaasen, D.K.Fork, Appl.Phys.Lett. **63**(1993)3592

38. R.Ramesh, J.Lee, T.Sands, V.G.Keramidas, O.Auciello, Appl.Phys.Lett. **64**(1994)2511

39. E.M.Alkoy, S.Alkoy, K.Uchiyama, T.Shiosaki, Jpn.J.Appl.Phys. **45**(2006)5110

40. G.Han, J.Lee, Surface and Coatings Technology. **131**(2000) 543

41. Y.Furusawa, H.DOI, Jpn.J.Appl.Phys. **38**(1999)6864

42. S.Aggarwal. A.M.Dhote, R.Ramesh, W.L.Warren, G.E.Pike, D.Dimos, M.V.Raymond, B.A.Tuttle, J.T.Evans.Jr, Appl.Phys.Lett. **69**(1996)2540

43. G.E.Pike, W.L.Warren, D.Dimos, B.A.Tuttle, R.Ramesh, J.Lee, V.G.Keramidas, J.T.Evans.Jr. Appl.Phys.Lett. **64**(1995)484

44. J.Lee, R.Ramesh, V.G.Keramidas, W.L.Warren, G.E.Pike, J.T.Evans.Jr. Appl.Phys.Lett. **66**(1995)1337

45. B.H.Park, T.W.Noh, J.Lee, C.Y.Kim, W.Jo, Appl.Phys.Lett. **70**(1997)1101

46. W.L.Warren, H.N.Al.Shareef, D.Dimos, B.A.Tuttle, G.E.Pike, Appl.Phys.Lett. **68**(1996)1681

47. W.L.Warren, G.E.Pike, B.A.Tuttle, D.Dimos, Appl.Phys.Lett. **70**(1997)2010

48. J.T.Cheung, P.E.D.Morgan, D.H.Lowndes, X.Y.Zheng, J.Breer, Appl.Phys.Lett. **62**(1993)2045

49. P.W.Chan, W.Wu, K.H.Wong, K.Y.Tong, J.T.Cheung, J.Phys.D.Appl.Phys. **30**(1997)957

50. Y.Yang, K.F.Wang, C.Zhu, J-M.Liu, J.Appl.Phys. **99**(2006)044109

51. S.K.Pandey, A.R.James, C.Prakash, T.C.Goel, K.Zimik, Thin Solid Films. **513**(2006)95

52. T.Nakamura, Y.Nakao, A.Kamisawa, H.Takasu, Jpn.J.Appl.Phys. **33**(1994)5207

53. J.Bandaru, T.Sands, L.Tsakalakos, J.Appl.Phys. **84**(1998)1121

54. D.Barrow, C.V.R.Vasant Kumar, R.Pascual, M.Sayer, Proc.Mater.Res.Soc.Symp. **243**(1992)113

55. A.V.Rao, S.A.Mansour, A.L.Bemet.Jr, Mater.Lett. **29**(1996)255

56. C-C.Yang, M-S.Chen, T-J Hong, C-M.Wu, J-M.Wu, T-B.Wu, Appl.Phys.Lett. **66**(1995)2643

57. B.A.Tuttle, H.N.Al-Shareef, W.L.Warren, M.V.Raymond, T.J.Headley, J.A.Voigt, J.Evans, R.Ramesh, Microelectronics.Engg. **29**(1995)223

58. M.Suzuki, T.Ami, Mater.Sci.Engg.B. **41**(1996)16

59. H.Yu, M.Li, C.Hui, A.Xu, W.Shao, Thin Solid Films **493**(2005)20

60. W-J.Lee, Y-M.Kim, H-G.Kim, Thin Solid Films. **269**(1995)75

61. K.B.Lee, S.Tirumala, S.B.Desu, Appl.Phys.Lett. **74**(1999)1484

62. N.Inoue, Y.Hayashi, J.Electro.Chem.Soci. **152**(2004)G113

63. H.Maiwa, N.Ichinose, K.Okazaki, Jpn.J.Appl.Phys. **33**(1994)5223

64. K.Sreenivas, M.Sayer, T.Laursen, J.L.Whitton, R.Pascual, D.J.Jhonson, D.T.Amm, G.I.Spourle, D.F.Mitchell, M.J.Graham, S.C.Gujrathi, K.Oxorn, Mater.Res.Soc.Symp.Proc. **200**(1990)255

65. L.D.Madsen, L.Weaver, J.Elect.Mater. **21**(1992)93

66. J. Lee, L. Johnson, A. Safari,R. Ramesh, T. Sands, H. Gilchrist, V. G. Keramidas, Appl.Phys.Lett. **63**(1993)27

67. R.Ramesh, A.Inam, W.K.Chan, B.Wilkens, K.Myers, K.Remsching, D.L.Hart, J.M.Tarascon, Science. **252**(1991)944

68. R.Ramesh, W.K.Chan, B.Wilkens, H.Gilchrist, T.Sands, J.M.Tarascon, V.G.Keramidas, D.K.Fork, J.Lee, A.Safari, Appl.Phys.Lett.

61(1992)1537

69. R. Ramesh, T. Sands, V. G. Keramidas, Appl. Phys. Lett. **63**(1993)731

70. S-M.Yoon, E.Tokumitsu, H.Ishiwara. Appl.Surf.Sci. **117/118**(1997)447

71. F.Chen, H.F.Wang, Q.Z.Liu, W.Wu, X-G.Li, Appl.Phys.Lett. **90**(2007)082904

72. Y-F.Chen, L.Sun, T.Yu, J-X Chen, Y-Y Zhu, N-B.Ming, X-Y.Chen, Z-G Liu, Thin Solid Films **269**(1995)18

73. S.Aggarwal, S.R.Persusse, B.Nagaraj, R.Ramesh, Appl.Phys.Lett. **74**(1999)3023

74. C.Rossel, A.Rosova, K.Hasekova, D.Machajdik, K.Frohlich, J.Appl.Phys. **100**(2006)04451

75. H.D. Bhatt, R.Vedula, S B. Desu, G C. Fralick, Thin Solid Films **350** (1999)249

76. A.Laha, S.Saha, S.B.Krupanidhi, Thin.Solid Films **424**(2003)274

77. J.Yin, T.Zhu, Z.G.Liu, T.Yu, Appl.Phys.Lett. **75**(1999)3698

78. I-D.Kim, H-G.Kim, Jpn.J.Appl.Phys. **40**(2001)2357

79. W.Bensch, H.W.Schmalle, A.Reller, Solid State Ionics, **43**(1990)171

80. C.B.Eom, R.J.Cava, R.M.Fleming, J.M.Phillips, B.B.Van.Dover, J.H.Marshall, J.W.P.Hsu, J.J.Krajewski, W.F.Peck. Jr, Science. **258**(1993)1776

81. L.Che, J.Cheng, S.Yu, Z.Meng, Mater.Lett. **61**(2007)3068

82. C.B.Eom, J.Z.Sun, K.Yamamoto, A.F.Marshall, K.E.Luther, T. H.Geballe, Appl.Phys.Lett. **55**(1989)595

83. J-E.Heo, B-J.Bae, D-C.Yoo, S-D.Nam, J-E.Lim, D-H Im, S-H Joo, Y-J Jung, S-H Choi, S-O Park, H-S Kim, U-In Chung, J-T.Moon, Jpn.J.Appl.Phys. **45**(2006)3198

84. M.Izuha, K.Abe, M.Koiki, S.Takeno, N.Fukushima, Appl.Phys.Lett. **70**(1997)1405

85. J.H.Cho, K.C.Park, Appl.Phys.Lett. **75**(1999)549

86. C. C. Yang, M. S. Chen, T. J. Hong, C. M. Wu, J. M. Wu, T. B. Wu, Appl. Phys. Lett. **66**(1995)2643

56

87. A. Li, C. Ge, P. Lu, N. Ming, Appl. Phys. Lett. **68**(1996)1347

88. K.M. Satyalakshmi, R.M. Mallya, K.V. Ramanathan, X.D. Wu, B. Brainard, D.C. Gautier, M.S. Hegde, Appl. Phys. Lett. **62**(1993)233

89. K. V. R. Prasad, K. B. R. Varma, A. R. Rogu, K. M. Satyalakshnmi, R. M.Mallya, M. S. Hegde, Appl. Phys. Lett. **63**(1993)1898

90. J.Ma, X.J.Meng, J.L.Sun, T.Lin, F.W.Shi, J.H.Chu, Mater.Res.Bull. **40**(2005)221

91. W.Wu, K.H.Wong, C.L.Choy, J.Vacu.Sci.Tech.A. **18**(2000)79

92. J. Mizusaki, J. Tabuchi, T. Matsuura, S. Yamauchi, K. Fueki, J.Electrochem.Soc. **136**(1989)2082

93. J-M.Liu, C.K.Ong, J. Appl. Phys. **84**(1998)5560

94. P.M.Raccah, J.B.Goodenough, J.Appl.Phys. **39**(1968)1209

95. J.Muzusaki, Y.Mima, S.Yamauchi, K.Fucki, J.Solid.State.Chem. **80**(1989)102

96. H-S.Kim, M-H.Lim, H-G.Kim, I-D.Kim, Electrochemical and Solid State Letters 7(2004)J1

97. R.Ramesh, B.Dutta, T.S.Ravi, J.Lee, T.Sands, V.G.Keramidas, Appl.Phys.Lett. **64**(1994)1588

98. A.M.Dhote, S.Madhukar, W.Wei, T.Venkatesan, R.Ramesh, C.M.Cotell Appl.Phys.Lett. **68**(1996)1350

99. Z.G.Liu, X.Y.Chen, J-M.Liu, Z.C.Wu, D.Feng, Solid.State.Comm. **91**(1994)671

100. G.S.Wang, X.J.Meng, J.L.Sun, Z.Q.Lai, J.Yu, S.L.Guo, J.G.Cheng, J.Tang, J.H.Chu, Appl.Phys.Lett. **79**(2001)3476

101. C-C.Chou, C-S.Hou, G-C.Cheng, H-F.Cheng, Appl.Surf.Sci. **142**(1999)413

102. J.Lee, C.H.Choi, B.H.Park, T.W.Noh, J.K.Lee, Appl.Phys.Lett. **72**(1998)3380

103. I-D.Kim, K-Y.Han, H-G.Kim, Electrochemical and Solid State Letters 7(2004)F11

104. Y.Wang, L.Zhou, X.B.Lu, Z.G.Liu, Appl.Surf.Sci. **205**(2003)176

57

105. B.T.Liu, K.Maki, S.Aggarwal, B.Nagaraj, V.Nagarajan, L.Salamanca-Riba, R.Ramesh, A.M.Dhote, O.Auciello, Appl.Phys.Lett. **80**(2002)3599

106. B.T.Liu, K.Maki, Y.So, V.Nagarajan, R.Ramesh, J.Lettieri, J.H.Haeni, D.G.Schlom, W.Tian, X.Q.Pan, F.J.Walker, R.A.Mckee, Appl.Phys.Lett. **80**(2002)4801

107. B.T.Liu, X.Zhang, W.T.Zhang, Z.Yan, C.S.Cheng, F.Li, L.Li, Q.X.Zhao, Mater.Lett. **61**(2007)3045

108. H.U.Anderson, Solid.State.Ionics **52**(1992)33

109. V.V.Kharton, E.N.Naumovich, A.A.Vecher, A.V.Nikolaev, J.Solid.State.Chem. **120**(1995)128

110. H.J.M.Bouwmeester, H.Kruidhof, A.J.Burggraaf, Solid State Ionics. **72**(1994)185

111. C.M.Chiu, Y.H.Chang, Sensors Actuators.B. **54**(1999)236

112. A.Bieberle – Hutter, M.Sogaard, H.L.Tuller, Solid.State.Ionics. **177**(2006)1969

113. O.Yamanato, Y.Takeda, R.Kanno, M.Noda, Solid.State.Ionics. **22**(1987)241

114. M.Sase, J.Suzuki, K.Yashiro, T.Otake, A.Kaimai, T.Kawada, J.Mizusaki, H.Yugami, Solid.State.Ionics. **177**(2006)1961

115. J.L.Routbort, R.Doshi, M.Krumpelt, Solid.State.Ionics. **90**(1996)21

116. Y.Huang, J.M.Vohs, R.J.Gorte, J.Electr.Chem.Soci. **153**(2006)A951

117. Y.Teraoka, H.M.Zhang, S.Furukawa N.Yamazoe, Chem. Lett. **14**(1985)1743

118. Y.Teraoka, T.Nobunaga N.Yamazoe, Chem. Lett. **17**(1988)503

119. Y.Teraoka, T.Nobunaga, K.Okamoto, N.Miura and N.Yamazoe, Solid State Ionics. **48**(1991)207

120. L.Hong, W.Chua, J.Memb.Sci. **198**(2002)95

121. Y.Liu, L.Hong, J.Memb.Sci. **224**(2003)137

122. L.Hong, X.Chen, Z.Cao, J.Europ.Ceram.Soci. **21**(2001)2207

123. K.Sahneer, R.Moos, M.Matam, J.J.Tunney, M.Post, Sensors

Actuators.B. **108**(2005)102

124. D.T.V.Anh, W.Olthuis, P.Bergveld, Sensors Actuators.B. **103**(2004)165

125. P. Moseley, D. Williams, Polyhedron. **8**(1989)1615

126. D. Niemeyer, D.E. Williams, P. Smith, K.F. Pratt, B. Slater, C.R.A.Catlow, A.M. Stoneham, J. Mater. Chem. **12**(2002)666

127. Y.C.Chen, Y.H.Chang, G.J.Chen, Y.L.Chai, D.T.Ray, Sensors Actuators.B. **96**(2003)82

128. C.M. Chiu, Y.H. Chang, Thin Solid Films **342**(1999)15

129. D. Dimos, C. H. Mueller, Annu. Rev. Mater. Sci. **28**(1998)397

130. G.H.Jonker, J.H.Van Santen, Physica. **19**(1953)120

131. J.B.Goodenough, J. Phys. Chem. Solids. **6**(1958)287

132. H.Ohbayashi, T.Kudo, T.Gejo, Jpn.J.Appl.Phys. **13**(1974)1

133. J.Liu, L.He, G.Chen, W.Su, J.Mater.Sci. **32**(1997)203

134. C.N.R.Rao, O.Prakash, D.Bahadur, P.Ganguly, S.Nagabhushana, J.Solid.State.Chem. **22**(1977)353

135. P.M.Racch, J.B.Goodenough, J.Appl.Phys. **39**(1968)1209

136. V.G.Sathe, A.V.Pimpale, V.Siruguri, S.K.Paranjpe, J.Phys.Condens.Matter. **8**(1996)3889

137. P.V.Vanitha, A.Arulraj, P.N.Santhosh, C.N.R.Rao, Chem.Mater. **12**(2000)1666

138. V.G.Bhide, D.S.Rajoria, C.N.R.Rao, G.R.Rao, V.G.Jadhao, Phys.Rev.B. **12**(1975)2832

139. J.P.Kemp, D.J.Beal, P.A.Cox, J.Solid.State.Chem. **86**(1990)50

140. E.Fatuzzo, W.J.Merz, *Ferroelectricity,* North-Holland Publishing company, Amsterdam. 1967, pp.10

141. P.Ganguly, N.Y.Vasanthacharya, C.N.R..Rao, P.P.Edwards, J.Solid State.Chem. **54**(1984)400

142. A.Chainani, M.Mathew, D.D.Sharma, Phys.Rev.B. **46**(1992)9976

143. R.Caciuffo, D,Rinaldi, G,Barucca, J.Mira, J.Rivas, M.A.Senaris Rodriguez, P.G.Radaelli, D.Fiorani, J.B.Goodenough, Phys.Rev.B.

59(1999)1068

144. R.Mahendiran, A.K.Raychaudhuri, A.Chainani, D.D.Sharma, J. Phys. Condens. Matter. 7(1995)L561

145. K.Asai, P.Gehring, H.Chou, G.Shirane, Phys.Rev.B. 40(1989)10982

146. M.A.Senaris-Rodriguez, J.B.Goodenough, J.Solid.State.Chem. 118(1995)323

147. J.M.Daughton, A.V.Pohm, R.T.Fayfield, C.H.Smith, J. Phys.D Appl.Phys. 32(1999)R169

148. W.H.Butler, A.Gupta, Nature. Mater. 3(2004)845

149. A. Maignan, *Colossal Magnetoresistive Materials*, in *Encyclopedia of SMART Materials*, Volume 1 and Volume 2, edited by M.Schwartz, John Wiely and Sons Inc., New York. 2002, pp. 202

150. R.M.Kusters, D.A.Singleton, D.A.Kenn, R.McGreevy, W.Hayes, Physica B. 155(1989)362

151. A.Congeduti, P.Postorino, E.Caramagno, M.Nardone, A.Kumar, D.D.Sarma, Phys.Rev.Lett. 86(2000)1251

152. C.N.R.Rao, J.Phys.Chem.B 104(2000)5877

153. E.Dagotto, T.Hotta, A.Moreo, Physics Reports. 344(2001)1

154. R.Mahendiran, A.K.Raychaudhuri, Phys.Rev.B. 54(1996)16044

155. P.Ganguly, P.S.Anil Kumar, P.N.Santhosh, I.S.Mulla, J.Phys.Condens.Matter. 6(1994)533

156. J.Wu, C.Leighton, Phys.Rev.B. 67(2003)0174408

157. G. H.Jonker, J.H.Van Santen, Physica. 16(1950)337

158. C.Zener, Phys.Rev. 82(1951)403

159. P.W.Anderson, H.Hasegawa, Phys.Rev. 100(1955)675

160. R.von Helmolt, J.Wecker, B.Holzapfel, L.Schultz, K.Samwer, Phys. Rev. Lett. 71(1993)2331

161. S.Jin, T.H.Tiefel, M.McCormack, R.A.Fastnacht, R.Ramesh, L.H.Chen, Science. 264(1994)413

162. G.C.Xiong, Q.Li, H.L Ju, S.N.Mao, L.Senapati, X.X.Xi, R.L.Green, T.Venkatesan, Appl.Phys.Lett. 66(1995)1427

163. Y.Tokura, Rep.Prog.Phys. **69**(2006)797

164. Y.Tokura, A.Urushibara, Y.Moritomo, T.Arima, A.Asamitsu, G.Kido, N.Furukawa, J. Phys. Soc. Japan **63**(1994)3931

165. A.Urushibara, Y.Moritomo, T.Arima, A.Asamitsu, G.Kido, Y.Tokura, Phys.Rev.B **51**(1995)14103

166. H. Fujishiro, M. Ikebe, Y. Konno, J.Phys.Soc.Jpn. **67**(1998)1799

167. S.Yunoki, A.Moreo, Phys.Rev.B. **58**(1998)6403

168. J.B.Goodenough, Phys.Rev. **100**(1955)564

169. A.Barnabe, M.Hervieu, A.Maignan, C.Martin, B.Raveau, J.Appl.Phys. **84**(1998)5506

170. G.Zhao, K.Conder, H.Keller, K.A.Muller, Nature. **381**(1996)676

171. A. J. Millis, P. B. Littlewood, B. I. Shraiman, Phys. Rev. Lett. **74**(1995)5144

172. A.J.Millis, B.I.Shraiman, R.Mueller Phys. Rev. Lett. **77**(1996)175

173. H.Roder, J.Zhang, A.R.Bishop Phys. Rev. Lett. **76**(1996)1356

174. J.R.Fletcher, K.W.H.Stephens, J. Phys. C. Solid State Phys. **2**(1969)444

175. A.P.Ramirez, J. Phys.Conds.Matter. **9**(1997)8171

176. M .Uehara, S .Mori, C.H Chen, S-W Cheong Nature. **400**(1999)405

177. S.Yamaguchi, H.Taniguchi, H.Takagi, T.Arima, Y.Tokura, J.Phys.Soc.Jpn. **64**(1995)1885

178. M.Imada, A.Fujimori, Y.Tokura, Rev.Mod.Phys. **70**(1998)1039

179. S.Yamaguchi, Y.Okimoto, Y.Tokura, Phys.Rev.B. **55**(19997)R8666

180. S.R.English, J.Wu, C.Leighton, Phys.Rev.B. **65**(2002)220407

181. M.Itoh, I.Natori, S.Kubota, K.Motoya, J.Magn.Magn. **140-144**(1995)1811

182. S. Tsubouchi, T. Kyomen, M. Itoh, P. Ganguly, M. Oguni, Y Shimojo, Y. Mori, Y. Ishii, Phys. Rev. B **66**(2002)052418

183. Y.Moritomo, K.Higashi, K.Matsuda, A.Nakamura, Phy.Rev.B. **55**(1997)R14725

184. X.Xu, L.Jiang, J.Shen, Z.Chen, Z.Xu, Phys.Lett.A. **351**(2006)431

185. M.Itoh, I.Natori, J.Phys.Soc.Jpn. **64**(1995)970

186. P. Ravindran, H. Fjellvag, A. Kjekshus, P. Blaha, K. Schwarz, J. Luitz, J. Appl. Phys. **91**(2002)291

187. M. A. Korotin, S. Yu. Ezhov, I. V. Solovyey, V. I. Anisimov, D. I.Khomskii, G. A. Sawatzky, Phys. Rev. B. **54**(1996)5309

188. H-W.Hsu, Y-H.Chang, G-J.Chen, Jpn.J.Appl.Phys. **39**(2000)61

189. S.Mukherjee, R.Ranganathan, P.S.Anilkumar, P.A.Joy, Phys.Rev.B. **54**(1996)9267

190. G.Briceno, H.Chang, X.Sun, P.G.Schultz, X.D.Xiang, Science **270**(1995)273

191. J-M.Liu, C.K.Ong, Appl.Phys.Lett. **73**(1998)1047

192. J.Wu, J.W.Lynn, C.J.Glinka, J.Burley, H.Zheng, J.F.Mitchell, C.Leighton, Phys.Rev.Lett. **90**(2005)037201

CHAPTER 2

Thin Film Deposition Techniques and Characterization Tools

This chapter describes the various thin film deposition techniques employed for the growth of the thin films and the various characterisation methods used in the present investigation.

65

2.1 Introduction

A thin film is defined as a low-dimensional material created by condensing atomic/molecular/ionic species of matter one-by-one. Thin films have been extensively used in physical research and applications [1]. The basic properties of thin films such as composition, crystal phase and orientation, film thickness and microstructure are controlled by deposition conditions. A wide variety of microstructures and consequently properties can be obtained by simply varying the deposition conditions during the growth of the film. Thin film properties are strongly dependent on the methods of deposition, the substrate materials, the substrate temperature, the rate of deposition and the background pressure. The application and the properties of the given material determine the most suitable technique for the preparation of thin films of that material.

The thin films prepared for the studies presented in this thesis were mainly deposited using radio frequency (rf) magnetron sputtering. Lanthanum Strontium Cobalt Oxide (LSCO) and Lanthanum Strontium Cobalt Nickel Oxide (LSCNO) thin films were deposited by rf magnetron sputtering. The structural, optical and electrical properties of these films were studied using different characterisation tools. LSCO and LSCNO were used as the electrodes for the fabrication of ferroelectric capacitors. The thin films of the ferroelectric materials, Barium Strontium Titanate (BST) and Lead Zirconium Titanate (PZT) were prepared by pulsed laser deposition.

2.2 Thin Film Preparation Techniques

Generally any thin film deposition follows the sequential steps: a source material is converted into the vapour form (atomic/molecular/ionic species) from the condensed phase (solid or liquid), which is transported to the substrate and then it is allowed to condense on the substrate surface to form the solid film [2]. Depending on how the atoms/molecules/ions/clusters of species are created for the condensation process, the deposition techniques

are broadly classified into two categories, viz. physical methods and chemical methods.

Chemical bath deposition, chemical vapour deposition, and spray pyrolysis are examples of chemical method of thin film deposition. Thermal evaporation, electron beam evaporation, rf and dc sputtering and pulsed laser deposition (PLD) are examples of physical methods of thin film preparation.

The following sections discuss the methodology and experimental set-up used in various thin film deposition techniques.

2.2.1 Thermal evaporation by resistive heating

Thermal evaporation is the most widely used technique for the preparation of thin films of metals, alloys, and also many compounds. A vacuum environment in which sufficient amount of heat is given to the evaporants to attain the vapour pressure necessary for the evaporation, is the only requirement for thermal evaporation. The evaporated material is allowed to condense on a substrate kept at a suitable temperature.

When evaporation is made in vacuum, the evaporation temperature will be considerably lowered and the formation of the oxides and incorporation of impurities in the growing layer will be reduced. Evaporation is normally done at a pressure of 10^{-5} Torr. At this pressure a straight line path for most of the emitted vapour atoms is ensured for a substrate to source distance of nearly 10 to 50 cm [3]. The characteristics and quality of the deposited film will depend on the substrate temperature, rate of deposition, ambient pressure, etc. and the uniformity of the film depends on the geometry of the evaporation source and its distance from the source. The deposition by thermal evaporation is simple, convenient and is widely used [4]. Thermal evaporation by resistive heating has been used for the deposition of metal electrodes in the present study.

2.2.2 Sputtering

Sputtering is one of the most versatile techniques used for the deposition of thin films when device quality films are required. Sputtering process produces films with better controlled composition, provides films with greater adhesion and homogeneity and permits better control of film thickness. The sputtering process involves the creation of gas plasma usually of an inert gas such as argon [5] by applying voltage between a cathode and anode. The cathode is used as a target holder and the anode is used as a substrate holder. Source material is subjected to intense bombardment by ions. By momentum transfer, particles are ejected from the surface of the cathode and they diffuse away from it, depositing a thin film onto a substrate. Sputtering is normally performed at a pressure of 10^{-2}-10^{-3} Torr.

There are two modes of powering the sputtering system; dc and rf biasing. In dc sputtering system a direct voltage is applied between the cathode and the anode. This method is restricted for conducting targets only. RF sputtering is suitable for both conducting and non-conducting targets; a high frequency generator (13.56 MHz) is connected between the electrodes of the system.

In the process of sputtering, the material is knocked out of a surface by heavy argon ions and travel across the system to condense onto the substrate surface. For the sputtered material to arrive at the substrate surface with the high energy necessary to give a good coating, and for the process to be efficient, it is important for the material to travel without collision with the residual gas in the vacuum. However, the residual gas pressure needed to maintain a simple electrical discharge, in order to provide the argon ions for bombardment, is too high to allow transfer of the sputtered material without many collisions. This results in very slow deposition rate and poor quality coating. A magnetron uses a magnetic field to confine electrons close to the cathode, making it easier to sustain an electrical discharge at low pressure. Magnetron sputtering is particularly useful when high deposition rates and low substrate temperatures are required [6]. Both reactive and non-reactive forms of dc, rf and magnetron sputtering can be employed for the deposition

of thin films. In reactive sputtering, the reactive gas is introduced into the sputtering chamber along with argon to deposit oxide films. The deposition rates and properties of the films strongly depend on the sputtering conditions such as the partial pressure of the reactive gas, the sputtering pressure, substrate temperature and target to substrate spacing.

In sputter deposition, the material arrives at the substrate mostly in atomic or molecular form. The atom diffuses around the substrate with a motion determined by its binding energy to the substrate, which is influenced by the nature and temperature of the substrate. The depressions on the substrate surface act as adsorption sites for the diffusing atoms. At each hop, the atom will either jump over the barrier into an adjacent site or will re-evaporate. After a certain time, the atom will either evaporate from the surface or will join another diffusing single atom to form a doublet. These doublets will be joined by other single atoms to form triplets, quadruplets and so on. This stage is known as the nucleation stage of thin film growth and it leads to the formation of quasi-stable islands. The islands will grow in size and it will lead to the coalescent stage. Coalescence proceeds until the film reaches continuity.

Sputtering may be carried out in a variety of systems, which may differ in sputtering configuration, geometry, target type etc. Experimental sputtering systems usually have small targets and low production rates, whereas commercial production systems have large targets and rapid substrate transport to maximize production rate. Irrespective of the sputtering system used, the basic sputtering process remains the same. Figure 2.1 shows a typical sputter deposition system.
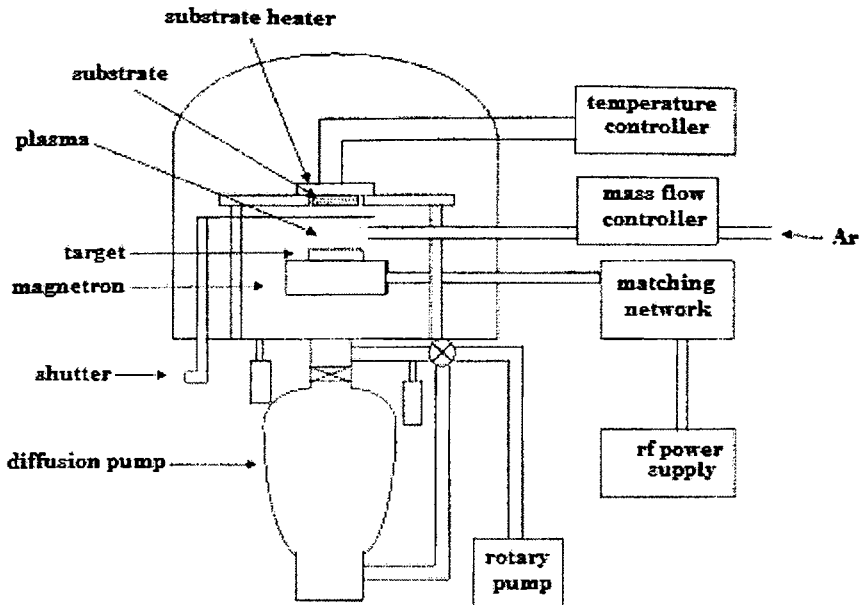
Figure 2.1 Schematic sketch of rf sputter deposition system

The process of rf sputter deposition is made possible due to the large difference in mass, and hence mobility, of electrons and inert gas ions. Because electrons are many times less massive than ions, electrons attain much greater velocities and travel much further than ions during each cycle of the applied rf voltage waveform. Since electrons travel much further, they eventually accumulate on the target, substrate and chamber walls such that the plasma is the most positive potential in the system. These induced negative voltages or "sheath voltages", cause acceleration of positive ions toward the negatively charged surfaces, which subsequently leads to sputtering events. The volume adjacent to a surface tends to be relatively free of electrons because of the negatively charged surface. This leads to a "dark space" because electrons are not available to excite gas atoms [7].

The target is selectively sputtered by controlling the relative surface areas of the target and the substrate holder. If space charge limited current is assumed, the ion current flux, J can be estimated by the Child-Langmuir equation [7],

$$J = \frac{KV^{3/2}}{D^2 m_{ion}}$$
(2.1)

where D is the dark space thickness, V is the sheath voltage, m_{ion} is the ionic mass and K is the proportionality constant. Since the positive ion current must be equal at both the electrodes,

$$\frac{A_A V_A}{D_A^2} = \frac{A_B V_B}{D_B^2}$$
(2.2)

where A_A and A_B are the surface areas of electrodes A and B respectively (figure 2.2). It should be noted that this step differs from the assumption of treating the positive ion current densities equal.
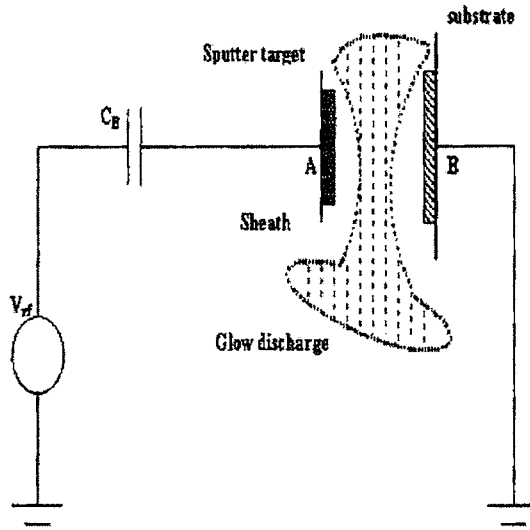

Figure 2.2 Deposition process during rf sputtering

If the positive ion current densities were equal, there would be a much greater positive ion current flowing during one half cycle of the applied voltage waveform than the other due to the much greater area of the grounded substrate electrode. Therefore, because this system is assumed to

72

be in steady state, the total positive ion current per half cycle should be the relevant quantity.

The glow discharge itself is a region where large quantities of positive and negative charge exist and can be modelled as a wire. Since most of the voltage in the glow discharge is dropped across the dark space, and they have small conductivities, they can be modelled as capacitors such that the capacitances,

$$C \propto A/D \tag{2.3}$$

Furthermore, an ac voltage will divide across two series capacitors such that,

$$\frac{V_A}{V_B} = \frac{C_B}{C_A} \tag{2.4}$$

From equations (2.1), (2.2) and (2.3),

$$\frac{V_A}{V_B} = \left(\frac{A_B}{A_A} \right)^2 \tag{2.5}$$

This equation tells that smaller area will see larger sheath voltage, whereas larger area will see a smaller sheath voltage by a power of 2. The usefulness of this result is that $A_B > A_A$ must hold to selectively sputter the target. This is done in practice by grounding the substrate holder to the entire chamber resulting in a very large A_B. For this reason it is extremely important that the substrate holder and the system are well grounded to ensure that resputtering of the growing film does not occur.
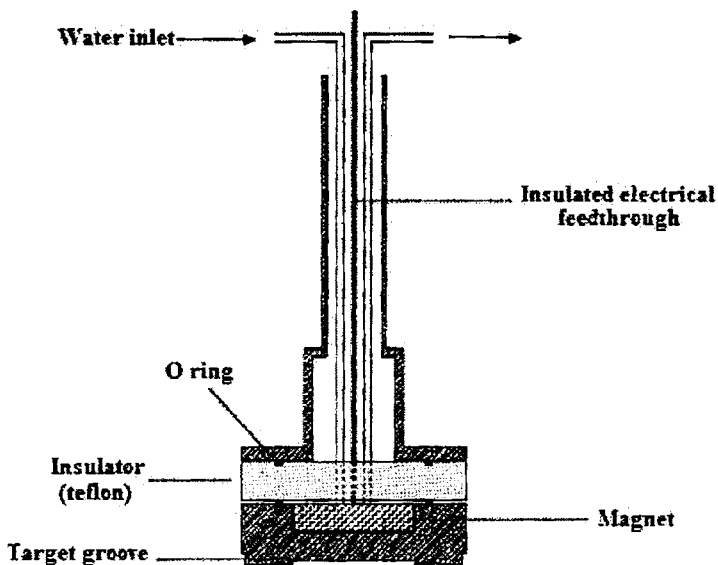
Figure 2.3 Schematic structure of the magnetron

We have used a Sierra Applied Sciences, (USA) made magnetron for the rf sputtering of LSCO and LSCNO thin films. A schematic diagram of the magnetron is shown in figure 2.3. The vacuum system consists of a six-inch diameter diffusion pump backed by a rotary pump (make - HindHivac, Bangalore). The rf supply was connected to the magnetron through a capacitive matching network (make - Huttinger Electronic, Germnay). The flow of argon gas and oxygen into the vacuum chamber was controlled using mass flow controllers (make - Aalborg, USA).

Sputtering facilitates the stoichiometric deposition of the mixed conducting oxide thin films LSCO and LSCNO. Raymond et al. [8] has investigated the influence of O_2:Ar sputter gas ratio on the properties of LSCO thin films. The thin films were deposited on quartz, $LaAlO_3$ and $Pt/Ti/TiO_2/SiO_2/Si$ substrates. The resistivity of the LSCO thin films was found to decrease with the increase of O_2:Ar ratio. The improvement in the LSCO film properties with O_2:Ar ratio is due to the increase in the stoichiometry of oxygen. Many groups have investigated the fabrication of LSCO by rf magnetron sputtering for the use of bottom electrode of PZT capacitors. The as deposited films

74

were all subjected to a post deposition annealing in oxygen atmosphere in the temperature range from 450 °C - 675 °C to improve the crystallinity and conductivity [9, 10]. Recently a detailed investigation of the deposition parameters on the composition, microstructure and electrical properties of the LSCO thin films by rf magnetron sputtering was done by Klenov et al. [11]. The total sputter pressure was found to be an important parameter in controlling composition of the LSCO film. The oxygen partial pressure as well as the cationic stoichiometry was found to influence the film resistivity. Increasing the oxygen partial pressure during deposition was ineffective in decreasing the resistivity because it negatively affected the cation stoichiometry. Electrical resistivity could be reduced by cooling the thin films in oxygen after deposition, consistent with the observation that oxygen deficiency dominates the electrical properties of cation stoichiometric films. There are also reports on the preparation of LSCNO thin films by rf magnetron sputtering for application in gas sensors. Chiu et al. [12] has prepared LSCNO thin films by rf magnetron sputtering at an rf power of 200 W at an Ar:O_2 ratio 2:1 at a total deposition pressure of 0.133 Pa. The as prepared films showed a ($0\overline{2}1$) preference orientation which changed into a polycrystalline nature on post deposition annealing at 700 °C. Based on these observations in literature, the sputtering unit for the present study was designed with special heater which can heat the substrate up to 800 °C in oxygen ambient.

2.2.3 Pulsed Laser Deposition

Pulsed laser deposition (PLD) is clearly emerging as one of the premier thin film deposition technologies. PLD has gained a great deal of attention in the past few years for its ease of use and success in depositing materials of complex stoichiometry. PLD was the first technique used to successfully deposit a superconducting $YBa_2Cu_3O_{7-\delta}$ thin film. Since that time, many materials that are normally difficult to deposit by other methods, especially multi-element oxides, have been successfully deposited by PLD. In the case of multielemental compounds such as high temperature superconductors,

ferroelectrics and for electro optic materials, this technique is extremely successful. This technique offers many potential applications, from integrated circuits and optoelectronics to micro mechanics and medical implants [13]. The best quality films can be deposited by controlling the fundamental criteria of the substrate temperature (T), the relative and absolute arrival rates of atoms (R_i, where i could vary from 1 to 6) and the energy of the depositing flux (E). PLD offers the best control over these criteria than other vacuum deposition techniques [14].
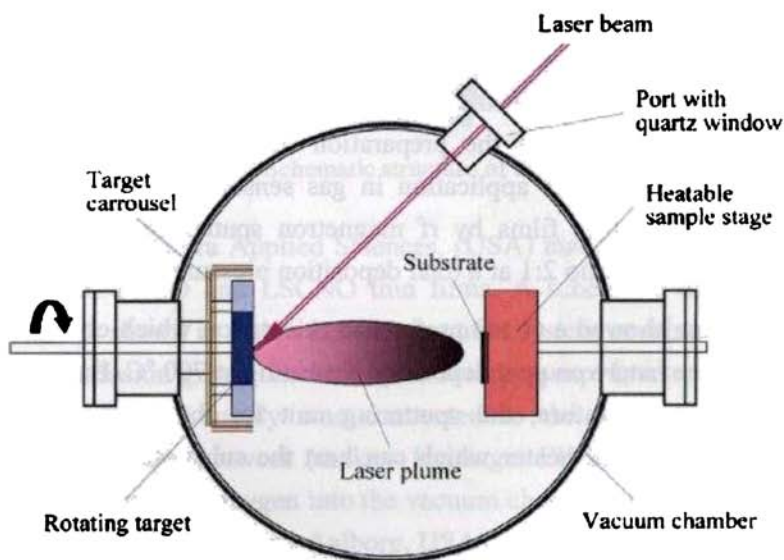

Figure 2.4 Schematic diagram of the pulsed laser deposition system

Figure 2.4 shows the schematic diagram of a pulsed laser deposition system. The main advantage of PLD derives from the laser material removal mechanism; PLD relies on a photon interaction to create an ejected plume of material from any target. The vapor (plume) is collected on a substrate placed at a short distance from the target. Though the actual physical processes of material removal are quite complex, one can consider the ejection of material to occur due to rapid explosion of the target surface due to superheating. Unlike thermal evaporation, which produces a vapor

composition dependent on the vapor pressures of elements in the target material, the laser-induced expulsion produces a plume of material with stoichiometry similar to the target. It is generally easier to obtain the desired film stoichiometry for multi-element materials using PLD than with any other deposition techniques.

Typical plasma temperature measured by emission spectroscopy during initial expansion is $\approx$ 10,000 K, which is well above the boiling point of most materials ($\approx$ 3000 K). Heating of the plasma to these temperatures is thought to occur by inverse–Bremsstrahlung absorption of the laser light in a free – free transition of electron ion pair. This high temperature would evaporate the surface layer of the target thereby producing exact composition in the thin films.

The main advantages of pulsed laser deposition are:

- *conceptually simple*: a laser beam vaporizes a target surface, producing a film with the same composition as the target.
- *versatile*: many materials can be deposited in a wide variety of gases over a broad range of gas pressures.
- *cost-effective*: one laser can serve many vacuum systems.
- *fast*: high quality samples can be grown reliably in 10 or 15 minutes.
- *scalable:* as complex oxides move toward volume production.

(i) Mechanisms of PLD

The mechanism of pulsed laser deposition, in contrast to the simplicity of the set-up, is a very complex physical phenomenon. It not only involves the physical process of the laser-material interaction of the impact of high-power pulsed radiation on solid target, but also the formation plasma plume with high energetic species and even the transfer of the ablated material through the plasma plume onto the heated substrate surface. Thus the thin film formation process in PLD generally can be divided into the following four stages.

1. Laser radiation interaction with the target
2. Dynamics of the ablated materials
3. Deposition of the ablation materials on the substrate
4. Nucleation and growth of a thin film on the substrate surface

Each stage in PLD is critical to the formation of quality epitaxial, crystalline, stoichiometric and uniform thin film.

In the first stage, the laser beam is focused onto the surface of the target. At sufficiently high flux densities and short pulse duration, all elements in the target are rapidly heated up to their evaporation temperature. Materials are dissociated from the target surface and ablated out with stoichiometry as in the target. The instantaneous ablation rate is highly dependent on the fluences of the laser shining on the target. The ablation mechanisms involve many complex physical phenomena such as collisional, thermal, and electronic excitation, exfoliation and hydrodynamics.

During the second stage the emitted materials tend to move towards the substrate according to the laws of gas-dynamics and show the forward peaking phenomenon. The spatial thickness varies as a function of $\cos \theta$. The spot size of the laser and the plasma temperature has significant effects on the deposited film uniformity. The target-to-substrate distance is another parameter that governs the angular spread of the ablated materials. A mask placed close to the substrate could reduce the spreading.

The third stage is important to determine the quality of thin film. The ejected high-energy species impinge onto the substrate surface and may induce various type of damage to the substrate. These energetic species sputter some of the surface atoms and a collision region is formed between the incident flow and the sputtered atoms. Film grows after a thermalized region is formed. The region serves as a source for condensation of particles. When the condensation rate is higher than the rate of particles supplied by the sputtering, thermal equilibrium condition can be reached quickly and film grows on the substrate surface at the expenses of the direct flow of the ablation particles and the thermal equilibrium obtained.

The effect of increasing the energy of the adatoms has a similar effect of increasing substrate temperature on film growth [14]. Typical power densities involved in PLD are approximately 50 MWcm^{-2} for a reasonable growth rate (> 1 A$^{\circ}$/shot). If plasma is formed during laser target interaction in vacuum or in air then an explicit laser-plasma interaction occurs. Due to which ions in the plasma are accelerated to as much as 100-1000 eV [14]. Nucleation-and-growth of crystalline films depends on many factors such as the density, energy, ionization degree, and the type of the condensing material, as well as the temperature and the physico-chemical properties of the substrate. The two main thermodynamic parameters for the growth mechanism are the substrate temperature T and the supersaturation D_m. They can be related by the following equation

$$D_m = kT \ln(R/R_e) \tag{2.6}$$

where k is the Boltzmann constant, R is the actual deposition rate, and R_e is the equilibrium value at the temperature T.

The nucleation process depends on the interfacial energies between the three phases present viz., the substrate, the condensing material and the vapour. The critical size of the nucleus depends on the driving force, i.e. the deposition rate and the substrate temperature. For the large nuclei, a characteristic of small supersaturation, they create isolated patches (islands) of the film on the substrate, which subsequently grow and coalesce together. As the supersaturation increases, the critical nucleus shrinks until its height reaches on atomic diameter and its shape is that of a two-dimensional layer. For large supersaturation, the layer-by-layer nucleation will happen for incompletely wetted foreign substrates.

The crystalline film growth depends on the surface mobility of the adatom (vapour atoms). Normally, the adatom will diffuse through several atomic distances before sticking to a stable position within the newly formed film. The surface temperature of the substrate determines the adatom's surface diffusion ability. High temperature favors rapid and defect free crystal

growth, whereas low temperature or large supersaturation crystal growth may be overwhelmed by energetic particle impingement, resulting in disordered or even amorphous structures.

The mean thickness (N_{99}) at which the growing thin and discontinuous film reaches continuity, is given by the formula

$$N_{99} = A(1/R)^{1/3} \exp(-1/T) \tag{2.7}$$

where R is the deposition rate (supersaturation related) and T is the temperature of the substrate and A is a constant related to the materials [14]. In the PLD process, due to the short laser pulse duration (~10 ns) and hence the small temporal spread ($<=10$ ms) of the ablated materials, the deposition rate can be enormous (~10 nm/s). Consequently a layer-by-layer nucleation is favored and ultra-thin and smooth film can be produced. In addition the rapid deposition of the energetic ablation species helps to raise the substrate surface temperature. In this respect PLD tends to demand a lower substrate temperature for crystalline film growth.

Most of the reports on the preparation of LSCO thin films are by pulsed laser deposition. PLD shows the unique advantage of preparing multicomponent oxide thin films with stoichiometric composition without subsequent high temperature oxygen annealing. The influence of various deposition parameters such as substrate temperature, oxygen partial pressure during deposition, post deposition annealing conditions and the effects of various substrates on the LSCO thin films has been investigated in detail by many groups. The BST and PZT thin films for the fabrication of ferroelectric capacitors in the present study were deposited by pulsed laser deposition. The depositions were carried out in a vacuum chamber pumped by a six-inch diffusion pump backed by a rotary pump (Indovision, Bangalore). The laser used was the third harmonics (355 nm) of Nd:YAG laser (Spectra Physics model GCR 150). The flow of oxygen into the chamber was controlled using a mass flow controller (Bronkhorst, Holland).

2.3 Characterisation tools

The optimisation of the preparation conditions is the main task in order to get device quality films. This has to be carried out on the basis of detailed structural, morphological, optical and electrical properties of the films obtained at different growth conditions. In the following sections the techniques used for the film characterizations are discussed briefly.

2.3.1 Thin film thickness

Thickness plays an important role in the film properties unlike a bulk material. Reproducible properties are achieved only when the film thickness and the deposition parameters are kept constant. Film thickness may be measured either by in-situ monitoring of the rate of deposition or after the film deposition. The thicknesses of the thin films prepared for the work presented in this thesis were measured by a stylus profiler (Dektak 6M).

(i) Stylus Profiler

The thickness measurement is done by the stylus profiler by electromechanically moving the sample beneath a diamond tipped stylus (figure 2.5). The high precision stage moves the sample according to a user defined scan length, speed and stylus force. The stylus is mechanically coupled to the core of a linear variable differential transformer (LVDT). As the stage carries the sample, the stylus moves over the sample surface. Surface variations cause the stylus to be translated vertically. Electrical signals corresponding to the stylus movement are produced as the core position of the LVDT changes. The LVDT scales an ac reference signal proportional to the position change, which in turn is conditioned and converted to a digital format through a high precision, integrating, analog-to-digital converter [15]. The film whose thickness has to be measured is deposited with a region masked this creates a step on the sample surface. The thickness of the sample can be measured accurately by measuring the vertical motion of the stylus over the step.
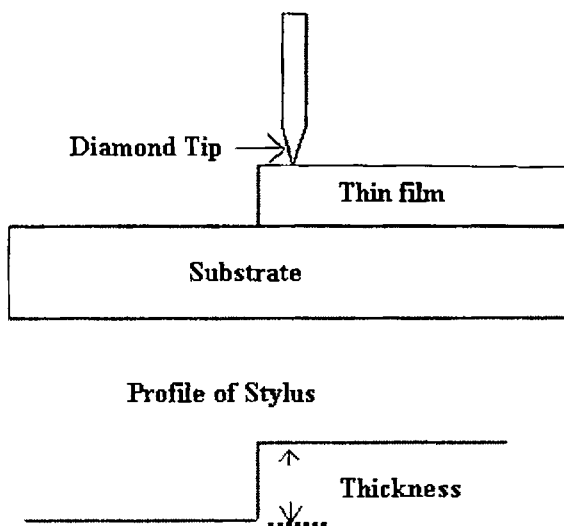
Figure 2.5. Schematic diagram illustrating the determination of thin film thickness with Stylus Profiler

2.3.2 X-ray diffraction studies

Electrical and optical properties of the thin films grown are influenced by the crystallographic nature of the films. X-ray diffraction (XRD) studies were carried out to study the crystallograoghic properties of the thin films prepared.

A given substance always produces a characteristic x-ray diffraction pattern whether that substance is present in the pure state or as one constituent of a mixture of substances. This fact is the basis for the diffraction method of chemical analysis. The particular advantage of x-ray diffraction analysis is that it discloses the presence of a substance and not in terms of its constituent chemical elements. Diffraction analysis is useful whenever it is necessary to know the state of chemical combination of the elements involved or the particular phase in which they are present. Compared with ordinary chemical analysis the diffraction method has the advantage that it is much faster, requires only very small sample and is non destructive [16].

The basic law involved in the diffraction method of structural analysis is the Bragg's law. When monochromatic x-rays impinge upon the atoms in a crystal lattice, each atom acts as a source of scattering. The crystal lattice acts as series of parallel reflecting planes. The intensity of the reflected beam at certain angles will be maximum when the path difference between two reflected waves from two different planes is an integral multiple of λ. This condition is called Bragg's law and is given by the relation,

$$2dSin\theta = n\lambda \qquad\qquad (2.8)$$

where n is the order of diffraction, λ is the wavelength of the x-rays, d is the spacing between consecutive parallel planes and θ is the glancing angle (or the complement of the angle of incidence)[17].

X-ray diffraction studies give a whole range of information about the crystal structure, orientation, average crystalline size and stress in the films. Experimentally obtained diffraction patterns of the sample are compared with the standard powder diffraction files published by the International Centre for Diffraction Data (ICDD).

The average grain size of the film can be calculated using the Scherrer's formula [16],

$$d = \frac{0.9\lambda}{\beta\cos\theta} \qquad\qquad (2.9)$$

where, λ is the wavelength of the x-ray and β is the full width at half maximum intensity in radians.

The lattice parameter values for different crystallographic systems can be calculated from the following equations using the (hkl) parameters and the interplanar spacing d.

Cubic system, $$\frac{1}{d^2} = \frac{h^2 + k^2 + l^2}{a^2}$$ (2.10)

Tetragonal system, $$\frac{1}{d^2} = \frac{h^2 + k^2}{a^2} + \frac{l^2}{c^2}$$ (2.11)

Hexagonal system, $$\frac{1}{d^2} = \frac{4}{3}\left(\frac{h^2 + hk + k^2}{a^2}\right) + \frac{l^2}{c^2}$$ (2.12)

X-ray diffraction measurements of the films in the present studies were carried out using Rigaku automated x-ray diffractometer. The filtered copper K_α (λ=1.5418A^0) radiation was used for recording the diffraction pattern.

2.3.3 Atomic Force Microscopy (AFM)

Following the invention of the scanning tunnelling microscope (STM), a number of new scanning probe microscopes (SPM) has been developed that use the key components of the STM. One of the most important SPM is the atomic force microscope (AFM) [18]. In atomic force microscopy a tip, integrated to the end of a spring cantilever, is brought within the interatomic separations of a surface, such that the atoms of the tip and the surface are influenced by interatomic potentials. As the tip is rastered across the surface, it bounces up and down with the contours of the surface. By measuring the displacement of the tip (*i.e.* the deflection of the cantilever), one can theoretically map out the surface topography with atomic resolution. The first AFM's measured cantilever deflections using a piggy-backed STM. Later instruments used more practical optical techniques. The AFM is essentially identical in concept to the scanning profilometer, except that the deflection-sensitivity and resolution are improved by several orders of magnitude. There are a large number of applications for the AFM, including biological systems, polymers, and a host of insulator and semiconductor materials.
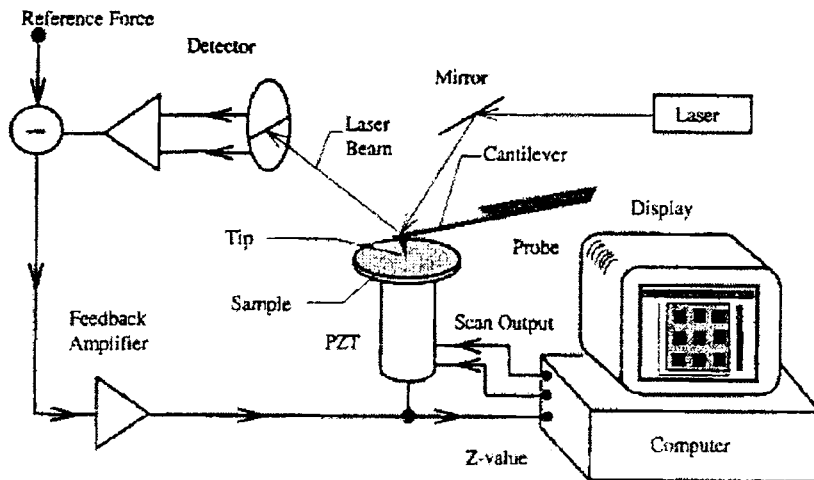
Figure. 2.6 The essential elements of an AFM

An AFM images a surface in a manner analogous to the gramophone stylus sensing the groves of gramophone disk. The essential elements of an AFM are shown in the figure 2.6. The tip is attached to a cantilever type spring as shown in the figure 2.7. As the tip and sample interact, forces act on the tip and cause the cantilever (spring) to deflect. The cantilever position is monitored by a position detector. The output of the detector is connected to a feedback controller that regulates the force between the sample and the tip by moving the sample up or down. The sample is moved by a PZT scanning actuator. The cantilever must be soft enough to deflect a measurable amount without damaging the surface features of the sample. The amount of deflection is proportional to the force acting on the tip.

$$F_{spring} = -k.\Delta Z \qquad (2.13)$$

where F is the force on the sample, k is the spring constant of the cantilever, and, ΔZ is the deflection of the cantilever.
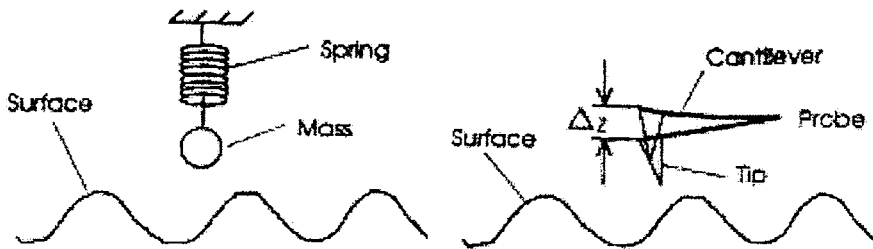
85

Figure. 2.7 Attachment of the tip to the cantilever in an AFM.

Various modes of AFM measurements include contact mode, dynamic force mode, phase mode. Friction force microscope, magnetic force microscope, surface potential microscope, etc are scanning probes microscopes slight variation in the working principles from that described above.

2.3.4 Optical characterisation

(i) Determination of band gap energy

Intrinsic optical absorption of a single photon across the band gap is the dominant optical absorption process in a semiconductor. When the energy of the incident photon ($h\nu$) is larger than the band gap energy the excitation of electrons from the valence band to the empty states of the conduction band occurs. The light passing through the material is then absorbed and the number of electron hole pairs generated depends on the number of incident photons $S_0(\nu)$ (per unit area, unit time and unit energy). The frequency ν is related to the wavelength λ by the relation, $\lambda = c/\nu$, where c is the velocity of light. The photon flux $S(x,\nu)$ decreases exponentially inside the crystal according to the relation [19],

$$S(x,\nu) = S_0(\nu) \exp(-\alpha x) \qquad (2.14)$$

where, the absorption coefficient α, ($\alpha(\nu) = 4\pi k\nu/c$) is determined by the absorption process in semiconductors and k is the extinction coefficient.

For the parabolic band structure, the relation between the absorption coefficient (α) and the band gap of the material is given by [20],

$$\alpha = \frac{A}{h\upsilon}\left(h\upsilon - E_g\right)^r \qquad (2.15)$$

where, $r = 1/2$ for allowed direct transitions, $r = 2$ for allowed indirect transitions, $r = 3$ for forbidden indirect transitions and $r = 3/2$ for forbidden direct transitions. A is the parameter which depends on the transition probability. The absorption coefficient can be deduced from the absorption or transmission spectra using the relation,

$$I = I_0 e^{-\alpha t} \qquad (2.16)$$

where, I is the transmitted intensity and I_0 is the incident intensity of the light and t is the thickness of the film. In the case of direct transition, from equation 2.16, $(\alpha h v)^2$ will show a linear dependence on the photon energy (hv). A plot of $(\alpha h v)^2$ against hv will be a straight line and the intercept on energy axis at $(\alpha h v)^2$ equal to zero will give the band gap energy. The transmissions of the thin films in the present study were recorded using Jasco V500 spectrophotometer.

2.3.5 Electrical characterisation

i) Low temperature resistivity and magnetoresistance of the bulk by four probe method

A four-probe in Vander paw configuration is used to measure the dependence of resistance on temperature by cooling the sample down to liquid He temperature. The electrical contacts on samples are made with the help of silver paste or indium solder. Lakeshore temperature controller (DRC-93CA) is used for measuring and controlling the temperature of the sample holder. Keithley source meter (model 2400) is used for sending the current through current leads, and the voltage across the voltage leads is

measured by Keithley sensitive digital voltmeter (model 182). The automation program is written in Quick Basic. A PC (HP486) is used for controlling and automated data collection using IEEE-488 interface. The measurement is started by controlling the temperature of sample using Lakeshore temperature controller. Then a specified current is passed through the sample and the voltage is measured across the voltage leads. After that the current direction is reversed and voltage is measured again. It cancels the off set voltage generated due to thermo emf, which is independent of the current direction. The process is repeated few times to improve the accuracy of the measurement. Then the temperature controller sets the next temperature and the measurement continues. The collected data is plotted online as resistance versus temperature on the computer monitor.

The resistivity (ρ) is determined from the measured resistance (R) from the following relation:

$$\rho = \left(\frac{A}{l}\right).R \qquad (2.17)$$

Where, A is the area perpendicular to current direction and l is the distance between the voltage leads.

The same setup can be used with a magnetic field for magnetoresistance measurements. The magnet provides a magnetic field up to 100 kOe.
The magnetoresistance ($\Delta\rho/\rho$), which is defined as

$$\frac{\Delta\rho}{\rho} = \frac{\rho_{(H,T)} - \rho_{(0,T)}}{\rho_{(0,T)}} \qquad (2.18)$$

where $\rho_{(H,T)}$ is the resistivity with field and $\rho_{(0,T)}$ is the resistivity without magnetic field. The magnetoresistance can be measured in two different modes; (*i*) Magnetoresistance as a function of temperature at constant

magnetic field, which is obtained from the measured resistance as a function of temperature in zero field and in presence of constant magnetic field (*ii*) Magnetoresistance as function of magnetic field at constant temperature can be obtained by measuring the resistance at various magnetic fields at that temperature. If the magnetic field is parallel to the current direction it is known as the longitudinal magnetoresistance and if it is perpendicular to the current direction it is known as the transverse magnetoresistance. The magnetoresistance data presented in this thesis is the longitudinal magnetoresistance.

ii) Thermoelectric power measurement

The thermo power measurement on the compounds has been carried out down to 4K using two stage closed cycle refrigerator. The thermo power sample holder consists of two copper blocks electrically insulated from the rest of the system but thermally connected to the cold head of the closed cycle refrigerator. The radiation shield and the vacuum of 10^{-5} mbar ensure the minimal heat leak. The temperature of the one block is measured using Si diode sensor with Lakshore temperature controller. The sample is kept in between the Cu blocks. Finite temperature difference of 2K is maintained between the two copper blocks by magnin wire heater wounded on one of the copper blocks. The temperature is sensed using Chromel-Gold/Fe (7%) thermocouple and controlled using lakeshore temperature controller. Thermopower is calculated as the ratio of thermoemf to the temperature difference. The absolute thermopower is then calculated by subtracting the measured thermopower from the thermopower of Cu. The temperature for which the thermo power is measured is calculated by taking the average between hot and cold

$$S_{total} = \Delta E / \Delta T \qquad\qquad (2.19)$$
$$S_{sample} = S_{cu} - S_{total} \qquad\qquad (2.20)$$

Copper normally has the thermopower about 1.5 μV/K and is positive. The thermoemf and thermocouple voltage are measured in precession Keithely

nanovoltmeter using Keithely scanner. The lakeshore temperature controller is used to measure and control the temperature. All the measurements are done through the computer automated GPIB interface and GWBASIC language.

iii) Resistivity of the thin films by two probe method

The resistivity of the films is determined by the two-probe method with the electrodes in planar geometry. High conducting silver paste was used as the electrodes. The current voltage measurements were carried out using a Keithley's source measure unit (Model SMU 236). The resistivity (ρ) of the films is calculated applying ohm's law, by the relation $\rho = RA/L$, where R is the resistance given by the slope of the current-voltage characteristic curves. A is the area of the film in planar geometry which is given by the product of the film thickness and the width of the film. L is the spacing between the electrodes.

2.3.6 Polarization Measurement

The hysteresis measurements of the fabricated capacitors were carried out using RT66A ferroelectric tester from Radiant Technologies (Albuquerque, NM). The polarization hysteresis loop can be obtained with the traditional Sawyer-Tower circuit mode or with a virtual ground mode [21]. The measurements in the present study were done in the virtual ground mode. The Sawyer-Tower circuit is composed of linear sense capacitor (C_s) connected in series with device under test (DUT). In this circuit the two capacitors have the same charge on them, and the polarization is obtained by measuring the voltage across the sense capacitor as shown in the figure 2.8. Even though the circuit is simple, the value of the sense capacitor has to be accurate and must have much higher capacitance than the ferroelectric capacitor to obtain accurate results.
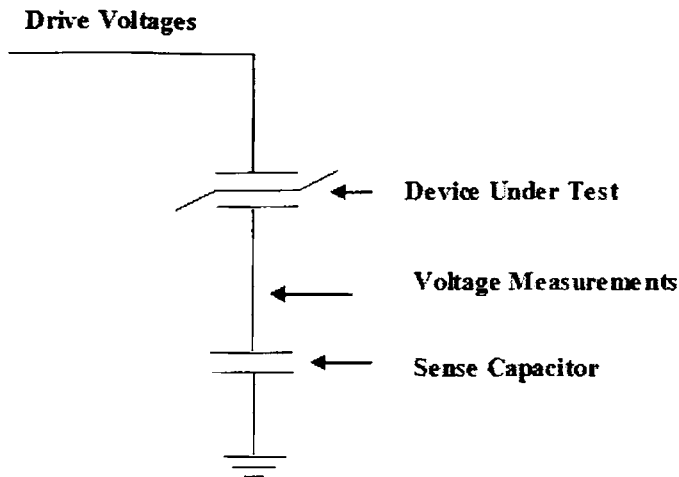
Figure 2.8. Basic Sawyer-Tower test configuration

The standard way of measuring the hysteresis loop is the virtual ground mode. In the virtual ground measuring system the sense capacitor in the Sawyer-Tower circuit is replaced with the measurement circuit as shown in figure 2.9. In this configuration, the transimpedance amplifier maintains the precision return terminal at a virtual ground potential. All of the charge that follows through the sample as a result of the applied drive voltage is collected by the integrator circuit. The voltage generated on the output of the integrator is then measured and translated into the test results that are displayed by the software. The precision drive and return circuitry are matched with respect to speed and current sinking ability. Thus the precision testers reject errors that might occur when the drive makes a transition faster than the transimpedance amplifier can follow. Therefore a large range of capacitance values over a large range of speeds can be measured accurately.
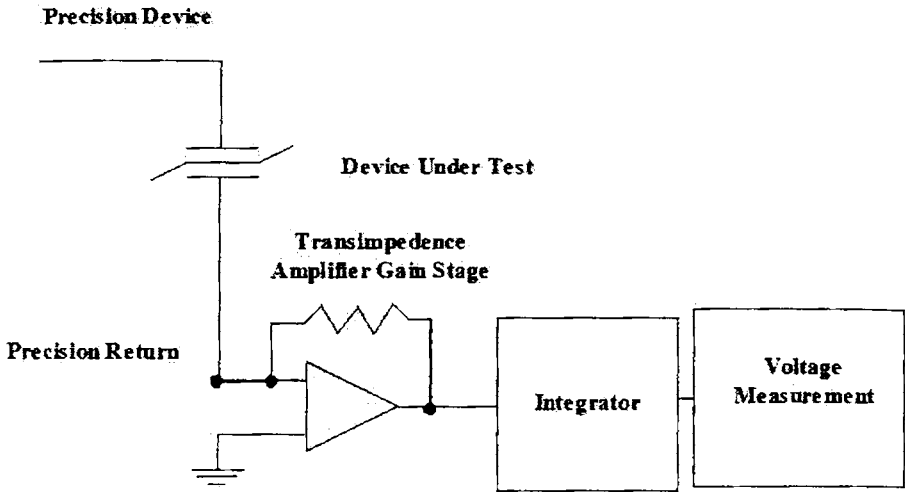
Figure 2.9. Virtual ground measuring system

There are basically two advantages of using the virtual ground measuring system rather than the Sawyer-Tower measuring system. In Sawyer-Tower measuring system the sense capacitor is susceptible to develop back voltage. When the drive voltage makes the transition to the maximum test voltage and then returns to zero volts, the charge collected in the sense capacitor generates a voltage known as the back voltage, which is applied in the opposite direction to the last drive voltage used to program the DUT. The back voltage may be minimized by the proper selection of the sense capacitor value. If the sense capacitor value is large (10 times) compared to the sample, the voltage across the sense capacitor generated by the charge flow through the sample is small and therefore the back voltage is minimized. In the virtual ground measuring system the DUT is never subject to back voltage because the measurement side of the sample that is connected to the return input of the system is "virtually grounded". In the Sawyer-Tower measuring system the parasitic capacitance of the measurement circuitry adds in parallel to the sense capacitance value. The accuracy of the Sawyer-Tower measurement depends directly on the accuracy of the value of the sense capacitor known. Therefore the parasitic capacitance value can introduce in accuracy in the measurement if the value of the sense capacitor is not large compared to the parasitic capacitance. But

in virtual ground mode the parasitic capacitance is associated with the return terminal. As this terminal is never allowed to gain voltage greater than zero volts the charge build up by the parasitic capacitance is zero. Therefore the parasitics that are associated with the return circuitry is essentially eliminated.

References

1. K.Wasa, M.Kitabatake, H.Adachi, *Thin Film Materials Technology, Sputtering of Compound Materials*, William Andrew Inc and Springer-Verlag GmbH & Co.KG, United States, 2004. pp.1

2. A.Goswami, *Thin Film Fundamentals*, New Age International (P) Limited, New Delhi, 1996. pp.2

3. K.L. Chopra, *Thin Film Phenomena*, Robert E. Krieger Publishing Co. Inc., New York, 1979.

4. L. Holland, *Vacuum Deposition of Thin films*, John Wiley & Sons Inc., New York, 1956. pp.3

5. D.L. Smith, *Thin-film deposition*, Mc Graw – Hill Inc, Washington D.C, 1995.

6. F.L.Akkad, A.Punnose, J.Prabu, J.Appl.Phys A **71**(2000)157

7. B.Chapman, *Glow Discharge Processes*, John Wiley & Sons, New York, 1980. pp.195

8. M. V. Raymond, H. N. Al-Shareef, B. A. Tuttle, D. Dimos, and J. T. Evans, Mater. Res. Soc. Symp. Proc. **433**(1995)145

9. H.N.Al-Shareef, B.A.Tuttle, W.L.Warren, D.Dimos, M.V.Raymond, M.A.Rodriguez, Appl.Phys.Lett. **68**(1996)272

10. B.T.Liu, K.Maki, S.Aggarwal, B.Nagaraj, V.Nagarajan, L.Salamanca-Riba, R.Ramesh, A.M.Dhote, O.Auciello, Appl.Phys.Lett. **80**(2002)3599

11. D.O.Klenov, W.Donner, L.Chen, A.J.Jacobson, S.Stemmer, J.Mater.Res. **18**(2003)188.

12. C.M.Chiu, Y.H.Chang, Senors and Actuators B, **54**(1999)236.

13. T.Venkatesan, S.M. Green; The industrial physicist, **2**(1996) 22.

14. Douglas B. Chrisey and Graham K. Hubler; *Pulsed Laser Deposition of Thin Films*, John Wiley and sons Inc., New York, 1994. pp 257

15. Veeco Dektak 6M Manual 2004.

16. C.Suryanarayana and M.Grant Norton, *X-ray diffraction A practical apporch*. Plenum Press New York, 1998. pp. 52

17. Charles Kittel, *Introduction to Solid State Physics,* Seventh edn, Wiley Eastern Limited, New Delhi, 1996 .pp.38

18. P. E .J. Flewit and R. K. Wild, *Physical methods for material characterization*, second edition, IOP publishing, London, 2003. pp. 505

19. J.I.Pankove, *Optical process in semiconductors*, Dover publications, New York, 1971. pp.3

20. J.Bardeen, F.J.Blatt, L.H. Hall, Proceedings of the conference on Photoconductivity, (1954) pp.146

21. Operation manual of the RT66A from Radiant Technology, Version 2.2 (Albuquerque,NM).

CHAPTER 3

Preparation and Characterization of
$La_{1-x}Sr_xCoO_3$ and $La_{0.5}Sr_{0.5}Co_{1-x}Ni_xO_3$

$La_{1-x}Sr_xCoO_3$ and $La_{0.5}Sr_{0.5}Co_{1-x}Ni_xO_3$ has been prepared by solid state reaction method. A detailed investigation of the structural and transport properties of these materials has been carried out. The properties were found to vary with the concentration of Sr^{2+} and Ni^{3+} in $La_{1-x}Sr_xCoO_3$ and $La_{0.5}Sr_{0.5}Co_{1-x}Ni_xO_3$ respectively. The observed magnetotransport properties were explained using the cluster model and the phase separation theory. The modified Heiks formula has been used to describe the observed thermoelectric behavior of the system.

-

99

3.1. Introduction

The wide spectrum of applications and the interesting properties make perovskite cobalt oxide $La_{1-x}Sr_xCoO_3$ an important candidate for scientific research. $La_{1-x}Sr_xCoO_3$ has potential applications in the field of catalysis, dense ceramic membrane, gas sensors, and as electrodes for oxide fuel cell [1-5]. The chemical and crystallographic compatibility of $La_{0.5}Sr_{0.5}CoO_3$ (LSCO) with ferroelectric materials makes it a suitable electrode for ferroelectric memories [6, 7]. The use of LSCO as a cathode in CO_2 lasers is reported to improve its output power and operating life [8]. Recently there have been investigations on the possibility of using $La_{1-x}Sr_xCoO_3$ as a thermoelectric material [9]. It has been reported that the partial substitution of Co by Ni in LSCO thin films decreases the resistivity of LSCO [10]. $La_{0.8}Sr_{0.2}Co_{1-x}Ni_xO_3$ powders and thin films have been used as a potential candidate for CO gas sensors as they exhibited strong oxidation to CO and could efficiently convert CO to CO_2 [11].

$La_{1-x}Sr_xCoO_3$ is obtained from $LaCoO_3$ by the partial substitution of Sr^{2+} for La^{3+}. Strontium substitution brings remarkable changes in the structural and transport properties and gives a complex phase diagram to the $La_{1-x}Sr_xCoO_3$ system [12, 13]. Even though the hole doping brings about the same changes in the transport and structural properties of the perovskite cobaltites and manganite systems, there are certain fundamental difference between the phase diagram of the two. These differences arise due to the unique properties of the cobaltites viz; the existence of spin state transitions and the presence of magnetic ground state in the doped systems. Since the crystal field splitting energy of the Co d states (E_g) and the Hunds rule exchange energy are comparable in cobaltites; there is only a small gap between the t_{2g} and e_g states which contributes to the spin state transitions in the system. For example in the parent compound $LaCoO_3$ where the difference is only 10 meV, t_{2g} electrons can be thermally excited into the high spin e_g state [3-5]. But in maganite systems the Hunds rule

exchange energy is larger than the crystal field splitting energy and the high spin state is stable in the Mn based systems [14]. The strong Hunds rule coupling prevents thermal variation of the spin state. The existence of a spin glass state with short range ferromagnetic ordering for low Sr^{2+} doping can be considered as the magnetic ground state for low doping in cobaltites. With higher Sr^{2+} doping the system evolves towards a ferromagnetic metallic state. But the Mn-based systems shows antiferromagnetic charge ordered insulating phase for low doping. It then evolves into a ferromagnetic insulator and ferromagnetic metal with further doping. These basic differences have renewed interest towards the study of magnetic properties of the cobalites [15]. Also the structural and electrical properties of these system changes remarkably with Sr^{2+} content. The Seebeck coefficient and the thermal conductivity of the $La_{1-x}Sr_xCoO_3$ with low Sr^{2+} content was found to be favorable for the use as thermoelectric material [9, 16]. Despite of the reports on the use of $La_{0.5}Sr_{0.5}Co_{1-x}Ni_xO_3$ system for gas sensing applications there are very few reports on the transport and structural aspect of these systems [10]. Therefore study of the $La_{1-x}Sr_xCoO_3$ and $La_{0.5}Sr_{0.5}Co_{1-x}Ni_xO_3$ system is important both scientifically and technologically.

In this chapter a detailed investigation on the preparation and characterization of $La_{1-x}Sr_xCoO_3$ and $La_{0.5}Sr_{0.5}Co_{1-x}Ni_xO_3$ system are discussed. $La_{1-x}Sr_xCoO_3$ system has been prepared for varying Sr^{2+} content and $La_{0.5}Sr_{0.5}Co_{1-x}Ni_xO_3$ system for varying Ni^{3+} content. The structural evolution of both the system with varying Sr^{2+} and Ni^{3+} content has been examined. The transport properties of the system with varying doping concentration of Sr^{2+} and Ni^{3+} have been studied using the temperature dependant measurement of resistivity, magnetoresistance and thermoelectric power. $La_{1-x}Sr_xCoO_3$ system is found to evolve from a semiconducting phase into a ferromagnetic metallic state with Sr^{2+} doping. Whereas the $La_{0.5}Sr_{0.5}Co_{1-x}Ni_xO_3$ system evolves into an insulating phase with Ni^{3+} doping. The magnetotransport and the thermoelectric properties of the system has been explained by considering the Co^{3+} and Co^{4+} ions in the intermediate spin state. A cluster model with short range ferromagnetic ordering

has been considered to explain the evolution of the magnetotranport properties of the system.

3.2. Experimental

The compounds of $La_{1-x}Sr_xCoO_3$ ($0.1 \leq x \leq 0.6$) powder were prepared by solid state reaction from stoichiometric mixtures of La_2O_3, $SrCO_3$, and Co_3O_4. Accurately weighed amounts of the reactants in required proportions were mixed together and were ball milled using ZrO_2 balls in de-ionized water for 24 hours. It was then dried and calcined for 24 hours at 1200 °C. The compounds of $La_{0.5}Sr_{0.5}Co_{1-x}Ni_xO_3$ were also prepared by solid state reaction described above from the stoichiometric mixtures of La_2O_3, $SrCO_3$, Co_3O_4 and NiO_3. Pellets of 10 mm diameter and 1 mm thickness were prepared from these powders. The pellets were then sintered at 1400 °C for 12 hours.

The structural characterizations were carried out using a Rigaku X-ray diffractometer with Cu K_α radiation (λ = 1.5418 A°). Resistance and magnetoresistance measurements were carried out by standard four probe method using a home made resistivity insert with Oxford superconducting magnet system. Magnetoresistance (MR) is defined as $[\Delta\rho/\rho = \{\rho(H)-\rho(0)\}/\rho(0)]$, where $\rho(H)$ and $\rho(0)$ are resistivity in the presence and in the absence of magnetic field respectively. For magnetoresistance measurements magnetic field is applied parallel to current direction. Thermoelectric measurements were done by differential technique down to 4K in a closed cycle refrigerator. In the differential technique the sample is sandwiched between two copper blocks and the temperature gradient (2 K) is maintained across them. Well polished surfaces of copper blocks and the sample facilitate better thermal contact and stability in the signal.

3.3. Results and Discussion

3.3.1 Structural Characterizations

Figure 3.1 shows the powder X-ray diffraction (XRD) pattern of the $La_{0.5}Sr_{0.5}CoO_3$ along with fitted curve obtained after Reitveld refinement. The analysis gave a good fit and the structure was identified as rhombohedral distorted perovskite structure; space group $R\bar{3}C$. Table 3.1 gives the refined structural parameters. The lattice parameters obtained are in agreement with earlier results [17].
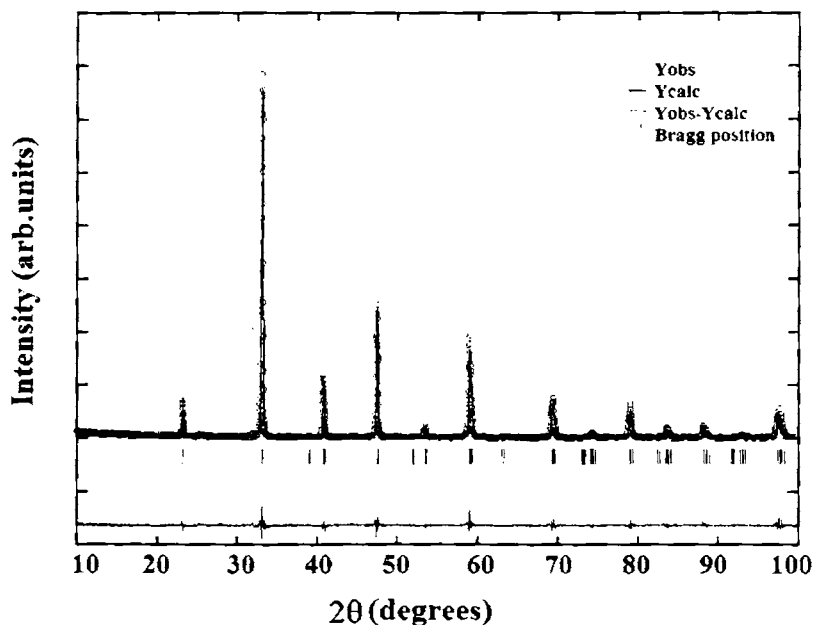

Figure 3.1. Powder XRD pattern (open circles) of $La_{0.5}Sr_{0.5}CoO_3$. The solid lines through the data represent a numerical least-square refinement fit in the $R3C$ space group. The vertical bars below the diffractogram indicate the position of expected Bragg reflections and the solid lines at the bottom of graph is an intensity difference plot between the observed and the fitted diffraction patterns

Table 3.1 Refined structural parameters of $La_{0.5}Sr_{0.5}CoO_3$

System	Rhombohedral
Lattice parameters (A°)	a = 5.4294(2) c = 13.2353(6)
Cell Volume (A°)^3	337.88
Space group	$R3C$
La x y z Occpancy	0.0000 0.0000 0.2500 0.50
Sr x y z Occupancy	0.0000 0.0000 0.2500 0.50
Co x y z Occupancy	0.0000 0.0000 0.0000 1.0
O x y z Occupancy	0.5254(15) 0.0000 0.2500 3.0
R factors R_p R_{wp} χ^2 R_{Bragg} R_f	11.5 16.8 1.60 2.77 2.48

105

The XRD pattern of the $La_{1-x}Sr_xCoO_3$ powder for varying Sr^{2+} content is given in figure 3.2. The samples with Sr^{2+} content $0.1 \leq x \leq 0.5$ can be indexed to that of rhombohedral distorted perovskite structure; space group $R\bar{3}c$. But for Sr^{2+} content $x = 0.6$, the crystal structure of the sample is tetragonal.
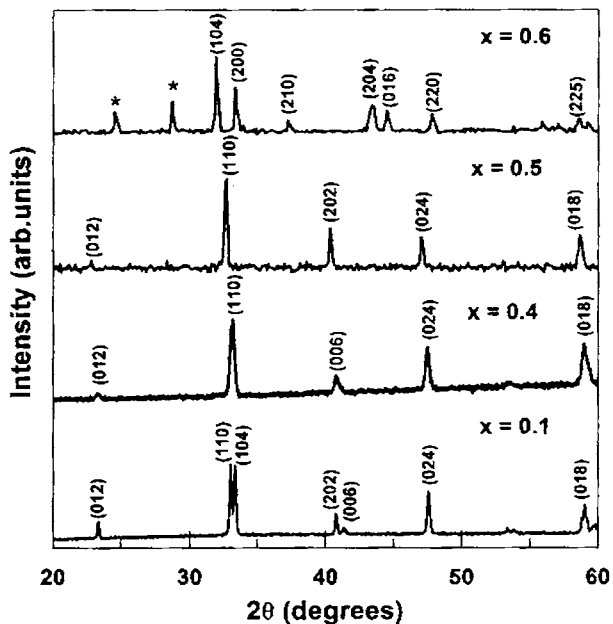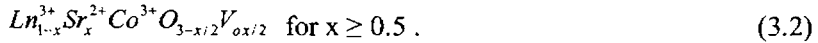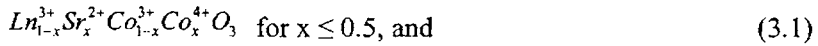

Figure 3.2.XRD pattern of the system $La_{1-x}Sr_xCoO_3$ for x = 0.1,0.4, 0.5 and 0.6. The * indicates unidentified peaks

The crystal structure of $La_{1-x}Sr_xCoO_3$ is derived from the ABO_3 perovskite $LaCoO_3$. The ideal crystal structure of perovskite type oxide ABO_3 have the large ionic-size lanthanide ion (A) occupying the body centered position, the small Co ion (B) occupying the corners of the cube and the oxygen ion (O) occupying the edge centers. $LaCoO_3$ is reported to show a small rhombohedral deviation from cubic form, with a = 3.82 A° and $\alpha = 90^{\circ}$ 42' [18]. Jonker and Van Santen has found that this distortion decreases with increasing Sr^{2+} content

and at about 50 % Sr^{2+} the XRD pattern no longer shows a splitting up of lines corresponding to rhombohedral distortion and the system is cubic [19]. When Sr^{2+} ion occupies La^{3+} site, the charge compensation is accomplished by either of the two mechanisms; the oxidation of Co^{3+} ion to Co^{4+} or the formation of O^{2-} vacancy V_o [20]. This can be expressed as

$$Ln_{1-x}^{3+}Sr_x^{2+}Co_{1-x}^{3+}Co_x^{4+}O_3 \quad \text{for } x \leq 0.5, \text{ and} \tag{3.1}$$

$$Ln_{1-x}^{3+}Sr_x^{2+}Co^{3+}O_{3-x/2}V_{ox/2} \quad \text{for } x \geq 0.5 . \tag{3.2}$$

The XRD results in our case give a rhombohedral distorted structure even for $x = 0.5$ which is similar to the one obtained for Vanita et.al [17]. This system may be considered as a fully oxygenated. A fully oxygenated $La_{1-x}Sr_xCoO_3$ ($x \leq 0.5$) system at room temperature belongs to the space group $R\bar{3}C$ [21]. When $x > 0.5$; the oxygen vacancy distorts the perovskite phase and results in the appearance of a phase with a lower coordination number for cobalt. This is probably the cause of the tetragonal structure for $x = 0.6$ [20].

The XRD pattern of the $La_{0.5}Sr_{0.5}Co_{1-x}Ni_xO_3$ system with varying Ni content is given in figure 3.3. For all Ni concentrations the system may be indexed to that of rhombohedral distorted perovskite structure; space group $R\bar{3}C$. The XRD pattern shows the presence of monoclinic $LaNiO_{2.5}$ (JCPDS card No: 87-1216) and orthorhombic $La_{1.6}Sr_{0.4}NiO_{3.5}$ (JCPDS card No: 85-2379) in addition to perovskite LSCNO (JCPDS card No: 87-1082) for all Ni content. All the d values of the LSCNO perovskite system was shifted by an amount of 0.04 A^0. This shift may be due to the incorporation of Ni atoms at Co sites in perovskite LSCO system [22].
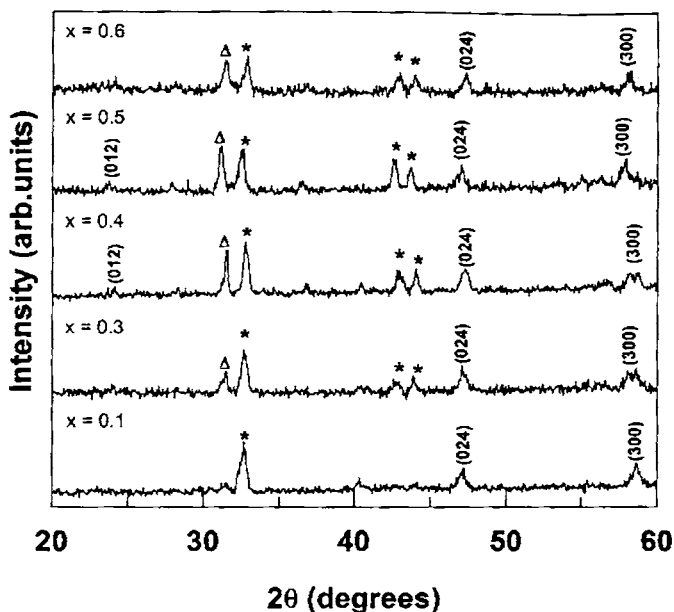
Figure 3.3.XRD pattern of the $La_{0.5}Sr_{0.5}Co_{1-x}Ni_xO_3$ system with varying Ni content. Δ and * indicate peak due to $LaNiO_{2.5}$ and $La_{1.6}Sr_{0.4}NiO_{3.5}$ respectively

3.3.2 Transport Properties

The transport properties of the LSCO and LSCNO compounds were studied by the resistivity, magnetoresistance (MR) and thermoelectric power measurements. The temperature dependent resistivity measurement revealed the conductivity mechanism in these compounds. The magnetic field response and the charge carrier responsible for conduction were studied using the MR and thermoelectric power measurements respectively.
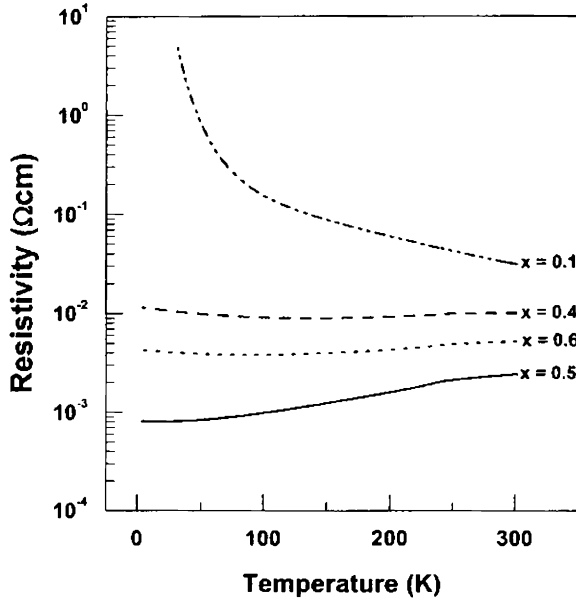
i) Resistivity Measurements

Figure 3.4. The temperature dependence of resistivity of the $La_{1-x}Sr_xCoO_3$ for $0.1 \leq x \leq 0.6$

The temperature dependence of resistivity of the $La_{1-x}Sr_xCoO_3$ $(0.1 \leq x \leq 0.6)$ is as shown in figure 3.4. For $x = 0.1$ a semiconductive behavior is observed. The resistivity of this sample follows the relation

$$\rho(T) = \rho_0 \exp[(T_0 / T)^n],\qquad (3.3)$$

where $\quad n = \dfrac{1}{2}\quad$ and $\quad T_0 = \dfrac{\beta}{kg(\mu)a^3},$

$g(\mu)$ is the density of states at the Fermi level, a the localization radius of the states near the Fermi level, and β a numerical constant. ρ_0 is generally of the

109

order of $\dfrac{1}{\sigma_{Mott}}$, where σ_{Mott} is the Mott minimum conductivity in these samples. The conductivity mechanism of this type is Efros-Shlovski (ES) type hopping, which is variable range hopping (VRH) in the presence of a Coulomb gap in the density of states. A plot of $\ln\rho(T)$ vs $T^{-1/2}$ gives a straight line (figure 3.5) at low temperature, which indicates the ES type hopping conduction mechanism for x = 0.1 sample [23]. A slope change is observed for the graph around 100 K. This may be attributed to the spin state transition of the system from a low spin to intermediate spin or high spin state [14, 24]. The argument is justified by the presence of an enhanced thermoelectric power for the x = 0.1 sample around 100 K (figure 3.14). The value of ρ_0 and T_0 for the region below 100 K is 15×10^{-3} Ωcm and 2015 K respectively, which are physically justifiable.
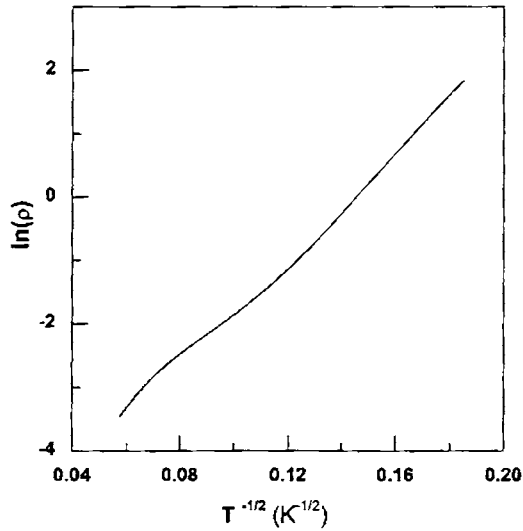

Figure 3.5. $\ln(\rho)$ versus $T^{-1/2}$ plot for the x = 0.1 composition of $La_{1-x}Sr_xCoO_3$ showing Efros-Shlovski (ES) type hopping

The thermally activated spin state transition and the corresponding variation in resistivity in the $La_{1-x}Sr_xCoO_3$ with x = 0.1 can be explained as follows. Sr^{2+} doping into the $La_{1-x}Sr_xCoO_3$ system creates tetravalent Co ions which are responsible for the ferromagnetism and semiconducting behavior of the system. The system have a cluster type behavior with ferromagnetic clusters containing tetravalent cobalt ions in the high spin (HS) (Co^{4+}) and low spin (LS) (Co^{IV}) state and a semiconducting intercluster medium containing trivalent cobalt ions in the HS (Co^{3+}) and LS (Co^{III}) state. It is the spin type of the trivalent cobalt ion in the intercluster medium which determines the charge transport through the cluster. The population of the HS and LS trivalent cobalt ion depends on temperature. For T < 100 K, most of the trivalent cobalt ions go to the low spin state. Therefore the trivalent cobalt ions residing at the boundaries between the ferromagnetic clusters localize the charge carriers causing a large increase in resistivity below 100 K. But as the temperature increases above 100 K, the trivalent cobalt ions become high spin and permit the charge transport through the cluster decreasing the resistivity.

For x > 0.1, the behavior of the resistivity in the temperature range indicates a metallic nature (figure 3.4). The value of resistivity is found to decrease with increase of Sr^{2+} content and the minimum resistivity was obtained for Sr^{2+} = 0.5. With further increase in Sr^{2+} content the resistivity was found to increase slightly as shown in the figure. The behavior is quite similar to the results reported earlier [14, 15]. The conductivity mechanism of $La_{1-x}Sr_xCoO_3$ can be explained using the same argument used to explain the structural evolution with Sr^{2+} doping. As the Sr^{2+} content increases, the Co^{4+} content also increases, which decreases the resistivity. When x is 0.5, the Co^{4+} content reaches its maximum and with further increase in Sr^{2+} content the structural phase transition occurs with the creation of oxygen vacancy and the resistivity increases. This explains the slight increase in resistivity for x = 0.6 [15, 20, 25].
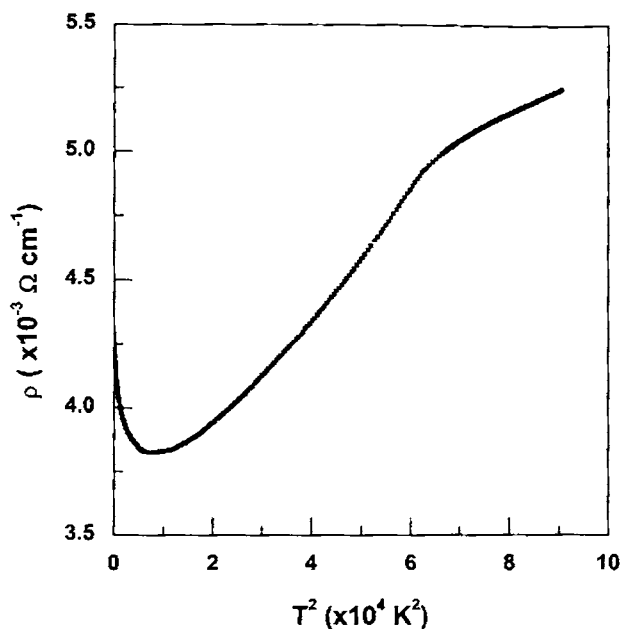
111

Figure 3.6. ρ versus T^2 plot for the x = 0.6 composition of $La_{1-x}Sr_xCoO_3$

A closer examination of the resistivity versus temperature plot of the metallic samples (see e.g. H = 0 curves in figure 3.8) shows an upturn in the resistivity behavior below 100 K. But the above explanation of the spin state transition of the Co ions cannot be used to explain this phenomenon. Since for $x \geq 0.2$, the concentration of the metallic ferromagnetic clusters is large enough and it exhibits itself as bulk ferromagnetism and the contribution to the conductivity from the trivalent Co ions residing at the intercluster medium is negligible [12, 14, 26]. Mandal et al. [27] has reported that the rise in resistivity for T < 100K can be due to the presence of oxygen vacancies. But the structural evaluation shows a fully oxygenated one for the compound ruling out this possibility. A similar rise in resistivity below 100 K was observed by Wu et al. [15] and it was attributed to the weak localization of charge carriers at low temperature. Ferromagnetic metals at low temperature are reported to have a T^2 dependence

112

on resistivity due to the electron scattering from the spin waves [28]. This behavior was investigated by plotting the resistivity as function of T^2 for $La_{0.4}Sr_{0.6}CoO_3$ (figure 3.6). It can be seen that the low temperature rise in the resistivity makes a deviation from the T^2 dependence. This rise in resistivity is due to the quantum interference effects and the resistivity in the region below 150 K follows the relation

$$\rho = \rho_0 - A\sqrt{T} + BT^2 .$$

(3.4)

It is the $\sqrt{T}$ dependence on resistivity which manifests as the upturn in the resistivity at low temperature. Metallic oxides with disorder usually show this type of behavior [29].
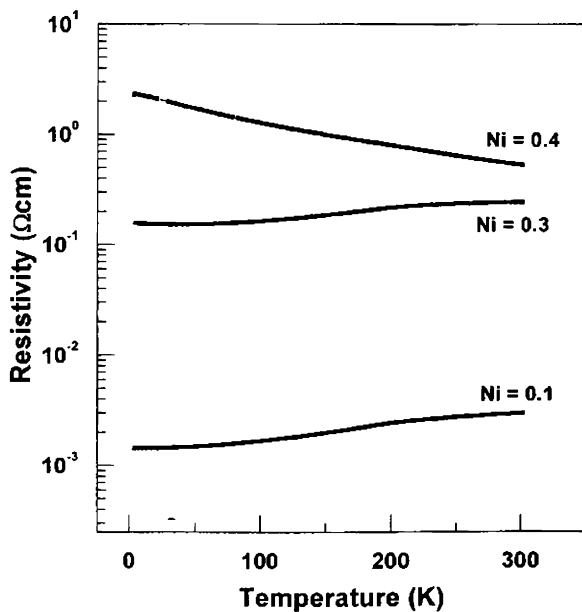

Figure 3.7. Variation of resistivity with temperature for the $La_{0.5}Sr_{0.5}Co_{1-x}Ni_xO_3$ for varying Ni^{3+} content

113

Figure 3.7 gives the variation of resistivity with temperature for the $La_{0.5}Sr_{0.5}Co_{1-x}Ni_xO_3$ system for varying Ni concentration. The samples with low Ni concentration, $0.1 \leq x \leq 0.3$ show a metallic behavior. The resistivity was found to increase with increase in Ni concentration. For Ni concentration $x = 0.4$ the sample is semiconducting and with further increase in Ni concentration the system became insulating. Migiakis et al. [30] has studied the effect of Sr^{2+} substitution on the transport properties of $LaNi_{0.2}Co_{0.8}O_3$ system. The obtained resistivity of the LSCNO system in the present study is comparable to reported results. The increase in resistivity with Ni substitution in LSCO can be explained as follows. The substitution of Ni was made by using NiO along with other constituent compounds for LSCO. NiO is an antiferromagnetic insulator. The electrical transport in LSCO through the direct contact through the grains is disturbed with the introduction of NiO. With increasing NiO concentration some part of the substituted NiO goes into the grains substituting the Co in the perovskite lattice and the remaining goes to the grain boundaries. If Ni substitutes Co in the perovskite lattice the double exchange mechanism involving Co^{3+} and Co^{4+} ions is disturbed as Ni cannot participate in it. Therefore with the increase of the NiO doping level the resistivity of the LSCNO system increases [22]. An upturn in the resistivity behavior below 50 K similar to that observed in the $La_{1-x}Sr_xCoO_3$ was also observed for the metallic samples in $La_{0.5}Sr_{0.5}Co_{1-x}Ni_xO_3$ due to quantum interference effects.

ii) Magnetoresistance measurements

The magneto transport of the $La_{1-x}Sr_xCoO_3$ and $La_{0.5}Sr_{0.5}Co_{1-x}Ni_xO_3$ was found to depend on the concentration of Sr^{2+} and Ni^{3+} respectively. The metallic composition of both the systems showed a small negative magnetoresistance (MR) like a typical ferromagnetic metal. But for the semiconducting composition of the $La_{1-x}Sr_xCoO_3$ system ($x = 0.1$) a large negative MR at very low temperature was observed. But the semiconducting composition in the

114

$La_{0.5}Sr_{0.5}Co_{1-x}Ni_xO_3$ system does not show any MR even at very low temperature. The MR behavior in the metallic region and semiconducting region of the system had different origin.
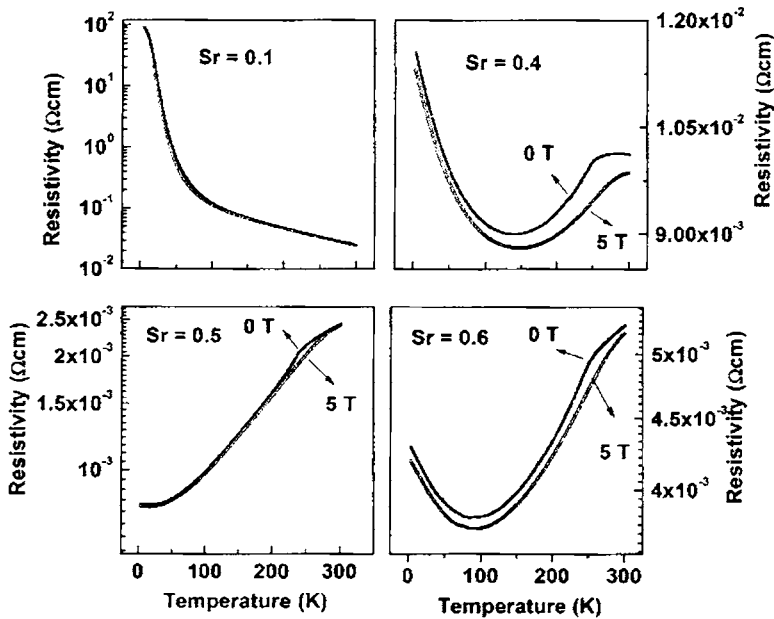
(a) Metallic samples

Figure 3.8. Temperature dependence of of resistivity in the presence of zero and 5 T magnetic field for $La_{1-x}Sr_xCoO_3$ (x = 0.1, 0.4, 0.5 and 0.6)

The variation of resistivity with temperature in zero field as well as in 5 T magnetic field $La_{1-x}Sr_xCoO_3$ system is given in figure 3.8. Figure 3.9 shows the temperature variation of MR at 5 T magnetic field which is calculated from resistivity curves shown in figure 3.8. The Y axis of figure 3.9 shows negative MR in percentage. The negative MR for the metallic compositions indicates it as a typical ferromagnetic metal [14, 15]. The value of MR is found to increase

with Sr^{2+} content and the maximum MR in metallic compositions was obtained for x = 0.5 which has lowest resistivity. There is a sharp decrease in resistivity below the ferromagnetic transition temperature T_c. For x = 0.4 and 0.6, MR is slightly lower and shows broad feature around transition temperature as compared to x = 0.5.
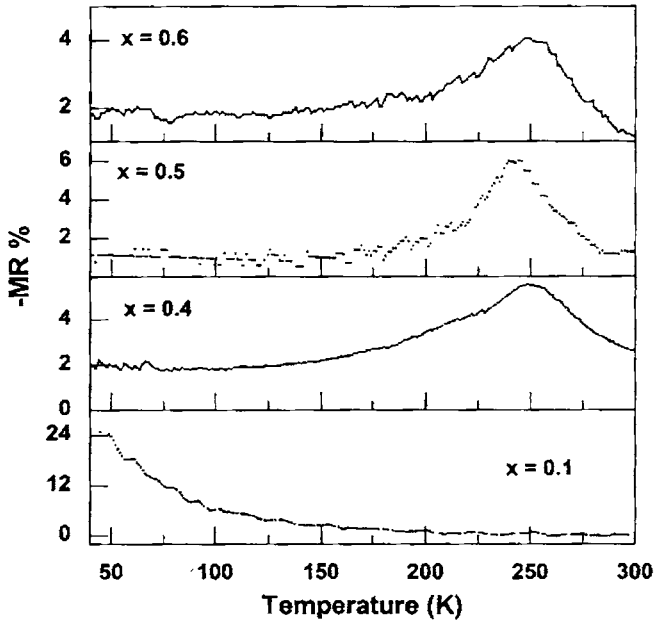

Figure 3.9. Variation of MR% with temperature for $La_{1-x}Sr_xCoO_3$ for varying Sr^{2+} content. The in field resistivity measurements were taken for a field of 5 T

In the Double exchange theory, the electron or the hole transfer between the neighboring sites depends on the relative angle $\Delta\theta_{ij}$ of the local t_{2g} spins [31], i.e.

$$t_{ij} = t_0 \cos\left(\frac{\Delta\theta_{ij}}{2}\right).$$
(3.5)

116

In the ferromagnetic state the spins are aligned parallel and spin transfer integral t_{ij} becomes maximum. Therefore the carrier mobility increases and the resistivity is reduced. The peak in the negative MR is observed around the T_c of the samples. The external magnetic field aligns the local spin moments of the sample. Maximum magnetization due to the alignment of the spin moments is obtained at the critical temperature of the ferromagnetic material [15, 31]. Therefore there is reduced carrier scattering round the T_c with magnetic field which causes maximum negative MR around T_c. The T_c of all the compositions was found to be close to 240 K. But there was no significant shift in the T_c with Sr^{2+} content.
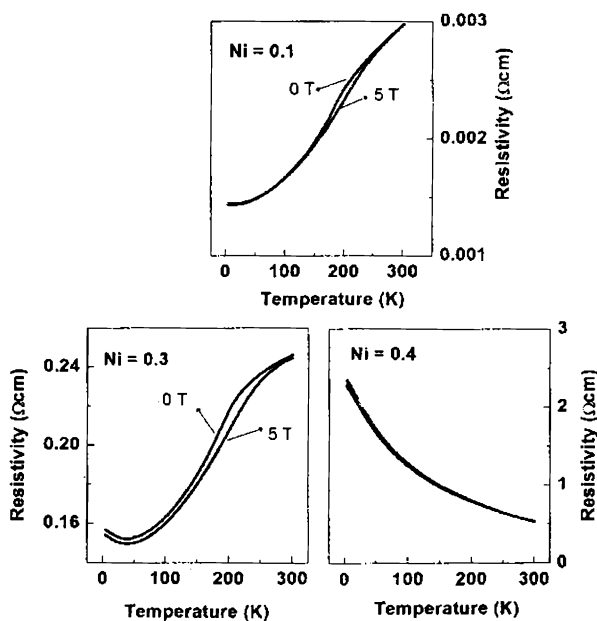

Figure 3.10. Variation of resistivity as a function of temperature for zero field and for a field of 5 T for $La_{0.5}Sr_{0.5}Co_{1-x}Ni_xO_3$ for varying Ni^{3+} content

117

For the $La_{0.5}Sr_{0.5}Co_{1-x}Ni_xO_3$ system the substitution of Ni^{3+} was found to enhance the resistivity of the system. Figure 3.10 gives the resistivity as a function of temperature for zero field and for a field of 5 T for $La_{0.5}Sr_{0.5}Co_{1-x}Ni_xO_3$ system and the variation of percentage of negative MR as a function of temperature at a field of 5 T is given in figure 3.11. The MR was observed only in the metallic composition of this system. The maximum negative MR was shown for the composition x = 0.3. With further increase of the Ni^{3+} content the system becomes semiconducting and the negative MR disappears. The peak of the negative MR was found close to the T_c of the system ie 200 K.
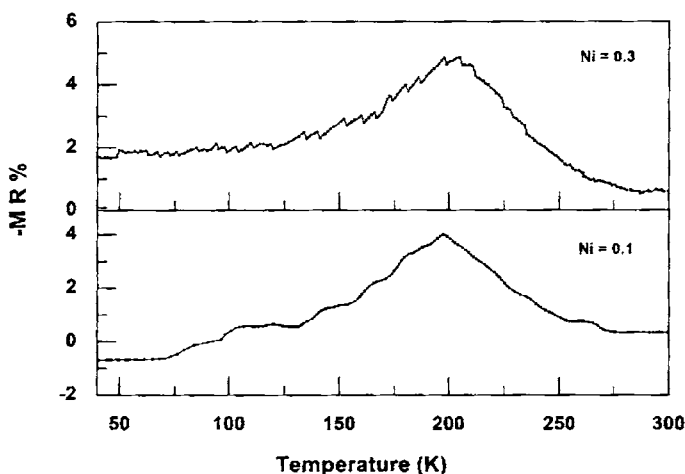

Figure 3.11. Variation of MR% with temperature for $La_{0.5}Sr_{0.5}Co_{1-x}Ni_xO_3$ for varying Ni^{3+} content. The in field resistivity measurements were taken for a field of 5 T

The variation of MR as a function of magnetic field at different temperatures for varying Sr^{2+} content for the $La_{1-x}Sr_xCoO_3$ (x = 0.4, 0.5, 0.6) is shown in figure 3.12. There was an increase in negative MR with increasing magnetic field for all the temperatures studied. In the ferromagnetic region the negative MR was found to increase more sharply with magnetic field. Generally magnitude of MR in ferromagnetic region shows rapid increase at low field which tends to saturate

118

at higher magnetic field. However, in the present case MR shows more or less liner trend at low temperatures. The variation in the MR at low temperature can be due to the inhomogeneous ferromagnetic state in these systems [14]. The maximum variation in MR was obtained at 250 K close to the transition temperature of the samples. In the paramagnetic region (above 250 K) the increase in negative MR was not very sharp where the MR increased to a very small value with the increase of magnetic field. The studies on the magnetization of $La_{1-x}Sr_xCoO_3$ indicate that the magnetization is proportional to magnetic field in the paramagnetic region. Therefore the MR can be considered to have negative a H^2 dependence on magnetic field. The magnetic field suppresses the spin fluctuation leading to negative H^2 dependence on magnetic field for the MR [32].

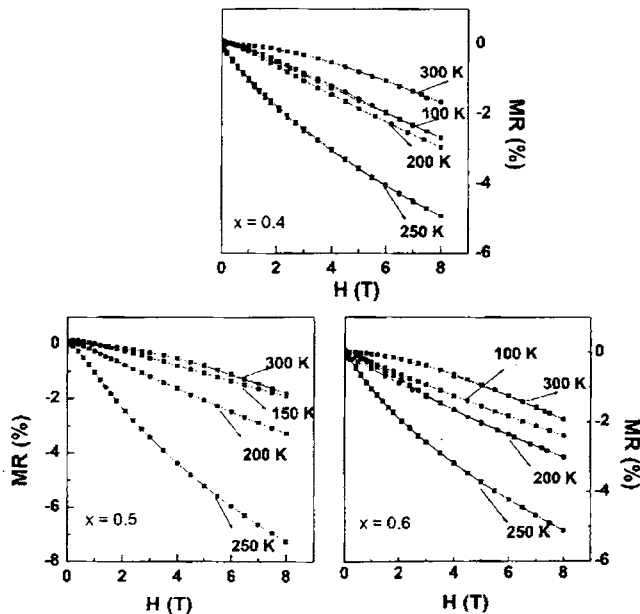**Figure 3.12.**MR as a function of magnetic field for the metallic compositions of $La_{1-x}Sr_xCoO_3$ at different temperatures

Figure 3.13 gives the plot of MR as a function of magnetic field for metallic samples (Ni = 0.1 and 0.3) of the series $La_{0.5}Sr_{0.5}Co_{1-x}Ni_xO_3$. The MR behavior is

similar to above metallic system. At 300 K MR follows negative H^2 dependence indicating paramagnetic state. This behavior is more evident than the $La_{1-x}Sr_xCoO_3$ samples and its transition temperature are close to 300 K as compared to Ni doped sample. Maximum MR was observed at 200 K which is close to T_c of the samples. At 150 K the MR is found to be complex showing small positive MR at low field which changes sign around 1.5 Tesla. This behavior is similar to $La_{0.5}Sr_{0.5}Co_3$ studied by Mahendiran et al. [14].

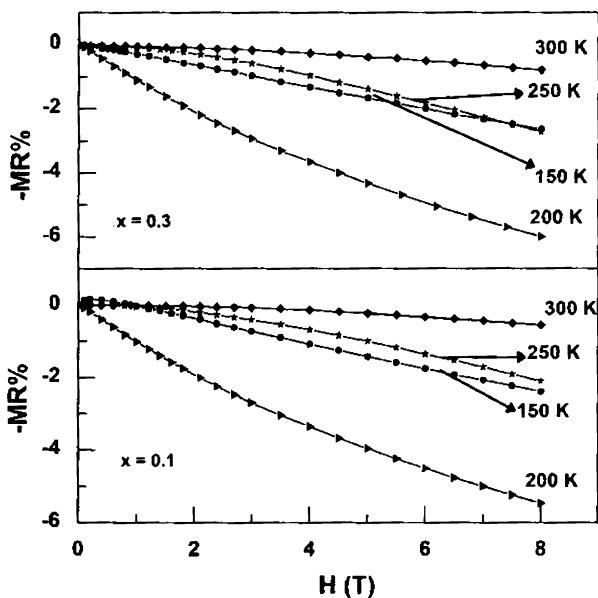**Figure 3.13.**MR as a function of magnetic field for the metallic compositions of $La_{0.5}Sr_{0.5}Co_{1-x}Ni_xO_3$ at different temperatures

(b) Semiconducting Samples

The figure 3.8 clearly indicates a semiconducting type conductive mechanism for the composition x = 0.1 of $La_{1-x}Sr_xCoO_3$ system over the whole temperature range studied. The onset of metallicity and ferromagnetism is simultaneous in $La_{1-x}Sr_xCoO_3$ system. According to the double exchange model the magnetoresistance can be observed around ferromagnetic transition temperature [33]. But figure 3.9 indicates a large negative MR (up to 25 %) at low temperature for the x = 0.1 composition which keeps on increasing with decreasing temperature. A similar effect of a large and negative MR in semiconducting compositions with the maximum MR near the spin-glass-like transition temperature was observed by Mahendiran et al. [14]. Wu et al. [15] obtained a low temperature MR value up to 35% for the Sr^{2+} content below x = 0.15. The observation of large negative MR in the compositions below the critical doping concentration (ie x < 0.15) is interesting. It is the Co^{3+} and Co^{4+} spins which make up the ferromagnetic clusters or the magnetic polarons in the cobaltite system. The spin fluctuations in the system are suppressed by the application of a large magnetic field at low temperature. This increases the hopping conductivity of the system contributing to large negative MR at very low temperatures. But the low temperature negative MR was not observed for the semiconducting composition of the $La_{0.5}Sr_{0.5}Co_{1-x}Ni_xO_3$ system. The Ni^{3+} substitution beyond x = 0.3 in the $La_{0.5}Sr_{0.5}Co_{1-x}Ni_xO_3$ system might have destroyed the inherent ferromagnetic ordering of the $La_{1-x}Sr_xCoO_3$ system.

The observed magnetotranport properties of the $La_{1-x}Sr_xCoO_3$ and $La_{0.5}Sr_{0.5}Co_{1-x}Ni_xO_3$ system can be explained as follows. Thermally activated spin state transition is a peculiar property of the cobaltite system. The comparable crystal field splitting energy and the Hund's rule exchange energy contributes to the spin state transitions in the t_{2g} and e_g states of the Co ion of the $La_{1-x}Sr_xCoO_3$ system [35]. In $LaCoO_3$, the Co ion is in the low-spin-state

121

(LS) Co^{III} (t_{2g}^6, S = 0) at low temperature. The energy difference between the LS and high spin (HS); Co^{3+} ($t_{2g}^4 e_g^2$, S = 2) is only 0.03 eV [26]. The large crystal field stabilizes the low spin state at low temperature. Thermal excitation can provide a spin transition from the LS to the intermediate spin; (IS: $t_{2g}^5 e_g^1$) around 100 K [26, 35]. Metal-Insulator transition is observed in the $LaCoO_3$ system with the spin state transition to high spin state above 500 K. Sr^{2+} substitution creates tetravalent Co ions which can take LS: Co^{IV} (t_{2g}^5, S = ½), IS Co^{+4} ($t_{2g}^4 e_g^1$,

S = 3/2) and high spin states Co^{+4} ($t_{2g}^3 e_g^2$, S = 5/2). The high spin Co^{4+} is 1 eV lower in energy than low spin Co^{IV}. Thus $La_{1-x}Sr_xCoO_3$ system contains a mixture of LS Co^{III} (t_{2g}^6), LS Co^{IV} (t_{2g}^5), IS Co^{3+} ($t_{2g}^5 e_g^1$), IS Co^{+4} ($t_{2g}^4 e_g^1$) and some HS Co^{3+} ($t_{2g}^4 e_g^2$) and HS Co^{4+} ($t_{2g}^3 e_g^2$) depending on the temperature and the Sr^{2+} content [14]. Another important property of the $La_{1-x}Sr_xCoO_3$ system is the short range magnetic ordering or the spin glass state for low Sr^{2+} doping. With higher Sr^{2+} content the system evolves to a state of long range ferromagnetic ordering [15].

We have interpreted our results considering a cluster model for the system. The exchange interactions between ions with the same valency state are antiferromagnetic. For low Sr^{2+} content the Co ion is mostly in the trivalent state and hence the system is dominated by an antiferromagnetic interaction between the trivalent Co ions. As the Sr^{2+} content increases the fraction of the Co^{4+} state increases. The exchange interaction of the tetravalent Co ion with the high spin trivalent Co ion is ferromagnetic. Therefore with the increase of the Sr^{2+} content the system phase separates into ferromagnetically interacting hole-rich clusters in an antiferromagnetically correlated matrix. The onset of ferromagnetic transition takes place at the critical temperature T_c. But the ferromagnetic phase does not have a long range order as the cluster of ferromagnetic regions is

embedded in antiferromagnetic matrix [34, 14]. The application of the magnetic field causes a local spin ordering and reduces the resistivity of the system leading to negative MR. This effect is more prominent near the ferromagnetic transition temperature T_c of the system as the field induced magnetization is more near T_c. At $x = 0.5$ the Co^{4+} content is maximum which maximizes the strength of the double exchange causing maximum MR [15]. This explains the observed negative MR for the metallic composition of $La_{1-x}Sr_xCoO_3$. In $La_{0.5}Sr_{0.5}Co_{1-x}Ni_xO_3$ the low doping of the Ni^{3+} does not interrupt the ferromagnetic ordering of the $La_{1-x}Sr_xCoO_3$ system. Therefore the local spin alignment due to the applied magnetic field can be considered as the reason for the negative MR in the metallic composition of $La_{0.5}Sr_{0.5}Co_{1-x}Ni_xO_3$. But the maximum negative MR in this system was not observed for the most metallic composition. This can be due to the increased scattering effect of the charge carries which compensates the local ordering due to magnetic field. The new phase separation model can be used to interpret the large MR observed in the semiconducting composition of the $La_{1-x}Sr_xCoO_3$. According to this model the ferromagnetic grains are embedded in antiferromagnetic matrix. The ferromagnetic phase is metallic with low resistivity where as the antiferromagnetic phase is insulating with high resistivity. With the application of magnetic field aniferromagnetic phase can be converted into ferromagnetic phase causing large magnetoresistance. This phenomenon is more evident near the percolation limit where the application of the magnetic field leads to colossal magnetoresistance as the ferromagnetic clusters form a percolative path [35, 36]. But in the semiconducting compositions of $La_{0.5}Sr_{0.5}Co_{1-x}Ni_xO_3$ the higher Ni^{3+} content disrupts the inherent ferromagnetic ordering of the $La_{1-x}Sr_xCoO_3$ causing no MR even at very low temperatures [22].

iii) Thermoelectric power measurements

Thermoelectric power is a zero current transport coefficient which can probe intrinsic properties of the material without being affected by defects such as grain boundaries. Thermoelectric power can be used to clarify the electronic structure as it is sensitive to the band structure and carrier mobility near the Fermi level [38, 39].
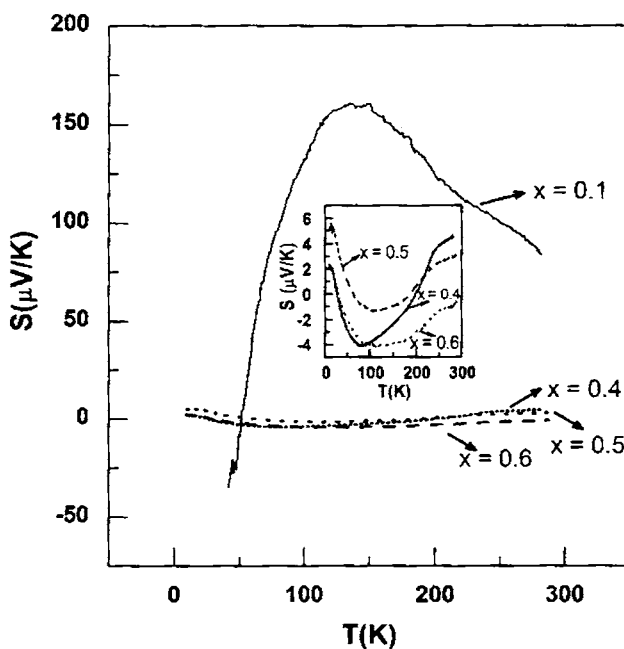
Figure 3.14. Variation of thermoelectric power with temperature for varying Sr^{2+} content for $La_{1-x}Sr_xCoO_3$

Figure 3.14 shows the variation of thermoelectric power (S(T)) with temperature for $La_{1-x}Sr_xCoO_3$ for varying Sr^{2+} content. The variation of S(T) with temperature for $La_{1-x}Sr_xCoO_3$ with x = 0.1 is quite different from that of samples with higher values of x. For x = 0.1 the S(T) increases with temperature to very

124

high value of 160 $\mu V/K$ at a temperature of 130 K. It remains at this value up to a temperature of about 150 K and thereafter decreases smoothly with temperature. The behavior is quite similar to that observed by Senaris-Rodriguez et al. [12]. For the compositional range $0 < x \le 0.05$ an increase in thermopower to a very high value was observed, and a plateau was defined with two critical temperatures T_s and T_s', in the S(T) versus temperature curve. But the plateau region is not well defined in the present case. The plateau region in the S(T) versus temperature curve is caused by an electrical conduction dominated by small polaron holes of nearly constant concentration [12].

The high value of thermo electric coefficient for $x = 0.1$ can be explained considering the spin states of the Co ions in the system. In $La_{1-x}Sr_xCoO_3$ the crystal field splitting energy and the Hunds rule exchange energy of the Co d states are comparable. Therefore the system can undergo thermally activated spin state transitions. In $LaCoO_3$, the trivalent Co ion is in the low-spin-state (LS) Co^{III} (t_{2g}^6, S = 0) at low temperature. It can undergo a spin state transition to an intermediate spin state (IS) (Co^{3+}: $t_{2g}^5 e_g^1$) at 100 K and to a high spin state Co^{3+} ($t_{2g}^4 e_g^2$, S = 2) above 500 K. Sr^{2+} substitution creates tetravalent Co ion which can exist in LS: Co^{IV} (t_{2g}^5, S = ½), IS Co^{+4} ($t_{2g}^4 e_g^1$, S = 3/2) and HS Co^{+4} ($t_{2g}^3 e_g^2$, S = 5/2) states. The Co ion in $La_{1-x}Sr_xCoO_3$ with $x = 0.1$ at a temperature around 100 K can be considered to have the identical spin configuration as the parent compound $LaCoO_3$. As the energy difference between the low spin and the intermediate spin states of the trivalent Co ion is only 100 K the system become degenerate at 100 K. This strong degeneracy causes an enhanced thermo power close to 100 K for the $x = 0.1$ system.

Also according to the generalised Heike's formula, the thermoelectric power is given by

$$S = -\frac{k_B}{e}\ln\left(\frac{g_3}{g_4}\frac{x}{1-x}\right) \qquad (3.6)$$

where g_3 and g_4 denote the number of configuration of Co^{3+} and Co^{4+} ions and x is the Sr^{2+} content [40, 24]. Therefore the ratio of the number of configuration of the Co ions is also crucial in determining thermopower. Koshibae et al. [24] has used the above relation to find out the thermoelectric power of the Co oxides. The calculations show that not only the degeneracy of the Co ion but also the ratio between the spin states of the Co ion ie g_3/g_4 is crucial in determining the thermopower of cobalt oxides. The maximum thermopower was obtained for the cobalt oxides when the trivalent Co ion was in the LS state and the tetravalent Co ion was in either LS or in a combination of LS and HS states even though there were other spin configurations for the system which were degenerate. Therefore in $La_{1-x}Sr_xCoO_3$ with x = 0.1 beyond 150 K, the spin configuration of the Co ions changes which changes the g_3/g_4 ratio of the system leading to a decrease in thermopower [24, 26].

The inset of the figure 3.14 shows the variation of S (T) versus temperature for higher Sr^{2+} content. The value of S (T) for x > 0.1 is very low and it has negative values within the ferromagnetic temperature domain. At higher temperatures it rises to small positive values. The figure shows a bend in the curve at T ~ T_c and this bend was found to shift towards the high temperature side with the increase of x. It exhibits a minimum with negative value around 100 K and rises to small positive values at room temperature indicating a metallic behavior. But for x = 0.6 the S (T) values remained to be negative over the whole temperature range even though it increased beyond the negative peak around 100 K. This negative value of S (T) may be due to the large FM clusters in the sample. The magnitude of S (T) at room temperature was found to decrease monotonically with increasing Sr^{2+} content. The low value of the thermoelectric power for the $La_{1-x}Sr_xCoO_3$ with large Sr^{2+} content can also be explained using the Heikes

formula. The spin state of the Co ions changes with increasing Sr^{2+} content and temperature. This changes the g_3/g_4 ratio of the system leading to low thermoelectric power. Even the sign of the thermoelectric power was found to depend on the g_3/g_4 ratio which explains the small negative values of thermoelectric power for the system in the ferromagnetic region. The presence of large ferromagnetic clusters can also contribute to the negative thermoelectric power of the system.
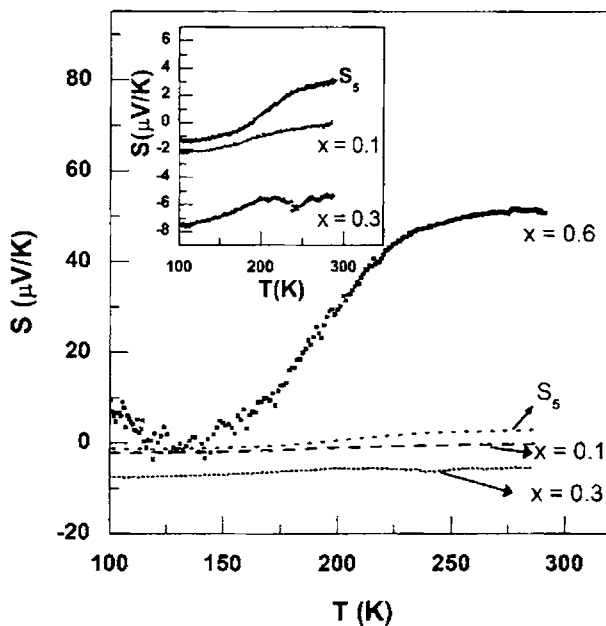
Figure 3.15. Variation of thermoelectric power with temperature for varying Ni^{3+} content for $La_{0.5}Sr_{0.5}Co_{1-x}Ni_xO_3$ in comparison with $La_{0.5}Sr_{0.5}CoO_3$ (S_5 in the figure)

Figure 3.15 shows the variation of thermoelectric power with temperature for varying Ni concentration for $La_{0.5}Sr_{0.5}Co_{1-x}Ni_xO_3$ in comparison with the thermoelectric power of $La_{0.5}Sr_{0.5}CoO_3$ (S_5 in the figure). The XRD analyses of

the $La_{0.5}Sr_{0.5}Co_{1-x}Ni_xO_3$ samples have shown the presence of some impurity phases in addition to perovskite $La_{0.5}Sr_{0.5}Co_{1-x}Ni_xO_3$. Fairly high purity of the samples is particularly important for thermo power determination at low temperatures [41]. Therefore the thermoelectric power data of Ni doped samples is considered from 100 K onwards only. For small values of Ni content; Ni = 0.1, the variation is similar to that of $La_{1-x}Sr_xCoO_3$ with x > 0.1. It has negative values within ferromagnetic temperature domain and rises to very small positive value at higher temperatures. This negative value for the most conductive sample in the $La_{0.5}Sr_{0.5}Co_{1-x}Ni_xO_3$ system is due to the scattering phenomena which dominate in the system. The reduced negative MR for this particular system further justifies this argument. For x = 0.3 sample the value of S(T) remained negative over the whole temperature range. This can be due to the large ferromagnetic clusters in the sample as the system showed largest negative MR among the compositions studied. For highly Ni doped sample; Ni = 0.5 and 0.6, the S(T) was found to steadily increase with temperature and raised to high value of S(T) indicating an insulating behavior. The temperature dependence of resistivity of highly Ni doped samples also indicated an insulating behavior. Thus the variation of S(T) with temperature for Ni doped samples clearly indicated a metallic behavior for light Ni concentration between $0.1 \leq x \leq 0.4$ and an insulating behavior for $x \geq 0.5$.

3.4. Conclusion

$La_{1-x}Sr_xCoO_3$ and $La_{0.5}Sr_{0.5}Co_{1-x}Ni_xO_3$ were prepared by solid state reaction. $La_{1-x}Sr_xCoO_3$ prepared for varying Sr^{2+} content were all single phase. The system could be indexed to rhombohedral distorted perovskite structure with space group $\bar{R}3C$ for all except x = 0.6, which had a tetragonal structure. $La_{0.5}Sr_{0.5}Co_{1-x}Ni_xO_3$ had some impurity phase in addition to perovskite $La_{0.5}Sr_{0.5}Co_{1-x}Ni_xO_3$. The temperature dependent resistivity data of the $La_{1-x}Sr_xCoO_3$ indicated a metallic conductivity for x > 0.1 and for x = 0.1 the system was semiconducting. The resistivity was found to decrease with Sr^{2+}

content with the x = 0.5 having the lowest resistivity. The temperature dependant resistivity of the $La_{0.5}Sr_{0.5}Co_{1-x}Ni_xO_3$ system indicated a metallic behavior for lightly doped samples (x $\leq$ 0.3). The sample with x = 0.4 was semiconducting and with further increase in Ni^{3+} the system became insulating. The MR of the $La_{1-x}Sr_xCoO_3$ indicated a negative MR for the metallic samples with the peak near the critical temperature. The most metallic system (x = 0.5) had the maximum MR. For the semiconducting composition x = 0.1 the MR behavior was different from that of metallic samples and gave a large negative MR at low temperature. In $La_{0.5}Sr_{0.5}Co_{1-x}Ni_xO_3$ only the metallic compositions showed the negative MR and the maximum MR was obtained for x = 0.3. The thermoelectric power measurements of the $La_{1-x}Sr_xCoO_3$ system gave a large thermo power for the insulating sample (x = 0.1) due to the degeneracy of the trivalent and tetravalent Co ions in the system. For metallic compositions the thermoelectric power increased with temperature to a small positive value like a typical ferromagnetic metal. For $La_{0.5}Sr_{0.5}Co_{1-x}Ni_xO_3$ system the conducting samples (x $\leq$ 0.3) gave negative value for the thermoelectric power within the ferromagnetic temperature domain and rose to small positive values at room temperature. The thermoelectric power of the insulating samples of the $La_{0.5}Sr_{0.5}Co_{1-x}Ni_xO_3$ system rose to high positive values with temperature as in $La_{1-x}Sr_xCoO_3$ system.

-

References

1. S.Kaji, N.Sakamoto, Solid State Ionics. **108**(1998)235
2. H.J.M.Bouwmerster, H.Kruidhof, A.J.Burggaf, Solid State Ionics. **72**(1994)185
3. K.Tabata, I.Matsumoto, J.Mater.Sci. **22**(1987)1882
4. Y.Ohno, S.Nagata, H.Sato, Solid State Ionics. **3/4**(1981)439
5. Z.L.Wang, J.Zhang, Phys.Rev.B. **54**(1996)1153
6. R.Ramesh, H-Gilchrist, T.Sands, V.G.Keramidas, R.Haakenaasen, D.K.Fork, Appl.Phys.Lett. **63**(1993)3592
7. J.T.Cheung, P.E.D.Morgan, D.H.Lowndes, S-Y.Zheng, J.Breen, Appl.Phys.Lett. **62**(1993)2045
8. N.Lehisa, K.Fukaya, K.Matsuo, N.Horiuchi, N.Karube, J.Appl.Phys. **59**(1986)317
9. J.Androulakis, P.Migiakis, J.Giapintzakis, Appl.Phys.Lett. **84**(2004)1099
10. R.W.Schwartz, M.T.Sebastian, M.V.Raymond, Mater.Res.Soc.Symp.Proc. **623**(2000)365
11. C.M.Chiu,Y.H.Chang, Sens.Actuators B. **54**(1999)236
12. M.A.Senaris-Rodriguez, J.B.Goodenough, J.Solid.State.Chem. **118**(1995)323
13. A.N.Petrov, O.F.Kononchuk, A.V.Andreev, V.A.Cherepanov, P.Kofstad, Solid State Ionics. **80**(1995)189
14. R.Mahendiran, A.K.Raychaudhuri, Phys.Rev.B. **54**(1996)16044
15. J.Wu, C.Leighton, Phys.Rev.B. **67**(2003)174408
16. A.J.Zhou, T.J.Zhu, X.B.Zhao, Mater.Sci.Engg.B. **128**(2006)174
17. P.V.Vanitha, A.Arulraj, P.N.Santhosh, C.N.R.Rao, Chem.Mater. **12**(2000)1666
18. H.Ohbayashi, T.Kudo, T.Gejo, Jpn.J.Appl.Phys. **13**(1974)1
19. G.H.Jonker, J.H.Van Santen, Physica. **19**(1953)120

20. J.Liu, L.He, G.Chen, W.Su, J.Mater.Sci. **32**(1997)203

21. R.H.E.van.Doorn, A.J.Burggraaf, Solid State Ionics. **128**(2000)65

22. M.Eshraghi, H.Salamati, P.Kameli, J.Alloys and Compounds. **437**(2007)22

23. B.I.Shlovskii, A.L.Efros, *Electronic Properties of Doped Semiconductors*, Springer-Verlag, Berlin, 1984, pp. 209

24. W.Koshibae, K.Tsutsui, S.Maekawa, Phys.Rev.B. **62**(2000)6869

25. P.Ganguly, P.S.Anilkumar, P.N.Santhosh, I.S.Mulla, J.Phys.Condens.Matter. **6**(1994)533

26. X.Xu, L.Jiang, J.Shen, Z.Chen, Z.Xu, Phys.Lett.A. **351**(2006)431

27. P.Mandal, A.Hassen, P.Choudhary, J.Appl.Pys. **100**(2006)103912

28. R.Mahendiran, A.K.Raychaudhuri, A.Chainani,, D.D.Sharma, J.Phys.Condens.Matter. **7**(1995)L561

29. A.K.Raychaudhuri, K.P.Rajeev, H.Srikanth, R.Mahendiran, Physica B. **197**(1994)124

30. P.Migiakis, J.Androulakis, J.Giapintzakis, J.Appl.Phys. **94**(2003)7616

31. S.Yamaguchi, H.Taniguchi, H.Takagi, T.Arima, Y.Tokura, J.Phys.Soc.Jpn. **64**(1995)1885

32. R.Rawant, I.Das, J.Phys.Condens.Matter. **13**(2001)L379

33. S.Mukherjee, R.Ranganathan, P.S.Anilkumar, P.A.Joy, Phys.Rev.B. **54**(1996)9267

34. V.G.Bhide, D.S.Rajoria, C.N.R.Rao, G.Rama.Rao, V.G.Jadhao, Phys.Rev.B. **12**(1975)2832

35. E.Dagotto, T.Hotta, A.Moreo, Physics Reports. **344**(2001)1

36. Y.Tokura, Rep.Prog.Phys. **69**(2006)797

37. J.B.Goodenough, Mater.Res.Bull. **6**(1971)967

38. A.Aslam, S.K.Hasanain, M.Zubair, M.J.Akhtar, M.Nadeem, J.Phys.Condes.Matter. **14**(2002)10305

39. A.S.Karolik, J.Phys.Condens.Matter. **13**(2001)1093

40. R.R.Heikes, R.W.Ure, Jr, *Thermoelectricity : Science and Engineering.* Interscience Publishers, New York- London, 1961. pp.170

131

41. P.Mandal, Phys.Rev.B. **61**(2000)1465

-

CHAPTER 4

Preparation and Characterization of $La_{0.5}Sr_{0.5}CoO_3$ thin films

La$_{0.5}$Sr$_{0.5}$CoO$_3$ thin films were prepared by rf magnetron sputtering. The various deposition parameters such as rf power, sputtering gas pressure, Ar:O$_2$ ratio in the sputtering gas and substrate temperature were optimized to obtain conducting and crystalline thin films. The oxygen atmosphere and the annealing temperature were found to be crucial in determining the conductivity of the thin films. But the oxygen incorporation during sputtering was found to deteriorate the film properties and the films prepared with minimum oxygen partial pressure was single phase with minimum resistivity. Crystalline and conducting La$_{0.5}$Sr$_{0.5}$CoO$_3$ thin films were obtained at substrate temperature as low as 500 °C.

4.1 Introduction

Oxide thin films have a wide range of properties covering insulators to high temperature superconductors and from ferroelectric to ferromagnetic materials. The growth of oxide thin films is an active field of research [1, 2]. Perovskite conducting oxide $La_{0.5}Sr_{0.5}CoO_3$ (LSCO) is obtained from ABO_3 perovskite $LaCoO_3$ by partial substitution of La^{3+} by Sr^{2+} [3, 4]. The similar crystal structure of LSCO with that of the perovskite ferroelectrics makes it a potential candidate as electrode for ferroelectric memory devices. The LSCO which is a conductive oxide electrode act as oxygen vacancy sink of the PZT capacitors thereby reducing the fatigue problem usually encountered while using conventional electrode Pt [5-8]. The similar crystal structure of LSCO and perovskite ferroelectrics facilitates the easy growth of ferroelectrics over textured or epitaxially grown LSCO layer [9, 10]. The high catalytic activity of LSCO to oxygen reduction and oxidation is widely applied in solid oxide fuel cells, oxygen separation membranes, cathodes for CO_2 lasers and gas sensors at elevated temperatures [11-14]. The good chemical and phase stability, large electrical conductivity and Seeback coefficient and the resistance to oxidation makes LSCO a possible candidate for thin film thermocouple applications [15].

This chapter describes the growth and characterization of $La_{0.5}Sr_{0.5}CoO_3$ (LSCO) thin films. The LSCO thin films were prepared by rf magnetron sputtering. The rf power, sputtering gas pressure, substrate temperature and $Ar:O_2$ sputter gas ratio has been optimized to get better conducting and crystalline perovskite thin films. Crystalline LSCO thin films could be grown at a substrate temperature of 500 °C. Also conducting LSCO thin films could be grown at room temperature by oxygen incorporation. The room temperature growth of conducting LSCO thin films facilitates the easy growth of top electrode for ferroelectric memory devices.

4.2 Experimental details

LSCO thin films were prepared by rf magnetron sputtering of the synthesized LSCO powder target. The method of preparation of LSCO powder is described in the section 3.2 of chapter 3. The powder was packed on to a copper plate of 2-inch diameter and the powder LSCO of thickness 2 mm was used as the target for sputtering.

The deposition was first carried out at various rf powers to optimize the rf power. The films were all deposited at room temperature for duration of one hour. High purity Argon gas was admitted into the chamber after attaining high vacuum (3×10^{-6} mbar). The Ar flow was adjusted using a mass flow controller and the deposition was carried out at an argon pressure of 0.001 mbar. The as deposited thin films were subjected to post deposition annealing in air and oxygen. The room temperature deposition of LSCO thin films on quartz and p-type Si <100> substrates were then carried out varying the Ar pressure and Ar:O_2 sputter gas ratio. The Ar pressure and Ar:O_2 sputter gas ratio was optimized to get conducting LSCO thin films at room temperature. Quartz, p-type Si <100> and Pt/TiO_2/SiO_2/Si were used as the substrates for the preparation of LSCO thin films at substrate temperature. The conditions such as sputtering gas pressure, substrate temperature and oxygen partial pressure were varied to optimize the growth of crystalline and conducting LSCO thin films.

The thickness of the films were found using Stylus profiler (Dektak 6M). The structural characterizations were carried out using a Rigaku X-ray diffractometer with Cu K_α radiation ($\lambda = 1.5418$ A^0). The room temperature electrical properties of the films were studied using a Keithley Source Measure Unit (SMU 236). The electrical conductivity and its temperature dependence were measured by Vanderpauw four probe method. Atomic force microscope was used to study the surface morphology and film roughness.

4.3 Results and Discussion

The growth of LSCO thin films is described in the following two sections viz. (1) room temperature deposition and (2) deposition at higher substrate temperature. The room temperature deposition includes the study of (i) influence of rf power and post deposition annealing condition and (ii) influence of Ar pressure and Ar:O_2 sputter gas ratio. The influence of sputtering gas pressure and Ar:O_2 sputter gas ratio was then studied by varying the substrate temperature.

4.3.1 Deposition at Room temperature

(a) Influence of rf power and post deposition annealing conditions

The LSCO thin films were deposited at various rf powers. Fused silica was used as the substrates. The substrate was kept at a distance of 4 cm above the target. The deposition was carried out at an argon pressure of 0.001 mbar for duration of one hour at a target to substrate distance of 6 cm. The thickness of the films was found to increase from 200 nm to 500 nm with rf power. The as deposited thin films were subjected to post deposition annealing in air and oxygen. The annealing was done at various temperatures (500 °C to 650 °C) in air and oxygen to optimize the crystallization temperature of LSCO thin films.

(i) Structural Properties

Figure 4.1 shows the XRD pattern of the LSCO powder target and the as deposited thin films deposited at rf power of 100 W and 150 W. The XRD patterns can be indexed to that of rhombohedral distorted perovskite structure, space group $R3C$, which is a fully oxygenated system [16]. The films deposited at lower rf powers were amorphous in nature. While the films deposited at

139

100 W and 150 W were oriented along (110) direction. Generally, sputtered particles have kinetic energies of several electron volts. This kinetic energy enhances the surface migration of sputtered particles arriving at the substrate surface and the crystallinity of the films is greatly affected by them. Thus it is possible to deposit crystalline films even at room temperature by sputtering using higher rf power [17, 18]
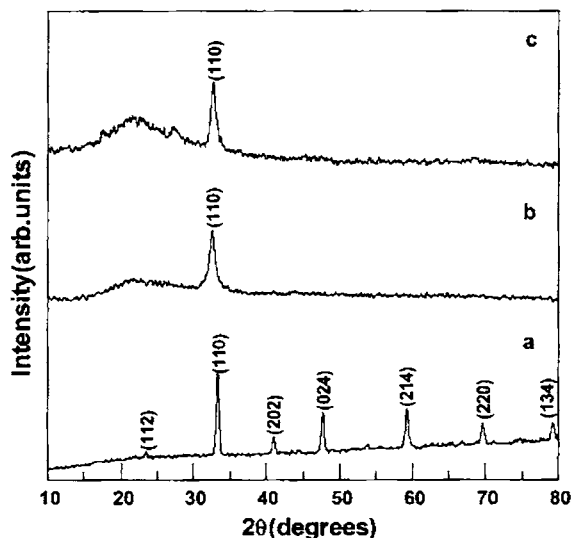

Figure 4.1 XRD pattern of $La_{0.5}Sr_{0.5}CoO_3$ (a) powder target and as deposited thin films deposited at rf powers (b) 100 W, (c) 150 W

The structural properties of the as deposited thin films subjected to post deposition annealing was investigated. It was observed that no perovskite phase was formed for the films annealed in air at 500 °C. The growth temperature of the $La_{0.5}Sr_{0.5}CoO_3$ thin films is reported to be greater than 600 °C, which explain the absence of perovskite phase for the films annealed in air at 500 °C [6]. Interestingly it was observed that the perovskite phase formation starts when the amorphous films were annealed at 500 °C in oxygen atmosphere (figure 4.2).

The films were all crystalline with the main peak oriented along (110) direction. The presence of oxygen during annealing might have contributed to the perovskite phase formation. The LSCO thin films were found to be crystalline irrespective of the annealing atmosphere when it was subjected to post deposition annealing at 600 °C and 650 °C. The crystallinity of the thin film was found to steadily increase with the increase in annealing temperature.
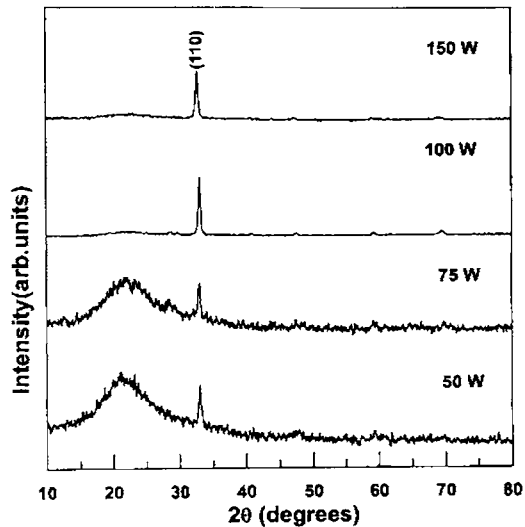
Figure 4.2 XRD pattern of $La_{0.5}Sr_{0.5}CoO_3$ thin films deposited at various rf powers and then annealed in oxygen at 500 °C

(ii) Electrical Properties

Figure 4.3 (a) shows the variation of resistivity with rf power for as deposited films and the films annealed in oxygen at 600 °C. The resistivity of the as prepared films was found to increase with rf power. The increase in resistivity with rf power may be due to the oxygen vacancies created in the film while depositing at higher rf power [19]. The ad atoms will have higher energy while

141

depositing at higher powers, which make them oxygen deficient [20]. When the films were annealed in oxygen at 600 °C, the film deposited at rf power of 150 W showed a low resistivity of 10^{-2} Ωcm. The decrease in resistivity for the films annealed in oxygen at 600 °C is due to the oxygen incorporation into the film at this temperature [21]. It has been reported that a similar effect as Sr^{2+} doping ie an increase in conductivity may be achieved by oxygen incorporation into LSCO thin films [22]. This explains the decrease in resistivity for the films annealed in oxygen at 600 °C. This result is further justified by the increase in band gap for thin films, which is due to the increase in carrier concentration [23].The resistivity was found to increase with rf power for the LSCO thin films post annealed at 650 °C as shown in figure 4.3(b). Annealing at high temperature creates oxygen vacancy, which reduces the conductivity considerably [22, 24].
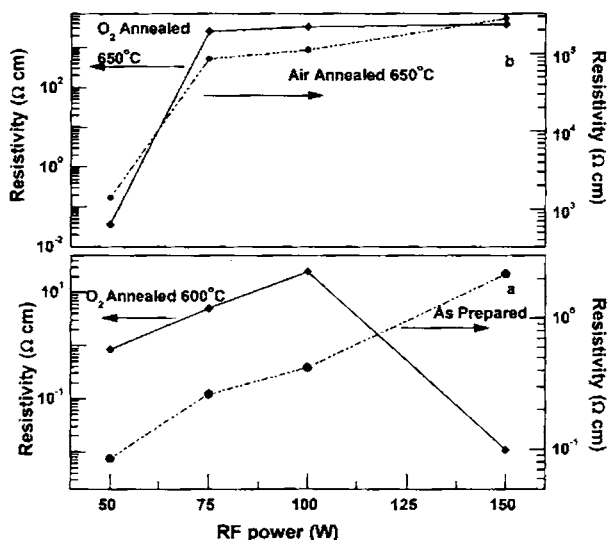

Figure 4.3 Variation of resistivity of LSCO thin films with rf power (a) as deposited films and films annealed in oxygen at 600 °C (b) films annealed in oxygen and air at 650 °C

142

(iii) Optical Properties

The optical properties of the films were studied by recording the transmission spectra in the UV-VIS-NIR region. A typical plot of transmission spectrum of $La_{0.5}Sr_{0.5}CoO_3$ is given in figure 4.4. The inset shows the plot of $(\alpha h\nu)^2$ vs $h\nu$ for determining the band gap of the material.

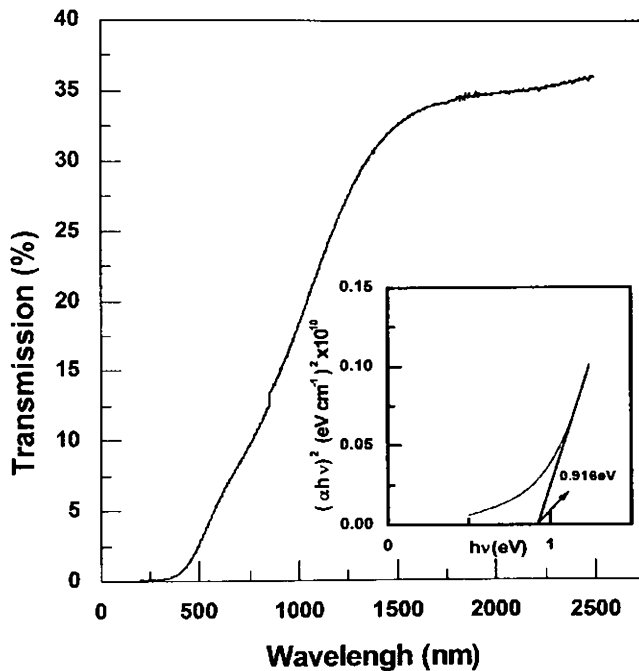**Figure 4.4** Typical transmission spectrum of as deposited $La_{0.5}Sr_{0.5}CoO_3$ thin film (rf power 50 W). Inset shows the $(\alpha h\nu)^2$ vs $h\nu$ plot

The band gaps of the as deposited thin films were found to decrease with increase in rf power. The variation of band gap and resistivity with annealing temperature for various rf power is shown in figure 4.5. It can be seen that with

143

the increase of band gap there is a decrease in resistivity due to an increase in carrier concentration. The film deposited at 150 W and post annealed in oxygen at 600 °C had the highest band gap, 1.09 eV and the lowest resistivity. This shift in band gap with the change in carrier concentration can be explained by Burstein – Moss (B–M) shift [23].
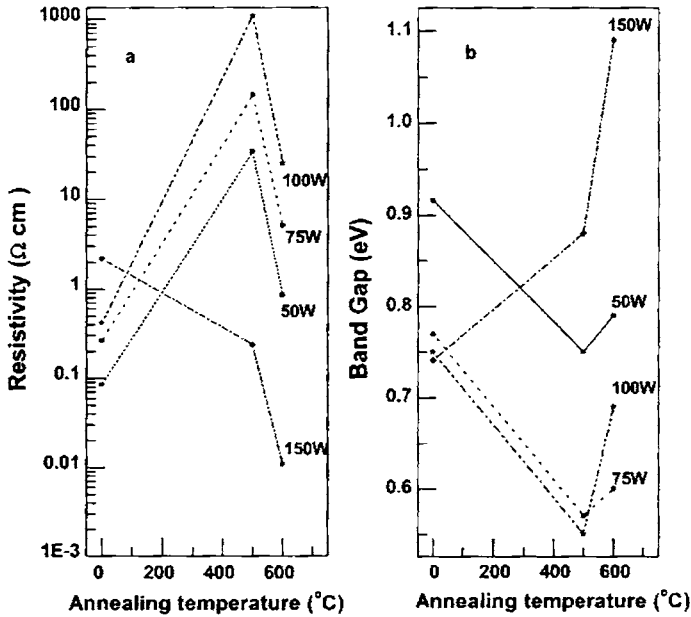
Figure 4.5 Variation of (a) resistivity and (b) band gap with annealing temperature for various rf power

Assuming that the conduction band and valence band are parabolic and B-M shift is the predominant effect; the band gap can be given by

$$E_g = E_{g0} + \Delta E_g^{B-M} , \qquad (4.1)$$

where E_{g0} is the intrinsic band gap and ΔE_g^{B-M} is the B-M shift. As the carrier concentration increases, in the case of a p-type conductor the low-lying levels in

144

the valence bands are filled. Since the Pauli principle prevents the states from being doubly occupied, and the optical transitions are vertical, the optical gap is given by the energy difference between the states with Fermi momentum in conduction and valence bands [23]. The B-M shift is given by

$$\Delta E_g^{B-M} = \frac{\eta^2}{2m_h^*}(3\pi^2 N)^{\frac{2}{3}}$$
(4.2)

where m_h^* is the effective mass of the hole carrier.

b) Influence of sputtering gas pressure and Ar:O₂ sputter gas ratio

The influence of sputtering gas pressure on the properties of LSCO thin films were studied by preparing the films at various Ar pressures. The deposition was carried out on quartz substrates at an rf power of 150 W at a target to substrate distance of 4 cm for a duration of one hour. The thickness of the films varied within 700-1000 nm depending on the sputtering gas pressure. The as deposited thin films were subjected to post deposition annealing in oxygen at 600 °C for one hour. The structural and electrical characterization of the thin films gave 0.003 mbar as the optimum Ar pressure. The structure of LSCO system and many other perovskites depends on the percentage of cation substitution and oxygen deficiency [25, 26]. The effect of oxygen in the structural and electrical properties of LSCO thin films were studied by preparing the films at various Ar:O₂ sputtering gas ratio, keeping the total deposition pressure at 0.003 mbar. The films were deposited on quartz, p-type Si <100> and MgO substrates. Single phase perovskite LSCO thin film could be obtained only when the films were deposited at low oxygen partial pressure.

(i) Structural Properties

Figure 4.6 gives the XRD pattern of the LSCO thin films deposited at various Ar pressures. The as deposited films were all crystalline and the peaks can be indexed to that of rhombohedral distorted perovskite LSCO structure, space group $R\bar{3}C$.
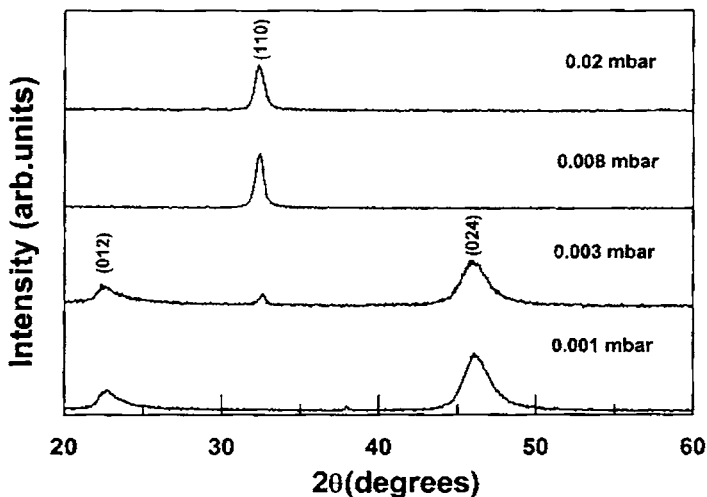
Figure 4.6 XRD pattern of the LSCO thin films deposited at various Ar pressure

The films deposited at low pressures had a reflection along (012). The films deposited at higher pressures had reflection along (110) direction only. The films deposited at 0.003 mbar had all the prominent peaks of perovskite LSCO and had a slightly larger grain size (20 nm) compared to the films deposited at other pressures (13 nm).

The films prepared with varying Ar:O_2 ratio resulted in the formation of LSCO thin films with some impurity phases of $SrCO_3$, except for that deposited on MgO substrate. But the films prepared with minimum oxygen in the Ar:O_2

146

sputter gas mixture (Ar:O$_2$ 80:20) was single phase. Figure 4.7 shows the XRD pattern of the LSCO thin films prepared with varying Ar:O$_2$ ratio deposited on MgO substrate. The figure clearly indicates the presence of perovskite LSCO for Ar:O$_2$ ratio 80:20. A considerable reduction in the sputtering rate was also observed with the increase of oxygen in the Ar:O$_2$ sputter gas ratio. The observed reduction in rate may be explained due to the negative oxygen ion bombardment to the growing film. The added oxygen causes the sputtering rate reduction because it decreases the amount of ionization and therefore reduces the sputtering ion impingement on the target. The formation of impurity phases may be due to the deterioration of the films caused by more negative ions reaching the growing film [27, 28].
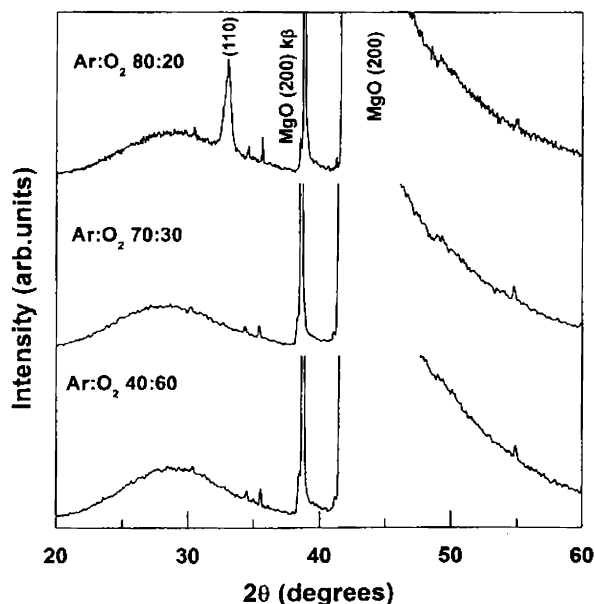
Figure 4.7 XRD pattern of the LSCO thin films prepared with varying Ar:O$_2$ sputter gas ratio deposited on MgO substrate

147

(ii) Electrical Properties

The temperature dependence of resistivity of the LSCO thin films deposited at 0.003 mbar on quartz substrates is given in figure 4.8. The figure clearly indicates a semiconductive character over the whole temperature range. The inset of the figure gives the plot of $\ln(\sigma T)$ Vs 1000/T above 200 K. The plot is approximately linear in the paramagnetic region indicating small polaron hoping conduction mechanism [15, 29].

Figure 4.8 Temperature dependence of resistivity of the LSCO thin film deposited at 0.003 mbar on quartz

Small polaron hopping conduction mechanism in LSCO can be explained as follows. LSCO belong to the group of narrow band semiconductors as the outer electrons of atoms in these materials are more localized. The electrons or holes in these narrow bands move either by tunneling through a potential well or by

148

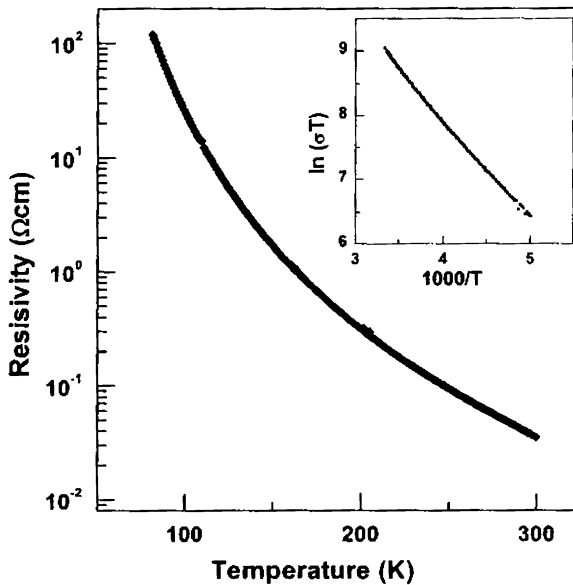hopping. When La^{3+} is substituted with Sr^{2+}, the charge neutrality is maintained by changing Co^{3+} to Co^{4+}. This causes the creation of a hole, which is localized over an area of the order of lattice constant and is referred to as a polaron. The mobility of the polaron occurs through a thermally activated process known as hopping. Thus the conduction in LSCO occurs through small polaron hopping [30].

The electrical conductivity by small polaron hopping conduction is given by

$$\sigma = \frac{(1-c)}{kT} ne^2 a_0 \gamma \exp(\frac{-E_a}{kT}) \qquad (4.3)$$

where , c is the fraction of sites occupied by polarons, E_a is the activation energy of hopping, n is the small polaron concentration , e is the electron charge, a_0 is the distance between the sites, γ is the optical phonon frequency and k is the Boltzmann constant. The slope of ln(σT) plotted against 1/T is equal to $\frac{-E_a}{k}$. The activation energy for hopping has been found from the graph and has a value of 0.15 eV. The slope change observed in the ln(σT) vs 1/T plot around 240 K is due to the paramagnetic to ferromagnetic phase transition occurring at that temperature [29].

Figure 4.9 shows the variation of resistivity of the LSCO thin films with sputtering gas pressure. The films prepared at a sputtering gas pressure of 0.003 mbar gave a minimum resistivity of 6×10^{-2} Ωcm. The resistivity was found to increase with the increase of sputtering gas pressure thereafter. Post deposition annealing in oxygen reduced the resistivity of the thin films by an order and the films deposited at 0.003 mbar gave a minimum resistivity of
5×10^{-3} Ωcm. The decrease in resistivity for the films annealed in oxygen at 600°C is due to the oxygen incorporation into the film at this temperature [21].

A similar effect as Sr^{2+} doping ie an increase in conductivity may be achieved by oxygen incorporation into LSCO thin films [22]. The figure clearly indicates an increase in resistivity with annealing for the films prepared at a sputtering gas pressure of 0.001 mbar. There was a slight increase in the lattice strain for the post annealed films prepared at 0.001 mbar compared to other pressures. In all the other cases the lattice strain and resistivity was found to decrease with annealing. The increase in resistivity of film deposited at this sputtering gas pressure (0.001 mbar) with annealing is due to the increase in lattice strain on annealing the thin films [6].
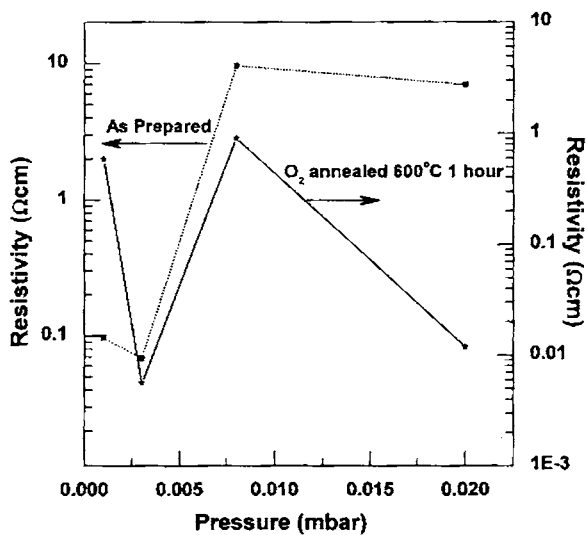
Figure 4.9 Variation of resistivity of the LSCO thin films with sputtering gas pressure

The variation of sputtering rate and resistivity with $Ar:O_2$ ratio is given in figure 4.10. The resistivity of the thin films was found to decrease with decrease in oxygen in the $Ar:O_2$ gas mixture whereas, the sputtering rate increased with decrease in oxygen partial pressure. The films deposited at an $Ar:O_2$ sputter gas ratio 80:20 gave the minimum resistivity, 2.5×10^{-3} Ωcm. The added oxygen

150

atom reduces the ionization thereby reducing the sputtering rate. The increase of oxygen partial pressure causes more negative ions to reach the growing film. The increase in resistivity with the increase of oxygen partial pressure is due to the deterioration of the thin films caused due to the high energetic negative ions striking the growing film [27, 28]. Decreasing the oxygen partial pressure minimizes these effects creating perovskite LSCO. The reduced resistivity of the LSCO thin film prepared at the lowest oxygen partial pressure is also due the single phase of perovskite LSCO formed at this condition.
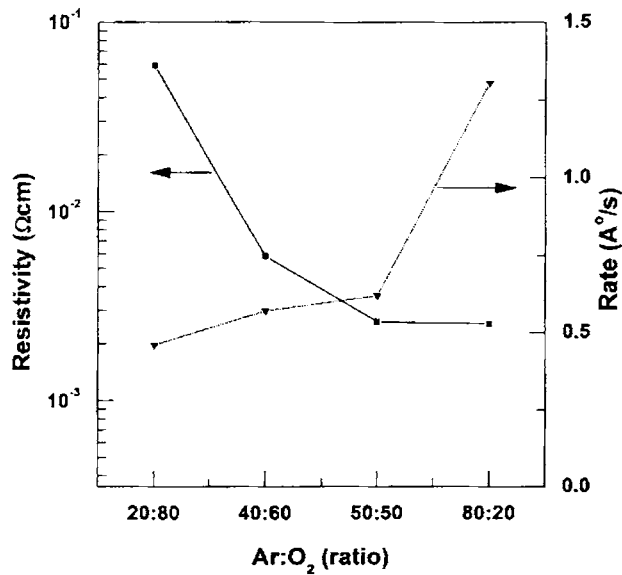

Figure 4.10 Variation of sputtering rate and resistivity of LSCO thin films with Ar:O_2 sputter gas ratio

4.3.2 Deposition at Substrate Temperature

The deposition of LSCO thin films at room temperature gave a resistivity of the order of 10^{-3} Ωcm. But the crystallinity of thin films was not appreciable to be

151

used as bottom electrode for ferroelectric devices. The poor crystallinity of the perovskite bottom electrode may adversely affect the growth and microstructure of ferroelectric thin films grown over them [31]. In order to improve the crystallinity of the LSCO thin films, the films were deposited at substrate temperature. The deposition was carried out at quartz, p-type Si <100> and $Pt/TiO_2/SiO_2/Si$ substrates. The thin films were prepared varying the sputtering gas pressure, $Ar:O_2$ sputter gas ratio and substrate temperature to obtain crystalline conducting LSCO thin films. The optimization of the deposition conditions on $Pt/TiO_2/SiO_2/Si$ and Si substrates offer the easy integrability into semiconductor devices and have the advantage of low cost and easy availability. The effect of substrate temperature on the structural and electrical properties of LSCO thin films were examined by depositing the films at two different sputtering gas pressures; viz. (1) a low pressure 0.003 mbar and (2) a high pressure 0.1 mbar.

(i) Structural Properties

The films prepared at low sputtering gas pressure 0.003 mbar showed no significant improvement in the crystallinity with the increase of substrate temperature. But the LSCO thin films prepared at a high sputtering gas pressure, 0.1 mbar; at a substrate temperature of 600 °C were better crystalline (FWHM = 0.1661°) compared to the films prepared at 0.003 mbar (FWHM = 0.4057°). The crystallization condition for LSCO thin films are reported to be at high temperatures (650 - 800 °C) and at high sputtering gas pressures (0.1 - 0.2 mbar) [31, 32]. Figure 4.11 shows the XRD pattern of the LSCO thin films prepared at 0.003 mbar and 0.1 mbar at a substrate temperature of 600 °C with an $Ar:O_2$ ratio 60:40 on Si substrates. The figure clearly indicates the improved crystallinity of the films deposited at 0.1 mbar.

The crystallinity of the thin films prepared at 0.1 mbar was found to increase with the decrease of oxygen in $Ar:O_2$ sputter gas ratio. A reduction in the

152

sputtering rate was also observed with the increase of oxygen partial pressure. The negative oxygen ions bombarding the growing film deteriorate the film properties and reduce the sputtering rate especially when substrates were heated during sputtering [27]. It was observed that the crystallinity of the LSCO thin films prepared at a substrate temperature 500 °C was comparable to that prepared at 600 °C. Therefore crystalline LSCO thin films could be prepared at a substrate temperature of 500 °C.
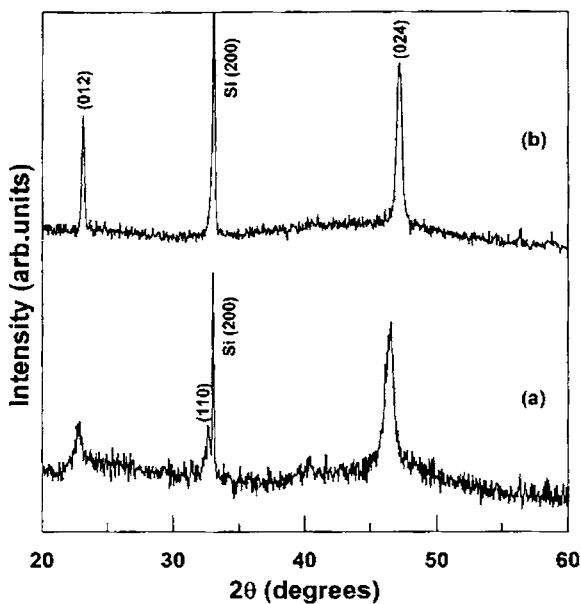
Figure 4.11 XRD pattern of the films prepared at (a) 0.003 mbar and (b) 0.1 mbar at a substrate temperature of 600 °C with an $Ar:O_2$ ratio 60:40 on Si substrates

(ii) Electrical Properties

The investigation of the electrical properties of the LSCO thin films deposited on substrate kept at higher temperature gave minimum resistivity for the films deposited at low oxygen partial pressure. This is due to the better film formation

153

devoid of any deterioration and resputtering which happens at higher oxygen partial pressures due to negative oxygen ion bombardment [27, 28]. Figure 4.12 shows the variation of resistivity with substrate temperature for the LSCO thin films deposited at a pressure of (a) 0.003 mbar and (b) 0.1 mbar. The variation is shown for the films deposited with Ar:O_2 sputter gas ratio 60:40. Minimum resistivity for the thin films was obtained for a substrate temperature of 500 °C irrespective of the sputtering gas pressure and substrates used. The films deposited on Si substrates gave low resistivity (10^{-3} Ωcm) than that on quartz substrates (10^{-2} Ωcm). The resistivity of the thin films was found to increase with further increase in substrate temperature due to the creation of oxygen vacancies at high substrate temperature [21, 22].
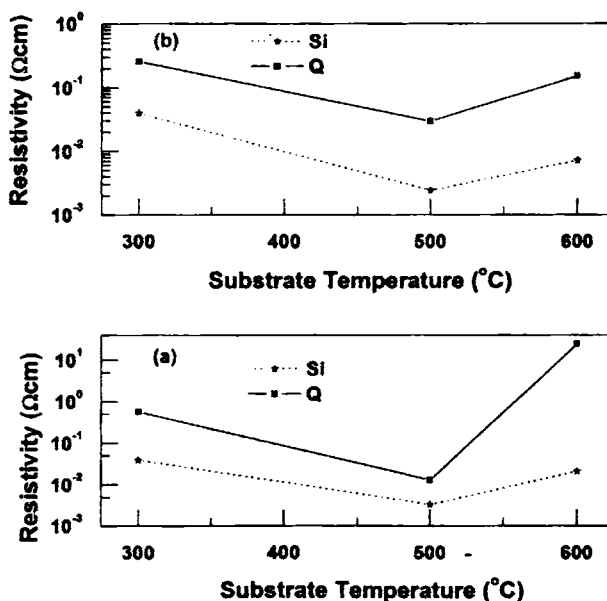

Figure 4.12 Variation of resistivity with substrate temperature for the films deposited at an Ar:O_2 sputter gas ratio 60:40 for a deposition pressure of (a) 0.003 mbar (b) 0.1 mbar

(iii) Surface Morphology

Figure 4.13 shows the atomic force microscopic images of the LSCO thin films prepared on (a) Pt/TiO$_2$/SiO$_2$/Si, (b) quartz and (c) Si substrate.
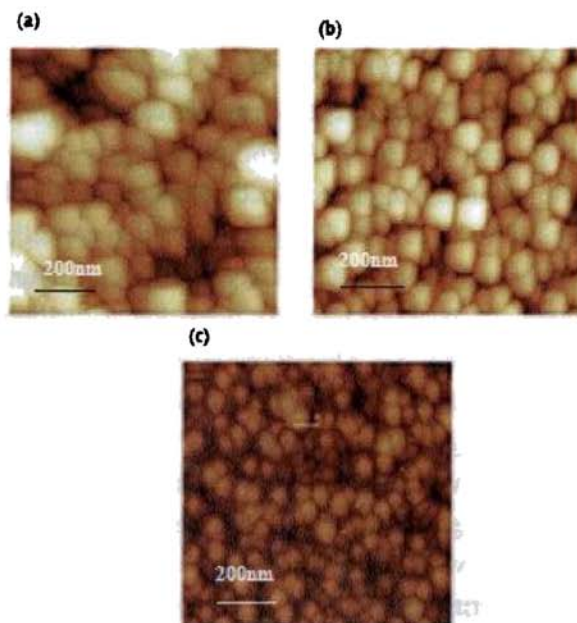
Figure 4.13 Atomic force microscopy images of the LSCO thin films prepared on (a) Pt/TiO$_2$/SiO$_2$/Si (b) quartz and (c) Si substrate. The films were deposited at substrate temperature of 500 °C at a deposition pressure of 0.1 mbar with Ar:O$_2$ ratio 60:40

The surface morphology is similar for all the films grown on different substrates except for the size of the particles and rms value of surface roughness. The size of the grains is smaller on the film prepared on Si substrate compared to that on Pt/TiO$_2$/SiO$_2$/Si and quartz substrate. The grains are uniformly distributed over the Si and quartz substrates whereas the grains form into large clusters in Pt/TiO$_2$/SiO$_2$/Si substrates. The rms value of roughness of LSCO film grown on Pt/TiO$_2$/SiO$_2$/Si substrates is 15 nm and that on quartz and Si substrates was

155

6nm and 4nm respectively. The increased roughness of the thin films prepared on $Pt/TiO_2/SiO_2/Si$ substrates is due to the higher thickness of the Pt layer (200 nm) beneath the LSCO layer [26, 33]. The smooth surface morphology of LSCO thin film on Si substrate makes it a better material for growing heterostructures [6].

4.4 Conclusion

$La_{0.5}Sr_{0.5}CoO_3$ thin films were prepared by rf magnetron sputtering. The rf power, sputtering gas pressure, $Ar:O_2$ sputter gas ratio and substrate temperatures were optimized to get conducting and crystalline thin films. The rf power was optimized to be 150 W. The post deposition annealing condition was optimized and found to be 600 °C in oxygen for one hour. The optimized sputtering gas pressure was 0.003 mbar for preparing crystalline and conducting thin films at room temperature. Deterioration of the film properties with the reduction in the sputtering rate was observed with the increase of oxygen partial pressure during sputtering. The films prepared with the minimum oxygen partial pressure ($Ar:O_2$ 80:20) was single phase with minimum resistivity. The films prepared with sputtering gas pressure of 0.003 mbar did not show any significant variation in crystallinity with the increase of substrate temperature. But the films prepared at high sputtering pressure, 0.1 mbar showed variation in crystallinity with substrate temperature. The crystallinity of the thin films was found to increase with the decrease in oxygen partial pressure with the films prepared at $Ar:O_2$ ratio 60:40 better crystalline compared to others. The temperature dependence of resistivity of the LSCO thin films indicated a semiconductive conduction mechanism. The resistivity in the paramagnetic region indicated a small polaron hopping conduction mechanism. The optimized growth condition for crystalline conducting LSCO thin films were, a substrate temperature of 500°C with a sputtering gas pressure of 0.1 mbar with $Ar:O_2$ sputter gas ratio 60:40.

References

1. D.P.Norton, Materials Science and Eng.R. **43**(2004)139
2. V.R.Plakar, S.C.Purandare, R.Pinto, J.Phys.D:Appl.Phys. **32**(1999)R1
3. J.B.Goodenough, J.Phys.Chem.Solids. **6**(1958)287
4. P.M.Raccah, J.B.Goodenough, J.Appl.Phys. **39**(1968)1209
5. R.Ramesh, H-Gilchrist, T.Sands, V.G.Keramidas, R.Haakenaasen, D.K.Fork, Appl.Phys.Lett. **63**(1993)3592
6. J.T.Cheung, P.E.D.Morgan, D.H.Lowndes, S-Y Zheng, J.Breen, Appl.Phys.Lett. **62**(1993)2045
7. R.Dat, D.J.Lichtenwalner, O.Auciello, A.J.Kingon, Appl.Phys .Lett. **64**(1994)2673
8. R.Ramesh, J.Lee, T.Sands, V.G.Keramidas, O.Auciello, Appl.Phys.Lett. **64**(1994)2511
9. Y.Furusawa, H.DOI, Jpn.J.Appl.Phys. **38**(1999)6864
10. Y.F.Chen, L.Sun,T.Yu, J-X Chen,Y-Y Zhu, N-B Ming, X-Y Chen, Z-G Liu, Thin Solid Films. **269**(1995)18
11. Y.Ohno, S.Nagata, H.Sato, Solid State Ionics. **3/4**(1981)439
12. H.J.M.Bouwmester, H.Kruidhof, A.Burggraaf, Solid State Ionics. **72**(1994)185
13. N.Lehisa, K.Fukaya, K.Matsuo, N.Horiuchi, N.Karube, J.Appl.Phys. **59**(1986)317
14. K.Tabata, I.Matsumoto, J.Mater.Sci. **22**(1987)1882
15. H.D.Bhatt, R.Vedula, S.B.Desu, G.C.Fralick, Thin Solid Films. **350**(1999)249
16. R.H.E.van Doorn, A.J.Burggraaf, Solid State Ionics. **128**(2000)65
17. P.K.Song, Y.Shigesato, M.Kamei, I.Yasui, Jpn.J.Appl.Phys. **38**(1999)2921
18. M.Girtan, G.I.Rusu, G.G.Rusu, Mater.Sci.Eng.B. **76**(2000)156
19. J.Mizusaki, Y.Mima, S.Yamauchi, K.Fucki, H.Tagawa, J.Solid.State.Chem. **80**(1989)102

20. X.Chen, N.Wu, A.Ignatiev, Z.Zhang, W-K.Chu, Thin Solid Films. **350**(1999)130

21. L.J.Meng, M.P.dos.Santos, Thin Solid Films. **322**(1998)56

22. S.Madhukar, S.Aggarwal, A.M.Dhote, R.Ramesh, A.Krishnan, D.Keeble, E.Poindexter, J.Appl.Phys. **81**(1997)3543

23. B.E.Sernelius, K.F.Berggren, Z.C.Jin, I.Hamberg, C.G.Granqvsit, Phys.Rev.B. **37**(1998)10244

24. J.M.Liu, C.K.Ong, J.Appl.Phys. **84**(1998)5560

25. V.V.Kharton, E.N.Naumovich, A.A.Vecher, A.V.Nicolaev, J.Solid.State.Chem. **120**(1995)128

26. H.Ohbayashi, T.Kudo, T.Gejo, Jpn.J.Appl.Phys. **13**(1974)1

27. A.Hamerich, R.Wunderlich, J.Muller, J.Vac.Sci.Technol.A. **12**(1994)2873

28. J.B.Lounsbury, J.Vac.Sci.Technol. **6**(1968)838

29. J.Yin, L.Wang, J.M.Liu, K.J.Chen, Z.G.Liu, Q.Huang, Appl.Phys.Lett. **76**(2000)580

30. D.Emin, T.Holstein, Ann.Phys. **53**(1969)439

31. S-M.Yoon, E.Tokumitsu, H.Ishiwara, Appl.Surf.Sci. **117/118**(1997)447

32. M.Li, Z-L.Wang, S.Fan, Q-T.Zhao, G.Xiong, Thin Solid Films. **323**(1998)304

33. J.Yin, W.Cai, Y.Zhang, L.Zhao, Surf.Coat.Tech. **198**(2005)329

CHAPTER 5

Preparation and Characterization of $La_{0.5}Sr_{0.5}Co_{0.5}Ni_{0.5}O_3$ Thin Films

$La_{0.5}Sr_{0.5}Co_{0.5}Ni_{0.5}O_3$ (LSCNO) thin films were prepared by rf magnetron sputtering. The sputtering gas pressure, $Ar:O_2$ ratio in the sputtering gas and substrate temperature has been optimized to get better conducting perovskite thin films. The thin films were deposited on various substrates such as quartz, p-type Si <100> and $Pt/TiO_2/SiO_2/Si$. The sputtering gas pressure was optimized to be 0.003 mbar for conducting and crystalline thin films at room temperature. Oxygen incorporation was found to improve the crystallinity and conductivity. A substrate temperature of 300 °C at a sputtering gas pressure of 0.1 mbar with $Ar:O_2$ sputter gas ratio 50:50 was the optimum growth condition for crystalline thin films. Crystalline thin films were obtained irrespective of the substrate material at the optimized deposition condition. The LSCNO thin film deposited on $Pt/TiO_2/SiO_2/Si$ substrate have the advantage of lower resistivity of Pt and improved fatigue behavior associated with LSCNO thin film.

5.1. Introduction

Ferroelectric thin films are one of the foremost and essential components for a wide spectrum of applications. Perovskite ferroelectrics are widely used in memory devices, microwave electronic components and micro devices [1]. $La_{0.5}Sr_{0.5}CoO_3$ (LSCO) thin films; a perovskite oxide have been extensively investigated as electrode for ferroelectric memory devices [2-5]. $LaNiO_3$ is yet another metallic oxide which crystallizes in rhombohedral distorted perovskite structure. But $LaNiO_3$ is unstable and it decomposes in air above 860 °C. $LaNiO_3$ doped with Co forms a highly stable and conductive mixed oxide $LaNi_{1-x}Co_xO_3$. $LaNi_{1-x}Co_xO_3$ is also widely used as electrode for ferroelectric memory devices [6]. The partial substitution of Co by Ni in $La_{0.5}Sr_{0.5}CoO_3$ has been reported to increases the electrical conductivity of LSCO thin films [7]. The perovskite gas sensor based on $La_{0.8}Sr_{0.2}Co_{1-x}Ni_xO_{3-\delta}$ is reported to offer a lower operating temperature (180 °C) for CO detection [8]. The properties of $La_{0.5}Sr_{0.5}Co_{0.5}Ni_{0.5}O_3$ as transparent electrodes in a shutter-based infrared sensor protection device have been investigated recently [7].

This chapter describes the growth and characterizations of ($La_{0.5}Sr_{0.5}Co_{0.5}Ni_{0.5}O_3$) LSCNO thin films. The LSCNO thin films were prepared by rf magnetron sputtering. The sputtering gas pressure, substrate temperature and $Ar:O_2$ ratio in the sputtering gas has been optimized to get better conducting perovskite thin films. Crystalline LSCNO thin films could be grown at low substrate temperature. The low temperature deposition of LSCNO electrodes opens up the possibility of fabricating ferroelectric capacitors at low temperatures. A low process temperature of ferroelectric capacitor is highly desirable to maintain the integrity of the plug material and underlying CMOS circuitry during the integration of the ferroelectric capacitor with access transistor.

5.2. Experimental Details

LSCNO thin films were prepared by rf magnetron sputtering using LSCNO powder target. LSCNO powder has been prepared by solid state reaction as described in the section 3.2 of chapter 3. The powder was packed on to a copper plate of 2-inch diameter and the powder LSCNO of thickness 2 mm was used as the target for sputtering.

The rf power was optimized to be 150 W during the preparation of LSCO thin films. The deposition of LSCNO thin films was also carried out at an rf power of 150 W. The sputtering duration was one hour with a target to substrate distance of 4 cm. High purity Argon gas was admitted into the chamber after attaining high vacuum (3×10^{-6} mbar). The Ar flow was adjusted using a mass flow controller. The room temperature deposition of the thin films was carried out on p-type Si <100> substrates. In this case the total sputtering pressure of Ar was first optimized and then optimized the $Ar:O_2$ ratio in the sputtering gas. The as deposited thin films were subjected to post deposition annealing in oxygen at 600 °C for 1 hour to improve the crystallinity and conductivity. The films were cooled down to room temperature under the oxygen flow so as to prevent the formation of oxygen vacancies at high growth temperatures. LSCNO thin films were grown at various substrate temperatures and on various substrates such as fused silica, p-type Si <100> and $Pt/TiO_2/SiO_2/Si$. The condition such as sputtering gas pressure, substrate temperature and oxygen partial pressure were varied to optimize the growth of crystalline and conducting LSCNO thin films.

The thickness of the films were found using Stylus profiler (Dektak 6M). The structural characterizations were carried out using a Rigaku X-ray diffractometer with Cu K_α radiation (λ=1.5418 A°). The room temperature electrical properties of the films were studied using a Keithley Source Measure Unit (SMU 236). The electrical conductivity and its temperature dependence were measured by

Vanderpauw four probe method. Atomic force microscope was used to study the surface morphology and film roughness.

5.3. Results and Discussion

The growth of the LSCNO thin films are described in the following two sections viz. (i) the room temperature growth followed by post deposition annealing and (ii) the growth at elevated substrate temperature.

5.3.1 Effect of room temperature deposition and post deposition annealing

The deposition of the thin films was initially carried out varying the Ar pressure. All the films had a thickness around 800 nm irrespective of the variation in Ar pressure. The as deposited thin films were subjected to post deposition annealing in oxygen at 600 °C for one hour. The annealing condition was optimized during the growth of LSCO thin films. The Ar pressure 0.003 mbar during deposition resulted in better crystalline and electrical conducting film.

The structure of LSCO system and many other perovskites depends on the percentage of cation substitution and oxygen deficiency. Kharton et al. [9] has reported that annealing the perovskite thin films in oxygen deficient atmospheres results in structural phase transition to brownmillerite-like phases. Annealing in reducing conditions creates oxygen vacancies, which breaks the perfect oxygen octahedra around the Co ions, distorting the perovskite structure [10, 11]. The effect of oxygen on the structural and electrical properties of LSCNO thin films were studied by preparing the films at various Ar:O_2 sputter gas ratio, keeping the total sputtering gas pressure at 0.003 mbar. The conductivity of the films prepared with oxygen incorporation was found to be better than that prepared without oxygen, even without post deposition annealing.

165

(i) Structural Properties

The XRD pattern of the as deposited LSCNO thin films deposited at various Ar pressure is as given in figure 5.1. The peaks of $LaNiO_{2.5}$ and $La_{1.6}Sr_{0.4}NiO_{3.5}$ which were present in the XRD pattern of the LSCNO powder were not detected in the XRD pattern of the thin films. All the peaks can be indexed to that of rhombohedral distorted perovskite LSCNO structure, space group $R\bar{3}C$. The space group identifies the system to be fully oxygenated [12]. The main diffraction peak (024) indicated a preferred orientation of the film along (012) direction.
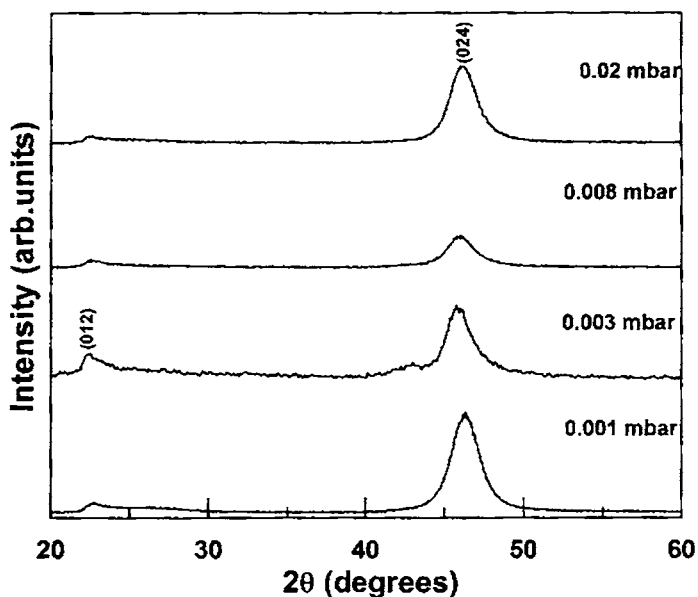

Figure 5.1.XRD pattern of the as deposited LSCNO thin films prepared at various pressures

The calculation of the grain size of the thin films using Scherer's formula indicated no significant variation in grain size with Ar pressure. The films

166

prepared at 0.003 mbar had a slightly larger grain size (7 nm) compared to others (4 nm). Also there was no appreciable improvement in the grain size with post deposition annealing.

The grain size of the films prepared with varying $Ar:O_2$ sputter gas mixture was found to vary with the oxygen partial pressure. The films deposited at the highest oxygen partial pressure ($Ar:O_2$ ratio 20:80) had the maximum grain size (10 nm). The grain size was found to decrease with decrease in oxygen partial pressure and the films deposited with lowest oxygen partial pressure ($Ar:O_2$ ratio (80:20)) had the minimum grain size (3 nm). The increase in grain size with increase in oxygen partial pressure is due to the better oxygen incorporation into the thin films [11].
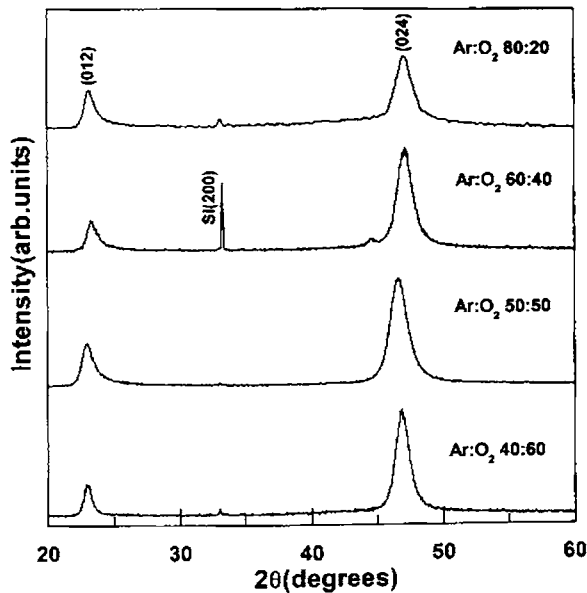

Figure 5.2.XRD pattern of the LSCNO thin films grown by varying $Ar:O_2$ sputter gas ratio and then subjected to post deposition annealing in oxygen at 600 °C

Figure 5.2 shows the XRD pattern of the post deposition annealed LSCNO thin films prepared at various Ar:O_2 sputter gas ratio, keeping the total deposition pressure at 0.003 mbar. The figure clearly indicates presence of the prominent peaks (012) and (024) of perovskite LSCNO. The grain size of the post annealed samples was found to be greater than the as deposited films which further justifies that oxygen incorporation into the films increases the crystallinity.

(ii) Electrical Properties

The variation of resistivity of LSCNO thin films with Ar pressure during sputtering is shown in figure 5.3 (a). The films deposited at deposition pressure of 0.003 mbar gave a minimum resistivity of 8×10^{-3} Ωcm. Figure 5.3 (b) shows the variation of resistivity of the LSCNO thin films with Ar:O_2 ratio in the sputtering gas. A minimum resistivity of 1×10^{-3} Ωcm was obtained for the films prepared with highest oxygen partial pressure (Ar:O_2 ratio 20:80). The resistivity of the films prepared in the presence of oxygen remained in the order of 10^{-3} Ωcm. The lowering of resistivity with the increase of oxygen partial pressure during sputtering may be due to the incorporation of oxygen into the thin films. The low electrical resistivity of LSCO is attributed to the multivalent state of the Co ion. For every Sr^{2+} ion introduced in the lattice, a Co^{3+} ion oxidizes to Co^{4+} ion. These Co^{4+} ions sitting on what was originally Co^{3+} sites are positively charged holes responsible for high electrical conductivity. It has been reported that a similar effect as Sr^{2+} doping ie an increase in conductivity may be achieved by oxygen incorporation into LSCO thin films [10, 13].
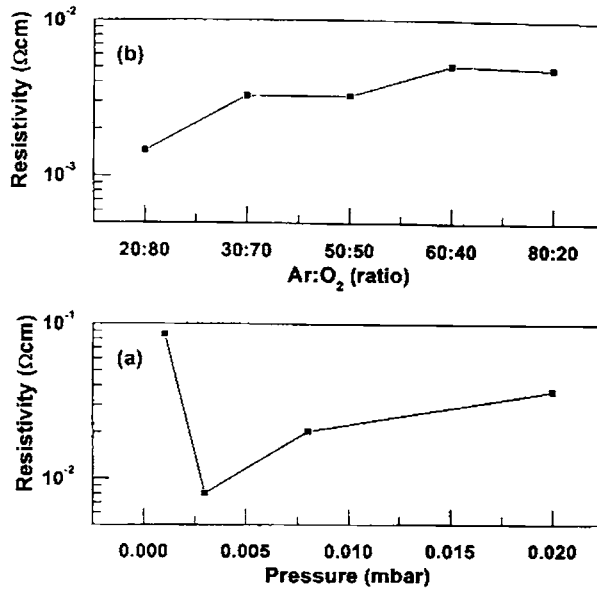
-

Figure 5.3. Variation of resistivity of LSCNO thin films (a) with Ar pressure (b) with Ar:O₂ sputter gas ratio

The dependence resistivity on Ar:O$_2$ sputter gas mixture may be related to the role that the oxygen stoichiometry plays in the electrical transport of LSCO. Both the conductivity and carrier concentration of bulk LSCO is reported to be decreasing with decrease in oxygen partial pressure from the measurements of electrical conductivity and Seebeck coefficient [14]. This is directly related to the change in the oxygen stoichiometry of LSCO corresponding to a larger oxygen deficiency. Furthermore, since the metallic conductivity of LSCO results from the formation of an "impurity band" composed of the Co-3d and O-2p orbitals, a disruption of the Co-O network due to oxygen vacancies, may affect the carrier mobility [14, 15]. Therefore it is reasonable to expect that the Ar:O$_2$ sputter gas mixture can affect oxygen stoichiometry and thus the conductivity of LSCNO thin films.
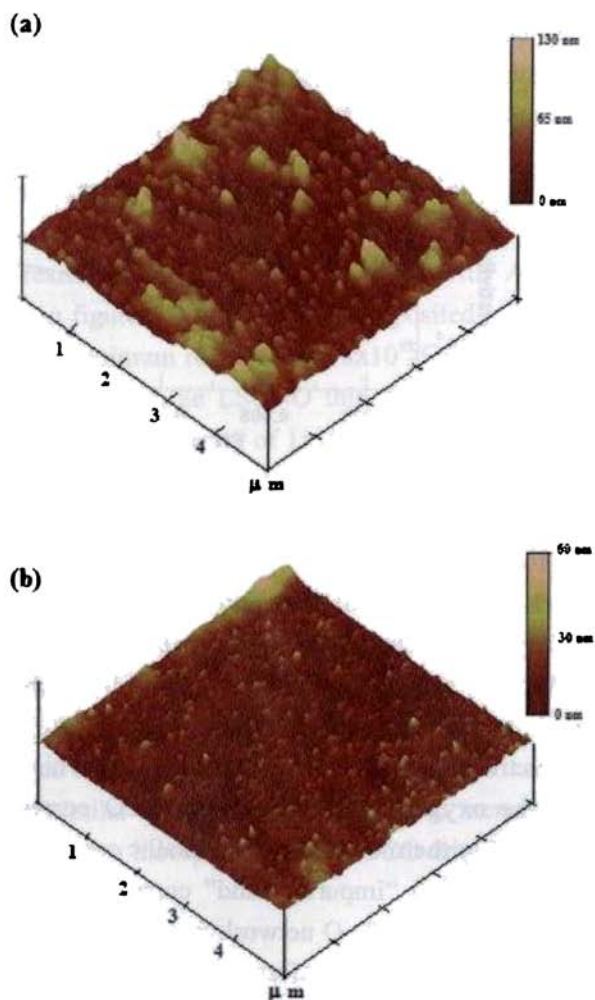
(iii) Surface Morphology

Figure 5.4.Atomic force microscopy images of the LSCNO thin films prepared
(a) without oxygen intercalation and (b) with oxygen intercalation during sputtering

Figure 5.4 shows the atomic force microscopy images of the LSCNO thin films prepared (a) without oxygen intercalation (sputtering in pure Ar gas) and (b) with oxygen intercalation during sputtering (sputtering in Ar and oxygen mixture). The films grown without oxygen intercalation had an average roughness of 2.37 nm. The AFM image shows a dense and continuous film composed of small grains with some agglomerations. But the films grown with oxygen intercalation were exceptionally smooth and had an average roughness of only 0.82 nm. The smooth morphology is due to the isotropic growth rate of LSCNO thin film along [0$\bar{2}$1] orientation i.e. along (012) and (024) planes [3]. Thus oxygen incorporation into LSCNO thin films forms better conducting film with a much smoother surface. The smooth surface morphology of LSCNO makes it a better material for growing heterostructures.

5.3.2 Growth at Substrate Temperature

The room temperature deposition of the LSCNO thin films gave a resistivity of the order of 10^{-3} Ωcm. But the crystallinity of the films was very poor. The crystallinity of the bottom electrode is reported to directly influence the nucleation, the microstructure and the electrical properties of the ferroelectric deposited over it. Therefore a highly crystalline LSCNO layer is desirable for its use as electrode in ferroelectric memory devices. In order to improve the crystallinity and conductivity of the LSCNO thin films, films were deposited at higher substrate temperature. The sputtering gas pressure, substrate temperature and Ar:O$_2$ ratio in the sputtering gas were varied to get crystalline conducting LSCNO thin films at the lowest possible substrate temperature. The deposition was carried out on fused silica, p-type Si <100> and Pt/TiO$_2$/SiO$_2$/Si substrates to investigate the effect of various substrates on the properties of LSCNO thin films. The growth of LSCNO on p-type Si <100> and Pt/TiO$_2$/SiO$_2$/Si substrates is particularly important considering the device fabrication using LSCNO as bottom electrode.

171

(i) Structural Properties

Figure 5.5 shows the XRD pattern of the LSCNO thin films on Si substrates prepared at various sputtering gas pressure. The deposition was carried out at a substrate temperature of 600 °C keeping the Ar:O$_2$ ratio in the sputtering gas 20:80. All the peaks can be indexed to that of rhombohedral distorted perovskite LSCNO structure, space group $R\bar{3}C$. The main diffraction peak is along (024) direction. The films deposited at 0.1 mbar had all the diffraction peaks of perovskite LSCNO and was crystalline (FWHM = 0.541°) compared to the films deposited at other pressures (FWHM = 1.126°). The sputtering gas pressure,
0.1 mbar was therefore chosen as the optimum pressure for further deposition of thin films. The films were deposited on various substrates varying the substrate temperature. The films grown at a substrate temperature of 300 °C at sputtering gas pressure 0.1 mbar are crystalline and have a lower resistivity.
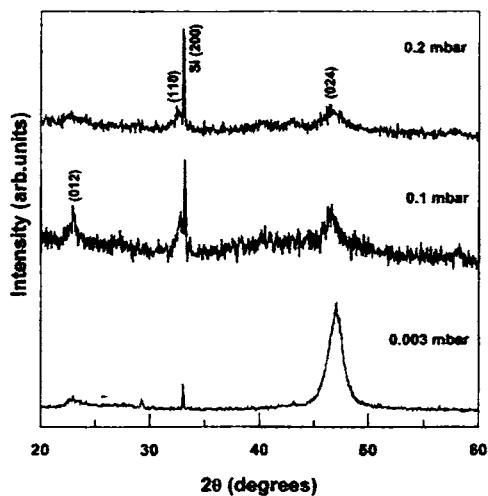

Figure 5.5.XRD pattern of the LSCNO thin films on Si substrates prepared at a substrate temperature of 600 °C with varying sputtering gas pressure
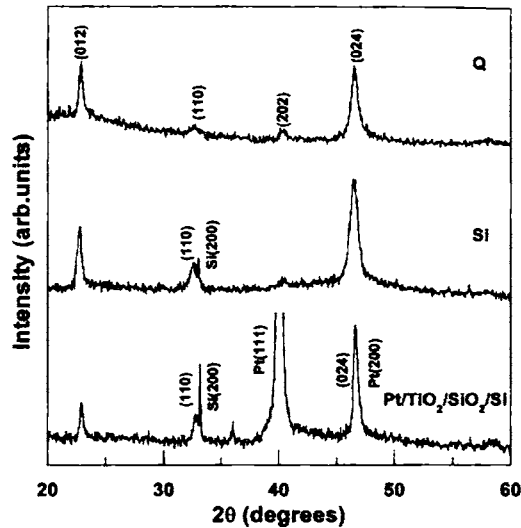(Ar:O$_2$ ratio 20:80)

Figure 5.6.XRD pattern of the LSCNO thin films deposited at 300 °C at 0.1 mbar with
an Ar:O$_2$ ratio 50:50 on various substrates

The effect of oxygen partial pressure on the properties of the LSCNO thin films
was investigated by preparing the thin films at various Ar:O$_2$ sputter gas mixture.
The films were deposited at a substrate temperature of 300 °C. The films
deposited at an Ar:O$_2$ sputter gas mixture 50:50 showed all the major peaks of
perovskite LSCNO and has a smaller FWHM (0.27°). Figure 5.6 shows the XRD
pattern of the LSCNO thin films deposited at 300 °C at 0.1 mbar with an Ar:O$_2$
ratio 50:50 on various substrates. All the films had the major peaks of perovskite
LSCNO. The (024) reflection of the perovskite LSCNO in Pt/TiO$_2$/SiO$_2$/Si
substrate is shadowed due to the strong intensity of (200) reflection of Pt at the
same angle (2θ = 46.5°). It is interesting to note that similar (024) oriented
LSCNO films are obtained irrespective of materials of substrate. The result
indicates that the low temperature crystallization and oriented growth of LSCNO
films are dominated by deposition factors rather than the substrate. It is most
likely related to the effect from a direct bombardment of the film by energetic
particles during sputtering [16]. A substrate temperature of 300 °C at a

173

sputtering gas pressure of 0.1 mbar with Ar:O_2 ratio 50:50 was obtained as the the optimum condition for crystalline LSCNO thin films. The crystallization temperature is much less than the reported crystallization temperature (700 °C) of LSCNO thin films prepared by dipping method and rf sputtering [8].

(ii) Electrical Properties

The temperature dependence of electrical resistivity of LSCNO thin film deposited on Si substrates is shown in figure 5.7. The films were deposited at a substrate temperature of 300 °C at a sputtering gas pressure of 0.1 mbar with Ar:O_2 ratio 20:80. The resistivity of the thin films increased by two orders of magnitude as the temperature was decreased from 300 K to 50 K, indicating a semiconducting behavior. This behavior is generally shown when LSCO thin film is deposited on Si substrate or single crystal substrate [17].
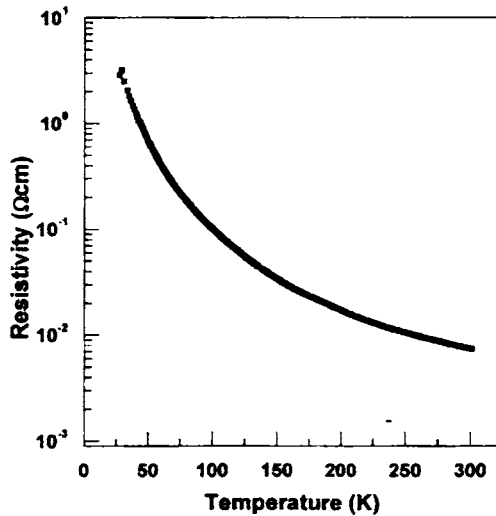

Figure 5.7.Temperature dependence of resistivity of LSCNO thin film deposited on Si substrates at a substrate temperature of 300 °C at a sputtering gas pressure of 0.1 mbar with Ar:O_2 ratio 20:80

174

The variation of resistivity of the LSCNO thin films deposited at 0.1 mbar at an Ar:O$_2$ sputter gas ratio 20:80 with substrate temperature is as given in figure 5.8 (a). The resistivity of the LSCNO thin films grown on quartz and p-type Si substrates are more or less the same ($\sim$ 10^{-2} Ωcm) and independent of substrate temperature in the studied range (300 °C - 600 °C). The LSCNO thin films deposited on p-type Si substrate gave a minimum resistivity of 6x10^{-3} Ωcm at 500 °C. The LSCNO thin films deposited on Pt/TiO$_2$/SiO$_2$/Si substrates gave a minimum resistivity of 5.74x10^{-5} Ωcm at a substrate temperature of 300 °C. This low resistivity is obviously due to the parallel conduction through the Pt layer beneath the LSCNO film [16]. While it is reported that the LSCO electrodes alleviates the fatigue problem of ferroelectric capacitor, it may adversely affect the frequency response of non volatile memory devices due to its relatively large resistivity compared to conventional Pt electrodes. Thus the use of a composite electrode LSCO/Pt/TiO$_2$/SiO$_2$/Si have the advantage of lower resistivity of Pt electrode and the improved fatigue behavior associated with LSCO electrodes [18, 19].

Figure 5.8 (b) shows the resistivity variation of the LSCNO thin films grown on various substrates at a substrate temperature of 300 °C at a sputtering gas pressure of 0.1 mbar with Ar:O$_2$ sputter gas ratio. A minimum resistivity of 3x10^{-3} Ωcm was obtained at an Ar:O$_2$ ratio of 50:50 on quartz and silicon substrates. This may be due to improved crystallinity and better oxygen incorporation into the films at this particular condition. There was no further reduction in the resistivity with the increase of oxygen partial pressure. The oxygen concentration in these films might have reached saturation at this particular condition [20]. The variation of resistivity with Ar:O$_2$ sputter gas mixture of the LSCNO thin films deposited on Pt/TiO$_2$/SiO$_2$/Si substrates was quite different from that on quartz and silicon substrates. The films deposited with maximum oxygen partial pressure were better conducting and the resistivity was found to increase with decrease in oxygen partial pressure. The behavior is similar to that observed on the LSCNO films deposited on quartz and p-type Si

substrates at room temperature. The reduced resistivity of the films prepared on Pt/TiO$_2$/SiO$_2$/Si at Ar:O$_2$ ratio 20:80 compared to the better crystalline film at Ar:O$_2$ ratio 50:50 may be due to more oxygen incorporation into the films at high oxygen partial pressure [10,13].
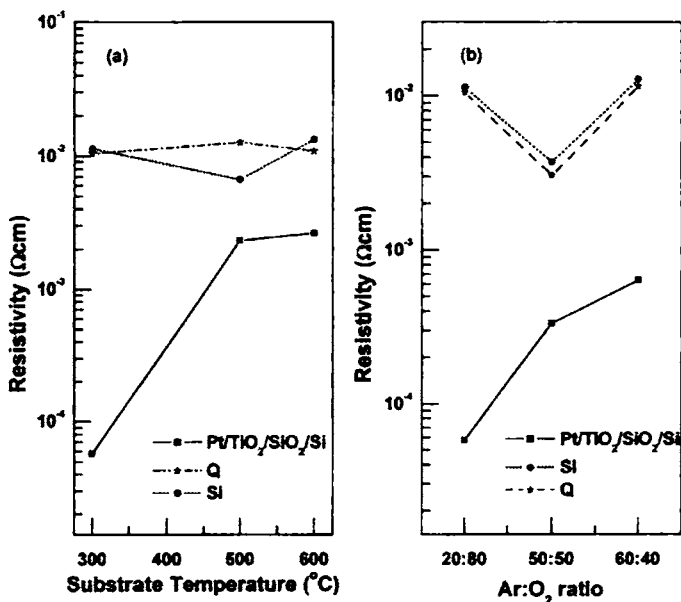
Figure 5.8. Variation of resistivity for the films deposited at 0.1 mbar (a) with substrate temperature (b) with Ar:O$_2$ sputter ratio for the films deposited at a substrate temperature of 300 °C.

(iii) Surface Morphology

Figure 5.9 shows the atomic force microscopy images of the LSCNO thin films prepared on (a) Si (b) Quartz and (c) Pt/TiO$_2$/SiO$_2$/Si substrate. The films were deposited at a substrate temperature of 300 °C at a sputtering gas pressure of 0.1 mbar with Ar:O$_2$ ratio 50:50.
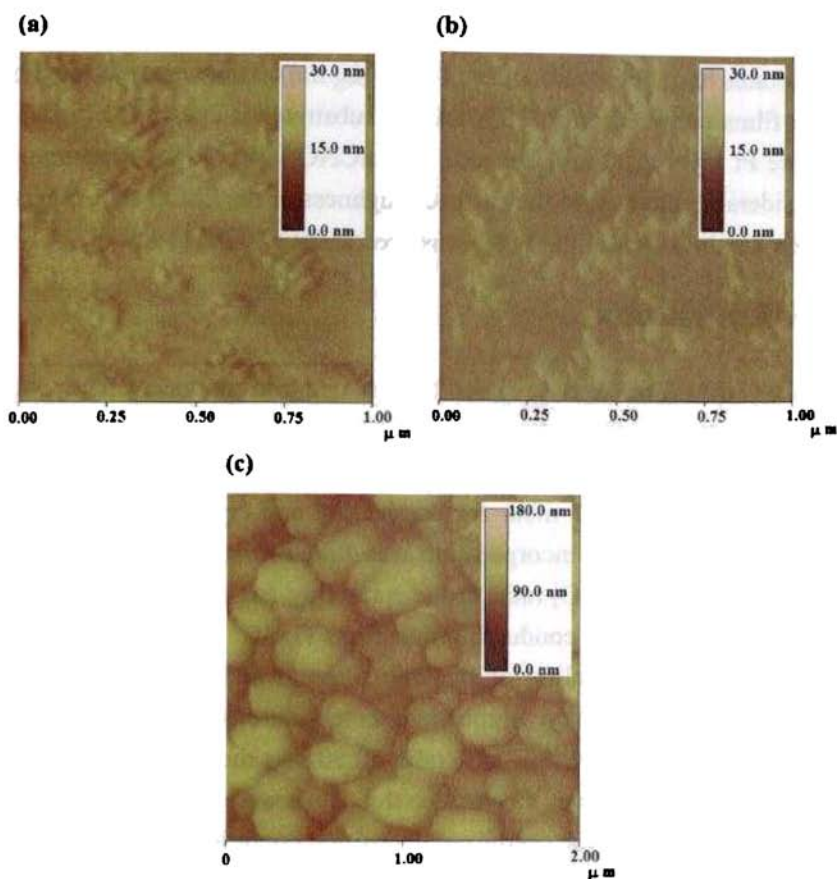
Figure 5.9. Atomic force microscopy images of the LSCNO thin films prepared on (a) Si (b) Quartz and (c) $Pt/TiO_2/SiO_2/Si$ substrate

The films deposited on Si substrates were exceptionally smooth without any type of surface features and had an average roughness of only 0.6 nm. This smooth morphology makes this film a better material for growing heterostructures [3]. The film deposited on quartz substrate is seen to be agglomerated composed of smaller particles. The individual grains are not clearly visible and the film had an average roughness of 2 nm. The grains are

177

spherical in shape and the grain boundaries are clearly seen in the films deposited on $Pt/TiO_2/SiO_2/Si$ substrates. The films prepared on $Pt/TiO_2/SiO_2/Si$ substrates had the maximum roughness (10 nm). The increased roughness of the thin films prepared on $Pt/TiO_2/SiO_2/Si$ substrates is due to the higher thickness of the Pt layer (200 nm) beneath the LSCNO layer. It has been reported that a considerable increase in the surface roughness of the LSCO thin film is observed when the thickness of the Pt layer is greater than 80 nm [19, 21].

5.4. Conclusion

LSCNO thin films were prepared by rf magnetron sputtering. The sputtering gas pressure, $Ar:O_2$ ratio in the sputtering gas and substrate temperature were varied to obtain conducting and crystalline thin films. The sputtering gas pressure was optimized to be 0.003 mbar for conducting and crystalline thin films at room temperature. Oxygen incorporation was found to improve the crystallinity and conductivity. The $Ar:O_2$ ratio in the sputtering gas was optimized for obtaining better crystalline and conducting thin films ($1x10^{-3}$ Ωcm) at room temperature. Post deposition annealing of the thin films at 600 °C in oxygen is found to improve the crystallinity. A substrate temperature of 300 °C at a sputtering gas pressure of 0.1 mbar with $Ar:O_2$ ratio 50:50 was the optimum growth condition for crystalline thin films. Crystalline thin films were obtained irrespective of the substrate material at the optimized deposition condition. The electrical resistivity of the thin films as a function of temperature shows a semiconductor behavior. A minimum resistivity of $3x10^{-3}$ Ωcm was obtained for the film deposited on quartz and p-type Si substrates at a temperature of 300 °C at an $Ar:O_2$ ratio of 50:50. The films deposited on $Pt/TiO_2/SiO_2/Si$ substrates showed considerable variation in resistivity with deposition conditions and gave a minimum resistivity of $5.68x10^{-5}$ Ωcm. Thus the LSCNO thin film deposited on $Pt/TiO_2/SiO_2/Si$ substrate have the advantage of lower resistivity of Pt and improved fatigue behavior associated with LSCNO electrodes in ferroelectric capacitor applications. The atomic force microscopy images of the thin films

178

revealed a smooth surface for the films prepared with oxygen intercalation. An exceptionally smooth surface for the thin films deposited on Si substrates facilitates its use in high quality integrated devices.

-

References

1. N.Settera, D.Damjanovic, L.Eng, G.Fox, S.Gevorgian, S.Hong, A.Kingon, H.Kohlstedtb, N.Y.Park, G.B.Stephenson, I.Stolitchnov, A.K.Taganstev, D.V.Taylor, T.Yamada, S.Streiffer, J.Appl.Phys. **100**(2006)051606

2. R.Ramesh, H-Gilchrist, T.Sands, V.G.Keramidas, R.Haakenaasen, D.K.Fork, Appl.Phys.Lett. **63**(1993)3592

3. J.T.Cheung, P.E.D.Morgan, D.H.Lowndes, S-Y Zheng, J.Breen, Appl.Phys.Lett. **62**(1993)2045

4. R.Dat, D.J.Lichtenwalner, O.Auciello, A.J.Kingon, Appl.Phys .Lett. **64**(1994)2673

5. R.Ramesh, J.Lee, T.Sands, V.G.Keramidas, O.Auciello, Appl.Phys.Lett **64**(1994)2511

6. H.Han, J.Zhong, S.Kotru, P.Padmini, X.Y.Song, R.K.Pandey, Appl.Phys.Lett. **88**(2006)092902

7. R.W.Schwartz, M.T.Sebastian, M.V.Raymond, Mater.Res.Soc.Symp.Proc. **623**(2000)365

8. C.M.Chiu, Y.H.Chang, Sens.Actuators B. **54**(1999)236

9. V.V.Kharton, E.N.Naumovich, A.A.Vecher, A.V.Nicolaev, J.Solid.State.Chem. **120**(1995)128

10. S.Madhukar, S.Aggarwal, A.M.Dhote, R.Ramesh, A.Krishnan,D.Keeble, E. Poindexter, J.Appl.Phys.Lett. **81**(1997)3543

11. H Ohbayashi, T.Kudo, T.Gejo, Jpn.J.Appl.Phys. **13**(1974)1

12. R.H.E.van Doorn, A.J.Burggraaf, Solid State Ionics. **128**(2000)65

13. J.M.Liu, C.K.Ong, J.Appl.Phys. **84**(1998)5560

14. J.Mizusaki, J.Tabuchi, T.Matsuura, S.Yamauchi, K.Fueki, J.Electrochem.Soc, **136**(1989)2082

15. J.B.Goodenough, J.Phys.Chem.Solids. **6**(1958)287

16. C-C.Yang, M-S.Chen, T-J.Hong, C-M.Wu, J-M.Wu, T-B.Wu, Appl.Phys.Lett. **66**(1995)2643

17. T.Wu, B.Dong, M.Guo, X.Chen, S.Guo, M.Li, X-Z.Zhao, Thin Solid Films. **497**(2000)329

18. D.J.Lichtenwalner, R.Dat, O.Auciello, A.I.Kingon, Ferroelectrics. **152**(1994)97

19. Y Furusawa, H. DOI, Jpn.J.Appl.Phys. **38**(1999)6864

20. X.Chen, N.Wu, A.Ignatiev, Z.Zhang, W-K.Chu, Thin Solid Films. **350**(1999)130

21. J.Yin,W.Cai,Y.Zheng, L.Zhao, Surf.Coat.Tech. **198**(2005)329

-

CHAPTER 6

Ferroelectric Capacitors

Ferroelectric capacitors were fabricated using LSCO and LSCNO as the electrodes. BST and PZT were used as the ferroelectric material. The structural, electrical and polarization properties of the capacitors were analyzed and were compared with a capacitor fabricated using conventional electrode, ITO. LSCNO emerges as new electrode material for ferroelectric applications.

6.1 Introduction

Ferroelectric thin films have potential applications in nonvolatile ferroelectric random access memory and microelectromechanical systems [1-5]. The wide applications of these materials make them an important topic of research in the recent years. Non volatile ferroelectric random access memory (FeRAM) can be realized using a ferroelectric capacitor. The spontaneous polarization of the ferroelectric material is used in the realization of ferroelectric memory device. The two directions of the spontaneous polarization can be used to represent the two binary logic states "0" and "1" of the memory device [2, 6-7].

Low leakage current, good resistance to breakdown, large polarization, low coercive field, negligible fatigue, minimal imprint are the important prerequisite for the use of ferroelectric capacitors in commercial memory device [6-8]. The reliability of the ferroelectric capacitor depends immensely on the choice of bottom electrode. The electrode material has direct influence on the nucleation, microstructure and electrical properties of the ferroelectric material [2, 9-11]. The electrode must have low resistance, better adhesion to the ferroelectric and layer under the electrode and should provide chemically stable environment for the growth of ferroelectric material and the operation of the device [9,12].

The major degradation factors of the ferroelectric capacitors are fatigue, imprint and logic state retention loss [2, 7, 13]. Fatigue is the loss of switchable polarization when subjected to repeated read/write cycles. The main reason for fatigue is the entrapment of oxygen vacancies, which are the main ionic defects in the ferroelectric-electrode interface. These defects will develop space charge at the interface. This causes the pinning of the domain thereby reducing the switchable polaraization with increasing polarization reversal [14, 15]. Imprint is the preference of a certain polarization state over the other. The asymmetric distribution of the charge defects or the oxygen vacancies is the possible cause for imprint [16, 17]. Logic state retention loss is the failure when the capacitor

and the corresponding memory element are unable to maintain a polarization state and clearly discriminate it from the opposite state for almost indefinitely. The asymmetry in the configuration of top and bottom electrode can cause the retention loss [6, 13].

The most commonly used electrode for ferroelectric memory devices is platinum (Pt) [18, 19]. The major drawback of using Pt electrode is fatigue due to the formation of oxygen depletion layer at the Pt-ferroelectric interface [15, 20]. The switchable polarization of the ferroelectric capacitor using Pt electrode is reported to reduce to 50% of its initial value after 10^6 cycles [21]. Another metallic electrode is Al. PZT crystallizes in a cubic non ferroelectric phase over Al leading to poor ferroelectric properties [22]. The fatigue and imprint can be effectively reduced by the use of oxide electrodes due to their capability to absorb oxygen vacancies and/or their role as effective diffusion barrier [6, 11, 13]. There are two categories for the oxide electrodes: one is the common metal oxide such as RuO_2, and IrO_2; the other group is conductive perovskite oxides, such as $LaNiO_3$, $La_{0.5}Sr_{0.5}CoO_3$ and $SrRuO_3$.

The fatigue of the PZT capacitor is found to be reduced when using RuO_2, and IrO_2 as electrodes [23-26]. But the capacitors fabricated using RuO_2 had high leakage current due to the formation of Pb_2RuO_{7-x} whereas that prepared using IrO_2 suffered from the inter diffusion of Ir with PZT [27, 28]. Conductive oxide electrode ITO has been utilized as the electrode for PZT capacitor. Even though PZT crystallizes readily on ITO, the electrode has high sheet resistivity which further increases when the heterostructure is annealed in oxygen [29, 30]. Cuprate superconductors are also used as electrodes for ferroelectric devices due to its fatigue resistance. But the anisotropic conductivity and thermal and chemical instability of the cuprate superconductors constraints it's processing and usage [31].

Conductive perovskite oxide $La_{0.5}Sr_{0.5}CoO_3$ (LSCO), $LaNiO_3$ (LNO), and $SrRuO_3$ has similar crystal structure as that of ferroelectric and has good chemical stability [12, 32, 33]. Therefore they can serve as electrodes as well as growth template layers and protective barriers during device fabrication [33, 34]. These electrodes being conductive oxides reduce the accumulation of oxygen vacancies at the ferroelectric-electrode interface thereby effectively reducing fatigue and imprint [11, 15]. The perovskite oxide electrode enables the growth of ferroelectric layer along preferred orientation. Thus the leakage current behavior is reduced and the ferroelectric properties are enhanced [34, 35]. Also the better surface morphology of the perovskite electrodes gives good texture characteristics which gives better performance for the device [11, 36].

Ferroelectric capacitors using LSCO electrodes are reported to give superior device performance compared to capacitors using other electrodes. One reason for this phenomenon is the low lattice mismatch between LSCO and Pb-based ferroelectrics which promote the epitaxial growth of the ferroelectric layer over LSCO [33, 37]. LSCO is also the most conductive oxide among the conductive perovskite oxides with a room temperature bulk resistivity of 90-120 $\mu\Omega$cm [38]. The large oxygen non stoichiometry in LSCO gives it high oxide ion diffusivity [39]. Therefore the LSCO electrodes effectively suppresses the polarization fatigue as it act as a sink of oxygen vacancies [14, 20]. This property of LSCO also reduces effectively the imprint behavior of ferroelectric capacitor [20]. LSCO can be grown at the similar growth conditions of the ferroelectric layer, ie at lower substrate temperature compared to other perovskite electrodes [9, 37]. This property is particularly interesting considering the device integration. LSCO can promote perovskite phase formation not only of Pb-based ferroelectrics, but also of other ferroelectric materials such as
$Ba_{1-x}Sr_xTiO_3$ [9, 40].

189

Among the various ferroelectric materials perovskites and layered perovskites are widely investigated for ferroelectric memory applications. The lead based perovskite (PZT) is one of the promising candidates among the perovskite oxide due to its large remanent polarization and low coercive field [2, 7]. The lower crystallization temperature and duration for crystallization makes PZT a more attractive candidate for integration into complementary metal oxide semiconductor (CMOS) technology [8, 33]. The natural fatigue resistant behavior makes $SrBi_2Ta_2O_6$ (SBT) a promising candidate among layered perovskite. But the high crystallization temperature and lower dielectric constant makes the integration of SBT capacitors difficult [41]. A fairly new candidate among the perovskite oxides is $Ba_{1-x}Sr_xTiO_3$. Its large dielectric constant and fatigue free nature makes it another interesting candidate for ferroelectric memory device fabrication [42, 43].

In this chapter we discuss the preparation and characterization of ferroelectric capacitors using $La_{0.5}Sr_{0.5}CoO_3$ (LSCO) and $La_{0.5}Sr_{0.5}Co_{0.5}Ni_{0.5}O_3$ (LSCNO) as electrodes. The devices were fabricated on p-type Si <100> and $Pt/TiO_2/SiO_2/Si$ substrates. $Ba_{0.7}Sr_{0.3}TiO_3$ (BST) and $PbZr_{0.52}Ti_{0.48}O_3$ (PZT) was used as the ferroelectric materials for the fabrication of the device. Structural, electrical and ferroelectric characteristic of the fabricated device were investigated. The properties of the device are compared with the device fabricated using conventional electrode ITO.

6.2 Experimental Details

Ferroelectric capacitors were fabricated with BST and PZT as the ferroelectric material using LSCO and LSCNO as the electrode materials. Figure 6.1 shows the schematic diagram of the ferroelectric capacitor fabricated.
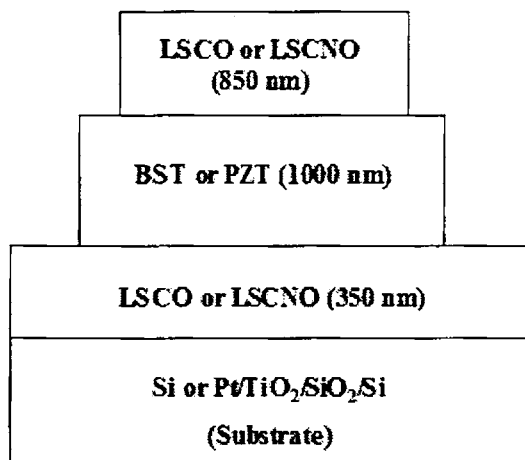
Figure 6.1. Schematic diagram of the ferroelectric capacitor fabricated

The ferroelectric capacitors fabricated using BST had the structure Si/LSCO/BST/LSCO and $Pt/TiO_2/SiO_2/Si/LSCNO/BST/LSCNO$. The top and bottom electrodes of LSCO and LSCNO were fabricated using rf magnetron sputtering. The electrodes were deposited at an rf power of 150 W at a target to substrate distance of 4 cm. The effect of crystallinity of the bottom electrode on the ferroelectric properties of the capacitors was compared by depositing the LSCO bottom electrode both at room temperature and at a substrate temperature of 600 °C. The LSCNO bottom electrodes for the capacitors were fabricated at a substrate temperature of 600 °C. The top electrodes for both the capacitors using LSCO and LSCNO were fabricated at room temperature. BST thin films were deposited by pulsed laser deposition using third harmonics (355 nm) of Q-switched pulsed Nd:YAG laser. Repetition frequency was 10 Hz with a pulse width of 6 -7 ns. Laser fluence was kept at 20 mJ. The deposition was carried out under an oxygen partial pressure of 0.1 mbar and substrate temperature during deposition was kept at 500 °C. An amorphous thin layer of BST (60 A°) was deposited at room temperature prior to the deposition of BST thin film at substrate temperature of 500 °C. This amorphous BST layer forms a buffer layer

for the growth of crystalline BST. The ferroelectric capacitors were also fabricated using PZT and they have the following structure; $Pt/TiO_2/SiO_2/Si/LSCO/PZT/LSCO$ and $Pt/TiO_2/SiO_2/Si/LSCNO/PZT/LSCNO$. The LSCO and LSCNO electrodes were fabricated using rf magnetron sputtering. The bottom electrodes were deposited at substrate temperature of $600^{\circ}C$ and the top electrodes were deposited at room temperature. The PZT layer was deposited by pulsed laser deposition. The deposition was carried out under an oxygen partial pressure of 0.1 mbar and the substrate temperature during deposition was kept at 300 $^{\circ}C$.

The structural characterizations of the heterostructure were carried out using a Rigaku X-ray diffractometer with Cu K_α radiation ($\lambda=1.5418$ A$^{\circ}$). The electrical properties of the device were studied using a Keithly Source Measure Unit (SMU 236). The Polarization-Electric field (P-E) measurements were obtained using RT66A ferroelectric tester.

6.3. Results and Discussion

6.3.1. Structural Properties

The X-Ray Diffraction (XRD) pattern of the Si/LSCO/BST heterostructure is as given in figure 6.2. The BST thin film was found to be polycrystalline in nature with no preferred orientation. Similar XRD pattern was also observed for the BST film grown on LSCNO as the bottom electrode. The perovskite phase of LSCO or LSCNO forms a better growth surface for the growth of perovskite BST [34]. In most processing conditions the ferroelectric layer develop the similar structure of the perovskite electrode layer below it [44].
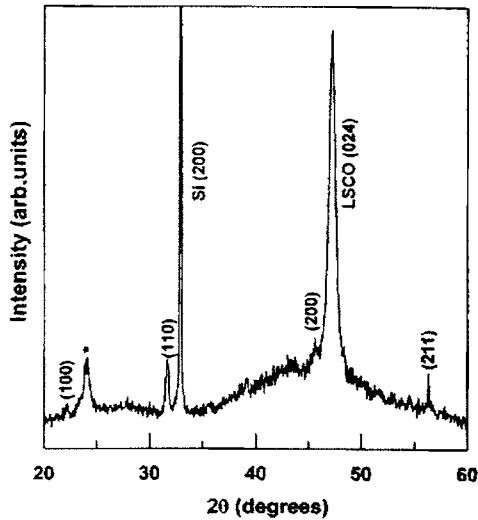
Figure 6.2. The XRD pattern of the Si/LSCO/BST heterostructure.
The indexed patterns correspond to that of BST

LSCO bottom electrode layer is reported to induce the growth of PZT with certain texture because of the small mismatch between LSCO and PZT crystal lattice [45]. But the structural analysis of the $Pt/TiO_2/SiO_2/Si/LSCO/PZT$ and $Pt/TiO_2/SiO_2/Si/LSCNO/PZT$ revealed that only pyrochlore phase of PZT could be grown on LSCO and LSCNO bottom electrodes. The formed pyrochlore phase could not be transformed into perovskite PZT with post deposition annealing. The pyrochlore phase is a non-stoichiometric phase compared to perovskite phase and cannot completely transmit into perovskite phase even when annealed in high crystallization temperatures, if oxygen is insufficient for forming the perovskite phase [46]. The Pb deficiency may also lead to the growth of pyrochlore phase. Further optimization of composition and deposition parameters is necessary to grow perovskite PZT film.

6.3.2 Electrical Properties

The leakage current is an important characteristic of thin film capacitor. It influences the hysteresis loop and directly limits the charge retention. The leakage current is also a sensitive probe of the material quality of the metal-ferroelectric-metal surface, and it strongly dependant on the material aspect of the ferroelectric film and the electrode ferroelectric interfaces [47].
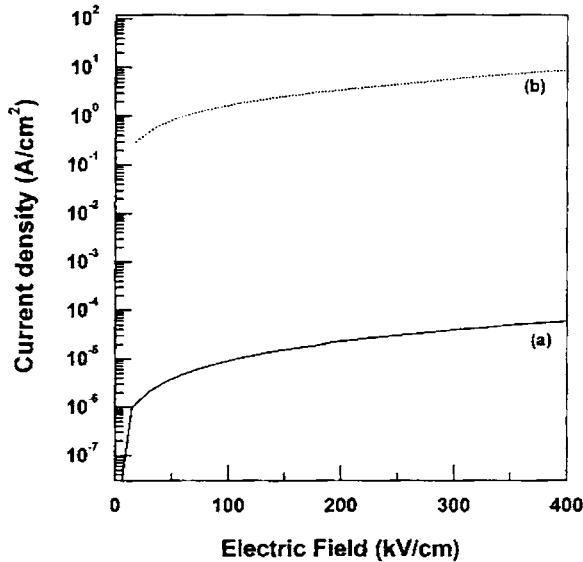

Figure 6.3. Current density (J) vs. electric field characteristics of BST capacitor
(a) with LSCO electrode and (b) with ITO electrode

High leakage conduction in capacitors is a severe problem which can prevent their practical use for FeRAM. Recently there were reports on the reduced leakage current for PZT capacitors using nonconductive oxide electrodes [48]. Capacitor with low leakage current is ideal for microelectronic device application. The current density (J) versus electric field characteristics of the BST capacitor, one with LSCO and another with ITO as electrode are given in

194

figure 6.3. The leakage current of the BST capacitor using LSCO electrode is about four orders of magnitude less than that using ITO electrode. The low leakage current density of the capacitor with LSCO electrode makes it a potential candidate for FeRAM device fabrication.

6.3.3 Polarization Properties

The polarization properties of the ferroelectric capacitor are analyzed using the P-E hysteresis loop. The polarization properties may be broadly classified into two categories: (1) using BST as the ferroelectric and (2) using PZT as the ferroelectric. The hysteresis loop measurements of the capacitors were made for various applied voltages.
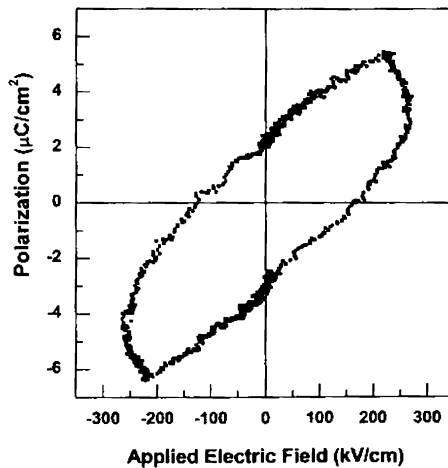
i) BST Capacitor

Figure 6.4. Polarization hysteresis of BST capacitor fabricated using ITO electrodes

BST capacitors were fabricated with both LSCO and LSCNO as the electrodes. The polarization properties of these capacitors were compared with that

195

fabricated using conventional ITO electrode. Figure 6.4 gives the P-E hysteresis loop of a BST capacitor fabricated using ITO as the top and bottom electrodes. The hysterisis loop is like that of a typical lossy dielectric and it does not show any saturation polarization. The lossy behavior of the device is due to the large leakage current associated with the capacitor [27].

The LSCO bottom electrodes were fabricated under two different growth conditions. The influence of the crystallinity of the bottom electrode on the ferroelectric properties of the capacitor was thus compared.
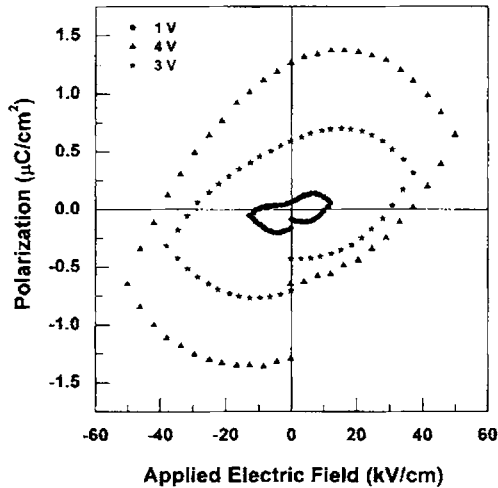

Figure 6.5.P-E hysteresis loop of a BST capacitor with the LSCO as the top and bottom electrode with the bottom electrode deposited at room temperature

Figure 6.5 gives the P-E hysteresis loops of the BST capacitor fabricated using LSCO bottom electrode deposited at room temperature. In this case also the hysteresis loop was like a lossy dielectric with the lossy behavior increasing with the increase in applied voltage. The lossy behavior of the capacitor may be due to large leakage current of the device. The bottom electrode in this case was fabricated at room temperature at a sputtering gas pressure of 0.003 mbar with

196

Ar:O_2 ratio 80:20. The crystallinity of the bottom electrode was poor with a smaller grain size (8 nm). The electrode material directly influences the nucleation, microstructure and electrical properties of the ferroelectric layer [49]. The reduced crystallinity of the bottom electrode is reported to increase the leakage current of the ferroelectric capacitor [27]. During hysteresis loop measurement, the RT66A tester measures the charge collected on an integrating capacitor and converts it to polarization. The charge due to leakage also collects on the integrating capacitor and is therefore included in calculating the polarization. Thus leaky capacitors give false exaggerated polarization values.
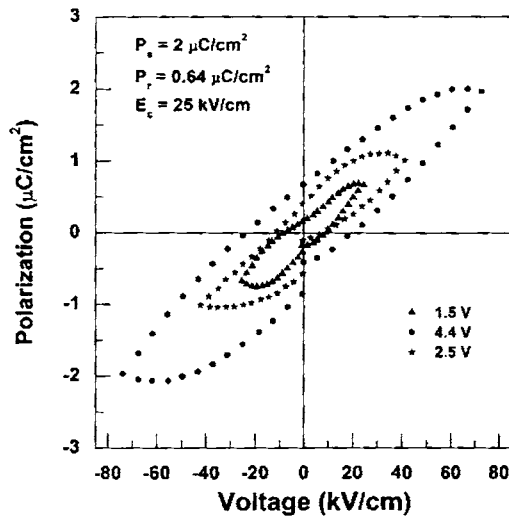

Figure 6.6.P-E hysteresis loop of a BST capacitor with the LSCO as the top and bottom electrode. The bottom electrode deposited at a substrate temperature of 600 °C

The P-E hysteresis loop of the BST capacitor fabricated with the LSCO bottom electrode deposited at a substrate temperature of 600 °C is as shown in figure 6.6. The bottom electrode was fabricated at a sputtering gas pressure of 0.1mbar with Ar:O_2 ratio 50:50. The top electrode of the capacitor was fabricated at room temperature at a sputtering gas pressure of 0.003 mbar with Ar:O_2 ratio 80:20.

The capacitor showed hysteresis behavior with the saturation and remanent polarization of 2 and 0.64 $\mu C/cm^2$ respectively, at room temperature with a coercive field of 25 kV/cm for an applied voltage of 4.4 V. The improved ferroelectric properties of the capacitor is due to the better crystallinity (grain size = 30 nm) and low resistivity ($2x10^{-3}$ Ωcm) of the bottom electrode. The improved crystallinity of the bottom electrode is found to improve the ferroelectric properties [50].

LSCNO was also used as the electrode for the fabrication BST capacitor. The LSCNO bottom electrode was deposited over $Pt/TiO_2/SiO_2/Si$ substrate at a substrate temperature of 300 °C at a sputtering gas pressure of 0.1 mbar with $Ar:O_2$ ratio of 50:50. The top electrode was fabricated at room temperature at a sputtering gas pressure of 0.003 mbar with $Ar:O_2$ ratio of 20:80. Figure 6.7 gives the P-E hysteresis loop of the BST capacitor fabricated using LSCNO as the electrodes.
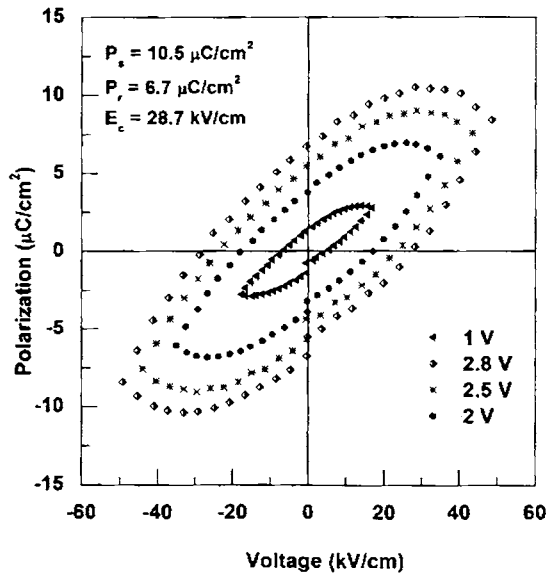

Figure 6.7 P-E hysteresis loop of the BST capacitor fabricated using LSCNO as the electrodes

The figure clearly indicates an improved ferroelectric behavior with large remanant polarization and low coercive field compared to the capacitors prepared using LSCO as the electrodes. The device had a remanent polarization of 6.7 $\mu C/cm^2$ and coercive field of 28.7 kV/cm for an applied voltage of 2.8 V. The better ferroelectric behavior of the device can be attributed to the better crystallinity (30 nm) and conductivity ($\rho = 3.3 \times 10^{-4}$ Ωcm) of the LSCNO electrodes. The improved conductivity of this LSCNO bottom electrode is due to the parallel conduction through the Pt layer beneath the LSCNO layer. The double electrode layer improves the ferroelectric properties with higher remanent polarization and low coercive field. The ferroelectric property of the $Pb_{0.6}Sr_{0.4}TiO_3$ layer deposited on the double electrode layer LSCO/Pt was better than that on single oxide layer such as LSCO [18]. The above result further substantiate that the conductivity and crystallinity of the bottom electrode are crucial in the properties of a ferroelectric capacitor.

The value of the coercive field E_c for the BST capacitor fabricated using both LSCO and LSCNO is larger than the reported values [51]. This is due to the small grain size of the BST thin film. Also the amorphous BST buffer layer act as a capacitive interface layer connected in series with the crystalline BST layer, thereby splitting the voltage that is applied to the multilayer films. This buffer layers reduces the dielectric constant of the device thereby increasing the coercive field [52].

ii) PZT Capacitor

Ferroelectric capacitors were also fabricated using PZT as the ferroelectric using LSCO and LSCNO as the electrodes. The ferroelectric properties of the PZT capacitor fabricated using LSCO as the electrode was compared with that prepared using LSCNO.

199

Figure 6.8 gives the P-E hysteresis loop of the PZT capacitor fabricated using LSCO as the electrodes. The LSCO bottom electrode in this case was fabricated at a substrate temperature of 500 °C on $Pt/TiO_2/SiO_2/Si$ substrates. The sputtering gas pressure was 0.003 mbar with $Ar:O_2$ ratio 20:80. The top LSCO electrode was fabricated at room temperature at a sputtering gas pressure of 0.003 mbar with $Ar:O_2$ ratio 20:80. The device exhibited poor ferroelectric property with very low remanent polarization and high coercive field.
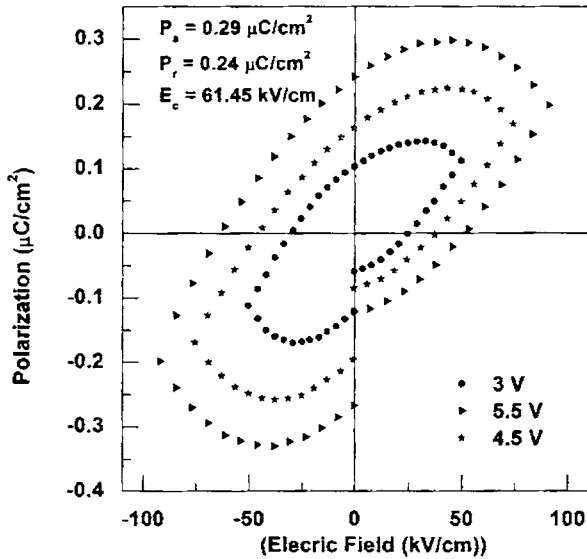

Figure 6.8 The P-E hysterisis loop of the PZT capacitor fabricated using LSCO as the electrodes

Figure 6.9 shows the P-E hysteresis loop of a PZT capacitor fabricated using LSCNO as the electrode. The bottom electrode was fabricated at a substrate temperature of 600 °C and the top electrode was fabricated at room temperature. The LSCNO electrode gave better ferroelectric properties to the PZT capacitor than that using LSCO electrode. The capacitor gave a remanent polarization of 2.9 $\mu C/cm^2$ with a coercive field of 58.4 kV/cm at an applied voltage of 7 V.

The better ferroelectric properties of the PZT using LSCNO electrode may be due to better crystallinity and conductivity of the LSCNO electrode compared to LSCO electrode. An improvement in the crystallinity of the bottom electrode is reported to enhance the remanent polarization of the capacitor [50].
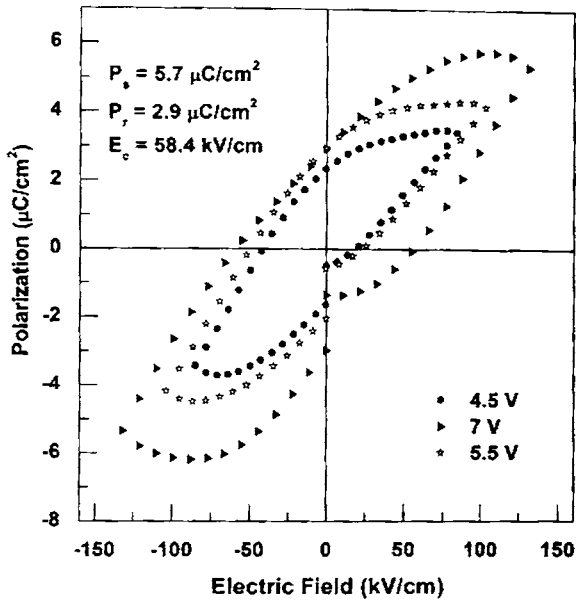

Figure 6.9 The P-E hysteresis loop of a PZT capacitor fabricated using LSCNO as the electrode

The hysteresis loop exhibited a discontinuity in polarization as the capacitor is switched from negative to positive voltage. The gap is more loss of retained charge during the period between setting the polarization state to negative P_r and starting the sweep of positive voltage. The loss of retained charge may be due to domain switching induced either by stress or space charge field [53]. The observed low saturation and remanent polarization of the capacitor is due to the pyrochlore phase of the PZT thin film [46]. Also the polarization is found to be less saturated in the capacitors. This is due to the applied voltage division

between the PZT and LSCNO layer. Therefore the voltage on the PZT layer is too low to make the polarization to saturate [54].

6.4 Conclusion

BST and PZT capacitors were fabricated using LSCO and LSCNO as the electrode materials. The structural, electrical and polarization behavior of the capacitors were studied and compared with ferroelectric capacitors fabricated using conventional ITO electrode. The LSCO electrode provides a low leakage current and better ferroelectric properties compared to conventional ITO electrode. The ferroelectric properties were found to depend on the crystallinity and conductivity of the bottom electrode. The capacitors fabricated using LSCNO as the electrode gave better ferroelectric properties than that using LSCO electrode. LSCNO opens up the possibility of a novel electrode material for ferroelectric devices.

References

1. J. F. Scott , C. A. P. de Araujo, Science. **246**(1989) 1400

2. M.Sayer, Z.Wu, C.V.R.Vasant Kumar, D.T.Amm, E.M.Griswold, Can.J.Phys. **70**(1992)1159

3. R. Ramesh, H. Gilchrist, T. Sands, V. G. Keramidas, Appl.Phys.Lett. **63**(1993)3592

4. N. Setter, D. Damjanovic, L. Eng, G. Fox, S. Gevorgian, S. Hong, A. Kingon, H. Kohlstedt, N. Y. Park, G. B. Stephenson, I. Stolitchnov, A. K. Taganstev, D. V. Taylor, T. Yamada, S. Streiffer, J. Appl.Phys. **100**(2006)051606

5. T. Maeder, P. Muralt, M. Kohli, A. Kholkin, N. Setter, Br. Ceram.Proc. **54**(1995)206

6. H.Ishiwara, FED Jrnl. **11**(2000)27

7. D.Hadnagy, The Industrial Physicist. **5**(1999)26

8. H.N.Al-Shareef, B.A.Tuttle, W.L.Warren, D.Dimos, M.V.Raymond, M.A.Rodriguez, Appl.Phys.Lett. **68**(1996)272

9. J.T.Cheung, P.E.D.Morgan, D.H.Lowndes, X.Y.Zheng, J.Breer, Appl.Phys.Lett. **62**(1993)2045

10. P.W.Chan, W.Wu, K.H.Wong, K.Y.Tong, J.T.Cheung, J.Phys.D.Appl.Phys. **30**(1997)957

11. Y.Furusawa, H.DOI, Jpn.J.Appl.Phys. **38**(1999)6864

12. C.Rossel, A.Rosova, K.Hasekova, D.Machajdik, K.Frohlich, J.Appl.Phys. **100**(2006)04451

13. S.Aggarwal, T.K.Song, A.M.Dhote, A.S.Prakash, R.Ramesh, N.Velaesquez, L.Boyer, J.T.Evans.Jr, J.Appl.Phys. **83**(1998)1617

14. M-S.Chen, T-B.Wu, J-M.Wu, Appl.Phys.Lett. **68**(1996)1430

15. B.Nagaraj, S.Aggarwal, R.Ramesh, J.Appl.Phys. **90**(2001)375

16. G.E.Pike, W.L.Warren, D.Dimos, B.A.Tuttle, R.Ramesh, J.Lee, V.G.Keramidas, J.T.Evans.Jr. Appl.Phys.Lett. **64**(1995)484

17. J.Lee, R.Ramesh, V.G.Keramidas, W.L.Warren, G.E.Pike, J.T.Evans.Jr.

Appl.Phys.Lett. **66**(1995)1337

18. W-J.Lee, Y-M.Kim, H-G.Kim, Thin Solid Films. **269**(1995)75

19. P.D.Hren, S.H.Rou, H.N.Al-Shareef, M.S.Ameen, O.Auciello, A.I.Kingon, Proc.of the 3rd International Symposium on Integrated Ferroelectrics, (1991) pp. 612

20. S.Aggarwal. A.M.Dhote, R.Ramesh, W.L.Warren, G.E.Pike, D.Dimos, M.V.Raymond, B.A.Tuttle, J.T.Evans.Jr, Appl.Phys.Lett. **69**(1996)2540

21. M.C.Jang, T.B.Wu, J.Mater.Res. **9**(1994)1879

22. D.Barrow, C.V.R.Vasant Kumar, R.Pascual, M.Sayer, Mater.Res.Soc.Symp.Proc. **243**(1992)113

23. T.Nakamura, Y.Nakao, A.Kamisawa, H.Takasu, Jpn.J.Appl.Phys. **33**(1994)5207

24. K.B.Lee, S.Tirumala, S.B.Desu, Appl.Phys.Lett. **74**(1999)1484

25. J.Bandaru, T.Sands, L.Tsakalakos, J.Appl.Phys. **84**(1998)1121

26. H.Maiwa, N.Ichinose, K.Okazaki, Jpn.J.Appl.Phys. **33**(1994)5223

27. H-N.Al.Shareef, K.R.Bellur, O.Auciello, A.I.Kingon, Thin Solid Films. **256**(1995)73

28. S.Aggarwal, R.Ramesh, Ann.Rev.Mater.Sci. **28**(1998)463

29. J.C.Manifacier, Thin Solid Films. **90**(1982)297

30. A.V.Rao, S.A.Mansour, A.L.Bement.Jr, Mater.Lett. **29**(1996)255

31. R.Ramesh, W.K.Chan, B.Wilkens, H.Gilchrist, T.Sands, J.M.Tarascon, V.G.keramidas, D.K.Fork, J.Lee, A.Safari, Appl.Phys.Lett. **61**(1992)1537

32. S.Aggarwal, S.R.Persusse, B.Nagaraj, R.Ramesh, Appl.Phys.Lett. **74**(1999)3023

33. S-M.Yoon, E.Tokumitsu, H.Ishiwara. Appl.Surf.Sci. **117/118**(1997)447

34. Y.F.Chen, L.Sun,T.Yu, J-X.Chen, Y-Y.Zhu, N.B.Ming, X-Y.Chen, Z-G.Liu, Thin Solid Films. **269**(1995)18

35. W.Jo, K.H.Kim, T.W.Noh, Appl.Phys.Lett. **66**(1995)3120

36. M.Izuha, K.Abe, M.Koiki, S.Takeno, N.Fukushima, Appl.Phys.Lett. **70**(1997)1405

37. R.Ramesh, H.Gilchrist, T.Sands,, V.G.Keramidas, R.Haakenaasen, D.K.Fork, Appl.Phys.Lett. **63**(1993)3592

38. L.Che, J.Cheng, S.Yu, Z.Meng, Mater.Lett. **61**(2007)3068

39. J.Muzusaki, Y.Mima, S.Yamauchi, K.Fucki, J.Solid.State.Chem. **80**(1989)102

40. H-S.Kim, M-H.Lim, H-G.Kim, I-D.Kim, Electrochemical and Solid State Letters 7(2004)J1

41. Y.I.Kim, D.S.Shin, Appl.Phys.Lett. **71**(1997)2507

42. C-J.Peng, S.B.Krupanidhi, J.Mater.Res. **10**(1995)708

43. F.M.Pontes, E.Longo, E.R.Leite, J.A.Varela, Thin Solid Films. **386**(2001)91

44. C-C.Chou, C-S.Hou, G-C.Chang, H-F.Cheng, Appl.Surf.Sci. **142**(1999)413

45. J.Yin, T.Zhu, Z.G.Liu, T.Yu, Appl.Phys.Lett. **75**(1999)3698

46. J.H.Ma, X.J.Meng, J.L.Sun, T.Lin, F.W.Shi, J.H.Chu, Mater.Res.Bull. **40**(2005)221

47. D.J.Wouters, G.J.Willems, H.E.Maes, Microelec.Eng. **29**(1995)249

48. B.T.Liu, X.Zhang, W.T.Zhang, Z.Yan, C.S.Cheng, F.Li, L.Li, Q.X.Zhao, Mater.Lett. **61**(2007)3045

49. I-D.Kim, H-G.Kim, J.Appl.Phys. **40**(2001)2357

50. J-D.Kim, S.Hana, S.Kawagoe, K.Sasaki, T.Hata, Thin Solid Films. **385**(2001)293

51. W.J.Kim, W.Chang, S.B.Qadri, J.M.Pond, S.W.Kirchoefer, D.B.Chrisey, J.S.Horwitz, Appl.Phys.Lett. **76**(2000)1185

52. E.M.Alkoy, S.Alkoy, K.Uchiyama, and T.Shiosaki, Jpn.J.Appl.Phys. **45**(2006)5110

53. G.S.Wang, X.J.Meng, J.L.Sun, Z.Q.Lai, J.Yu, S.L.Guo, J.G.Cheng, J.Tang, J.H.Chu, Appl.Phys.Lett. **79**(2001)3476

54. Y.P.Wang, L.Zhou, X.R.Lu, Z.G.Liu, Appl.Surf.Sci. **205**(2003)176

CHAPTER 7

Summary and Outlook

7.1 Summary

Ferroelectric memory devices are ideal for future memory technology due to its intrinsic nonvolatility with fast read write access, low power consumption and high density [1]. Perovskite oxide material $La_{0.5}Sr_{0.5}CoO_3$ (LSCO) is an important compound in this regard as it serves as an electrode for ferroelectric memory devices. The similar crystal structure and high electronic conductivity of LSCO ensures better performance for memory devices compared to the conventional metal electrode [2]. The mixed conducting nature (electronic and ionic conductivity) of the compound finds application in electrodes for solid oxide fuel cells (SOFC), gas sensors and oxygen separation membrane [3]. The transport properties of this class of compounds, $La_{1-x}Sr_xCoO_3$, are also important both scientifically and technologically. $La_{0.5}Sr_{0.5}Co_{1-x}Ni_xO_3$ is a relatively new material which has been obtained by the substitution of Co by Ni in LSCO. A systematic investigation of the evolution of the structural and transport properties of LSCO and LSCNO with varying Sr^{2+} and Ni^{3+} concentration respectively has been carried out. The lowering of the crystallization temperature of LSCO and $La_{0.5}Sr_{0.5}Co_{0.5}Ni_{0.5}O_3$ (LSCNO) are particularly important considering the device fabrication. Therefore the various process parameters during the rf magnetron sputter deposition of the thin films were optimized to obtain crystalline and conducting thin films at lower temperature.

$La_{1-x}Sr_xCoO_3$ and $La_{0.5}Sr_{0.5}Co_{1-x}Ni_xO_3$ was prepared for varying Sr^{2+} and Ni^{3+} respectively by solid state reaction. The structural evolution of the systems with varying Sr^{2+} and Ni^{3+} were examined using X-ray diffraction. The transport properties were investigated with varying doping concentration and also by studying the temperature dependent resistivity, magnetoresistance (MR) and thermoelectric power. $La_{1-x}Sr_xCoO_3$ is found to evolve from a paramagnetic semiconducting phase to a ferromagnetic metallic phase with Sr^{2+} doping. The semiconducting composition of $La_{1-x}Sr_xCoO_3$ (x = 0.1) shows a high value of negative MR at low temperature compared to the metallic compositions. An

investigation of the possibility of obtaining MR at room temperature for these compounds is of particular technological interest. This opens up the application of this compound towards magnetic storage of information [4]. The thermoelectric properties of the compound are also worthwhile noting. The semiconducting compositions of both the compounds gave high value of Seeback Coefficient. It will be worthwhile to calculate the thermoelectric figure of merit $Z = \alpha^2 \sigma T/k$, where α is the thermoelectric power, σ the conductivity and k the thermal conductivity of the material with varying doping concentration to investigate the possibility of using these compounds as thermoelectric materials. The different spin states of Co can increase the structural and magnetic disorder of the compound which suppresses the thermal conductivity on one hand and enhances the thermoelectric power on the other [5].

The thin films of LSCO and LSCNO were prepared by rf magnetron sputtering as it ensures stoichiometric deposition of multicomponent compounds. This technique provides films with greater adhesion and homogeneity over large area. The deposition conditions are crucial in determining the properties of LSCO thin films. Therefore the various process parameters such as rf power, sputtering gas pressure, oxygen partial pressure, substrate temperature and post deposition annealing conditions were optimized. The oxygen atmosphere during post deposition annealing was found to be crucial in determining the crystallinity and conductivity of the thin films. In the present investigation the optimized annealing temperature was found to be 600 °C for one hour, a much lower temperature compared to the reported crystallization temperature of LSCO. The crystallization temperature of the compound was further lowered to 500 °C by depositing the films at substrate temperature. The result is particularly important considering the device integration as crystalline and conducting thin films could be grown on Si and $Pt/TiO_2/SiO_2/Si$ substrates at 500 °C.

LSCNO thin films were prepared at the optimized condition of LSCO thin films. LSCNO is particularly important material as it has lower resistivity in thin film

210

form compared to LSCO thin films. Oxygen incorporation during sputtering could yield films with resistivity as low as 10^{-3} Ωcm even at room temperature. This facilitates the room temperature deposition of perovskite top electrode for the ferroelectric capacitor. Crystalline LSCNO thin films could be obtained at a substrate temperature as low as 300 °C. The oxygen incorporation into the thin films resulted in smooth surface morphology which further justifies its application in ferroelectric heterostructures [6].

Ferroelectric capacitors were fabricated using LSCO and LSCNO as the electrode material using both $Ba_{0.7}Sr_{0.3}TiO_3$ (BST) and $PbZr_{0.52}Ti_{0.48}O_3$ (PZT) as the ferroelectric material. The devices were found to yield better ferroelectric properties compared to that using conventional ITO electrode. The results are quite interesting as the device using LSCNO gave better performance than that using LSCO. LSCNO is a novel electrode material. The ferroelectric properties of BST for FeRAM applications are less investigated. Therefore a detailed study investigating the fatigue, imprint and retention properties of BST capacitors using LSCO and LSCNO as the electrode material will be worthwhile.

The electrode material will directly influence the nucleation, microstructure and electrical properties of ferroelectric thin films. The ferroelectric properties of PZT thin films are better on epitaxial LSCO bottom electrode compared to polycrystalline one. The sputtering provides a platform where epitaxial ferroelectric thin films can be grown at lower substrate temperatures and the technique is also industrially compatible, therefore the epitaxial growth of both LSCO and LSCNO thin films for better ferroelectric capacitors can be investigated [7]. These heterostructure can be further investigated for the development of nondestructive memory readout, ferroelectric FET (FeFET) [8].

LSCO and LSCNO thin films can also serve as buffer layers for the deposition of ferroelectric epitaxial superlattices which improves the properties of the material through surface modification [9]. Therefore ferroelectric superlattice

211

structures can be fabricated to explore the fundamental physical phenomena also to fabricate new functional devices [10]. The spin states of the $La_{1-x}Sr_xCoO_3$ thin films can be investigated by the fabrication of $La_{1-x}Sr_xCoO_3$/Nb-doped $SrTiO_3$ heterojunctions. These junctions exhibit good rectifying properties and its properties are tuned by the competition and evolution of Jahn-Teller splitting and spin splitting [11].

References

1. R.Bruchhaus, B.K.Moon, A.Hilliger, N.Nagel, Y.Yamada, H.Itokawa, K.Yamakawa, I.Kunishima, G.Beitel, Inter.Ferroelectrics. **64**(2004)115

2. S.M.Yoon, E.Tokumitsa, H.Ishiwara, Appl.Surf.Sci. **117/118**(1997)447

3. H.U.Anderson, Solid State Ionics **52**(1992)33

4. E.Dagotto, T.Hotta, A.Moreo, Physics Reports. **344**(2001)1

5. K. Berggold, M. Kriener, C. Zobel, A. Reichl, M. Reuther, R. Müller, A. Freimuth, and T. Lorenz, Phys.Rev.B. **72**(2005)155116

6. J.T.Cheung, P.E.D.Morgan, D.H.Lowndes, S-Y Zheng, J.Breen, Appl.Phys.Lett. **62**(1993)2045

7. I. Kanno, S. Hayashi, R. Takayama, and T. Hirao, Appl.Phys.Lett. **68**(1996)328

8. S. Mathews, R. Ramesh, T. Venkatesan, J. Benedetto, Science. **276**(1997)238

9. H-N.Tsai, Y-C.Liang, H-Y.Lee, Journal of Crystal Growth **284**(2005) 65.

10. H-Y.Lee, K-F.Wu, H-J.Liu, C-H.Lee, Y-C.Liang, Thin Solid Films **515**(2006) 1102

11. G. Li,T.F.Zhou, D.D.Hu, Y.P.Yao, Y.Hou, X.G.Li, Appl.Phys.Lett. **91**(2007)163114

-